NORTHWESTERN UNIVERSITY

Charge Dynamics in New Architectures for Dye-Sensitized Solar Cells

A DISSERTATION

SUBMITTED TO THE GRADUATE SCHOOL

IN PARTIAL FULFILLMENT OF THE REQUIREMENTS

for the degree

DOCTOR OF PHILOSOPHY

Field of Chemistry

By

Alex Brandon Fletcher Martinson

Evanston, IL

December 2008

© Copyright by Alex B. F. Martinson 2008

All rights reserved

ABSTRACT

Charge Dynamics in New Architectures for Dye-Sensitized Solar Cells

Alex Brandon Fletcher Martinson

The promise of a clean, renewable, and abundant energy supply make the efficient conversion of solar energy to electricity a compelling scientific and societal goal. In the following chapters, I will describe my efforts to advance one class of photovoltaic technology, dye-sensitized solar cells, by demonstration and characterization of unexplored device architectures.

Chapter 1 provides an introduction to the origin of solar energy conversion and the fundamentals of dye-sensitized solar cells. An understanding of device operation through charge dynamics facilitates a survey of the state of the art in addition to predictions for promising future directions.

Chapter 2 elucidates the electron transport and interception dynamics in ZnO nanorod array based dye-sensitized solar cells. The data presented suggest that the study of alternative photoanode architectures is a viable means of improving device performance and understanding.

Chapter 3 introduces a new photoanode design in which anodic aluminum oxide and atomic layer deposition are utilized to fabricate oriented arrays of electrically interconnected semiconductor nanotubes. The viability of these structures as dye-sensitized electrodes is

demonstrated by characterization of their morphology, light harvesting efficiency, and photovoltaic performance.

Chapter 4 builds upon the successful implementation of nanotube based dye-sensitized solar cells by quantifying charge dynamics through electrochemical impedance spectroscopy. Fitting the impedance data to an appropriate equivalent circuit establishes ZnO nanotubes as the most effective architecture for rapid electron collection to date.

Chapter 5 expands the synthetic palette of atomic layer deposition to include transparent conducting oxides that may be grown on high aspect ratio templates. Understanding and optimizing the growth mechanism of two versatile systems enables the structures to be presented in the final chapter.

Chapter 6 concludes with a presentation of a unique dye-sensitized solar cell architecture in which electrons are collected radially through adjacent, concentric transparent conducting oxide nanotubes. The exceedingly fast electron collection exhibited suggests the design strategy has potential to revitalize the field by overcoming its most prominent obstacle, iodide-based electrolytes.

ACKNOWLEDGMENTS

Let me start at the beginning and thank my high school chemistry teacher Jeffery Chalmers for teaching me that chemistry is amusing. If watching a football coach leap from a lab bench to invert an umbrella is not enough to motivate a career in science then I'm not sure what is. I need also thank my undergraduate chemistry, math, and physics professors and mentors at Luther College. They are scholars in the truest sense and serve as models for living a rigorous yet balanced life. In particular, I'd like to thank Dale Nimrod and Claude Mertzenich for pushing me higher and harder toward opportunities that I knew not existed.

I thank members of the Hupp group, past and present, for providing an invigorating atmosphere in which to do good science. Here I especially thank my classmates Karen, Mohammed, and Tendai for rising, falling, and floating along with me through the torrents of graduate school. I am indebted to Aaron Massari for the guidance and confidence to launch my graduate career. I thank Tom Hamann for teaching me to challenge everything and reminding me that we are the future of science. I thank Joe Hupp for giving me the opportunity to find my own path and the guile to see me through it. Working with Joe is intellectually challenging, humbling, and always a pleasure. I thank also my collaborators at Argonne National Laboratory, Mike Pellin and Jeff Elam, for taking a risk on me and then investing wholly. As a spring of new ideas and a rock of experimental proficiency, Mike and Jeff have added immeasurably to my graduate school experience. In addition, Jeff and I share authorship on the majority of my recent publications. As such I am grateful to him for many of the words found within.

I thank my parents and sister, without whose unwavering support and unabashed cheering I would not be here today. My mother and father, Rosanna and Lynn, have spent the better part of two decades paving the way for my education and for that I am deeply indebted.

Finally, and most importantly, I thank my brilliant wife Katie and our two stunning girls, Abigail and Isabel. Their smiles are what I live for and they bring meaning to everything I do. This dissertation is a direct result of Katie putting her career goals on hold and it is as much hers as it is mine. I love you, Katie, and dedicate these pages to you.

TABLE OF CONTENTS

LIST OF TABLES

Chapter 1

Chapter 5

LIST OF FIGURES

Chapter 1

Chapter 2

Chapter 3

Chapter 4

Chapter 5

Chapter 6

Chapter 1. Introduction to Dye-Sensitized Solar Cells

1.1. Energy

1.1.1. World Energy Consumption

The productivity and standard of living of a society is proportional to the energy consumed per capita. Energy powers offices by day, lights the pages of textbooks by night, and moves food, medicine, and information continuously. Current estimates of global energy consumption exceed 4.1×10^{20} J annually, which is equal to an instantaneous yearly-averaged rate of 13 TW. By 2050, the rate of consumption is projected to reach 30 TW.[1] While energy efficiency should be fully utilized to slow this pace, given an increasing world population and improving standard of living, some increase is inevitable and a sign of progress. In the near future, greater availability of affordable energy, if generated responsibly, will benefit the human condition. But in this brief moment in human history in which fossil fuels are easily extracted and politically acceptable to burn, energy use has become a necessary evil.

1.1.2. Energy Sources

The current source of energy for the world's population is overwhelming (85%) derived from fossil fuels. The remainder is a mix of nuclear (6%), biomass (4%), and hydro (3%) with the balance (2%) derived from other renewable resources such as geothermal heat, wind, and solar.[2] This energy mix is problematic for the present and near future for several reasons. First, fossil fuels reserves are being consumed several orders of magnitude faster than they can be replenished. Veins of coal, the largest fossil resource that formed over the last hundred million years will be exhausted in a single millennia. The remaining one trillion tons of proven coal reserves are expected to be consumed in 164 years. Conservative estimates of petroleum use project peak production during this century.[3] Fossil resources will simply not be an option for

future generations. Burning fossil fuels is also problematic for its negative impact on the environment. Even if the world's carbonaceous fuels were unlimited, the impact of the ensuing pollution and climate change are unsustainable. While the emission of sulfur and mercury have been recognized and regulated in the US since the Clean Air Act of 1970, there is currently no regulation of carbon dioxide emissions. This is despite assertions from the Intergovernmental Panel on Climate Change (IPCC) that "most of the observed increase in globally-averaged temperatures since the mid-20th century is very likely due to the observed increase in anthropogenic GHG concentrations."[4]

Abandoning fossil fuels, by choice or by exhaustion of supply, leaves a small handful of options including fission, fusion, and what is broadly classified as renewable energy. Fission reactors have proven effective but face geopolitical complications owing to a poor safety record and the fear of weapon proliferation. As a result, a nuclear power plant has not been built in the US since 1996. Nuclear fusion, in contrast, is a developing technology that has yet to show controlled net energy production. The ITER international tokamak project, which many hope will be the predecessor to the first useful fusion power plant, is currently slated to begin testing in 2016.[5] The popularity and propagation of renewable energy technology, in contrast, has soared in recent years. The small environmental impact and lack of geopolitical concerns have created a boom in the industry that is often compared to that of the semiconductor industry in the 1990s.[1] Since renewable resources vary by geographic location, diverse approaches have become economically viable in different regions. For example, greater than 99% of Iceland's electricity is generated by hydropower and geothermal energy due to the concentrated renewable resources (and lack of fossil fuels) available to the country.[6] But to significantly supplant (and expand) the world's current mix, the renewable resource must be vast and wide-spread. In

contrast to other renewable resources whose globally extractable power is each less than 5 TW, the solar constant on the earth's surface is 120,000 TW.[1] This massive flux of photons incident on the earth from the sun comprises an inexhaustible and plentiful energy source for the foreseeable future. The abundant supply and environmental friendliness of solar energy make the efficient conversion of solar radiation into electricity a compelling scientific and economic goal.

1.2. Photovoltaics

1.2.1. History

Civilizations have been deliberately and directly harnessing the sun's power to improve the human condition for at least 2700 years. Evidence suggests that the first application was the concentration of sunlight to light fires and torches for religious ceremony.[7] The Greek scientist, Archimedes, also claims to have utilized bronze shields to reflect and focus sunlight in order to ignite enemy ships from a distance of 50 meters, a feat that was successfully recreated by the Greek navy in 1973. Throughout the first millennia of the common era (C.E.) south-facing windows provided passive solar heating to residences and bathhouses.[7]

The direct conversion of sunlight into electricity, however, is less than 150 years old. The French scientist Edmond Becquerel is credited with first recognizing the photovoltaic effect in 1839. But it wasn't for another 44 years that the first solar cell was created by Charles Fritts, an American inventor who coated selenium wafers with gold to produce a 1% efficient device.[7] Modern photovoltaic technology would have to wait another 71 years, until 1954 - coincidentally the same year that the world's first nuclear power plant came online, for researches at Bell Labs to stumble upon silicon's light sensitivity. The result was a 6% efficient device that would

steadily evolve over the next 50 years to become the prevailing commercial photovoltaic installed today.[7]

1.2.2. State of the Art

In parallel with silicon solar cell technology, a wide variety of alternative photovoltaics have been developed and commercialized. A graphical representation of the primary technologies, Figure 1.1, illustrates improvements in power efficiency over the last several decades. Multijunction, GaAs and crystalline Si cells are the only photovoltaics that have reached greater than 20% efficiency to date. These cells rely upon highly pure and crystalline semiconductors to swiftly extract charges, making this the most efficient and expensive category. Thin film technologies, including $Cu(In,Ga)Se_2$ and CdTe, range from 12 to 20% efficiency. This type of PV relies upon higher extinction materials to achieve adequate light collection in a thinner active layer, thereby relaxing the demands on materials purity and therefore cost. As the first commercialized devices are just starting to be installed, the cost of these systems is yet to be determined. The final classification, labeled only "Emerging PV" in the figure, broadly describes those PV which include organic or molecular species. The operation of these devices, also called excitonic solar cells, profoundly differs from purely inorganic PV. Due to the low dielectric environment of organic semiconductors and molecules in excitonic solar cells, photoexcitation results in a bound electron-hole pair (exciton).[8] These mobile excited state species may efficiently dissociate across an interface of two materials with different electron affinities (a heterojunction). It is the most efficient of this class of PV, namely dye-sensitized solar cells (DSSCs), that is the topic of this work.

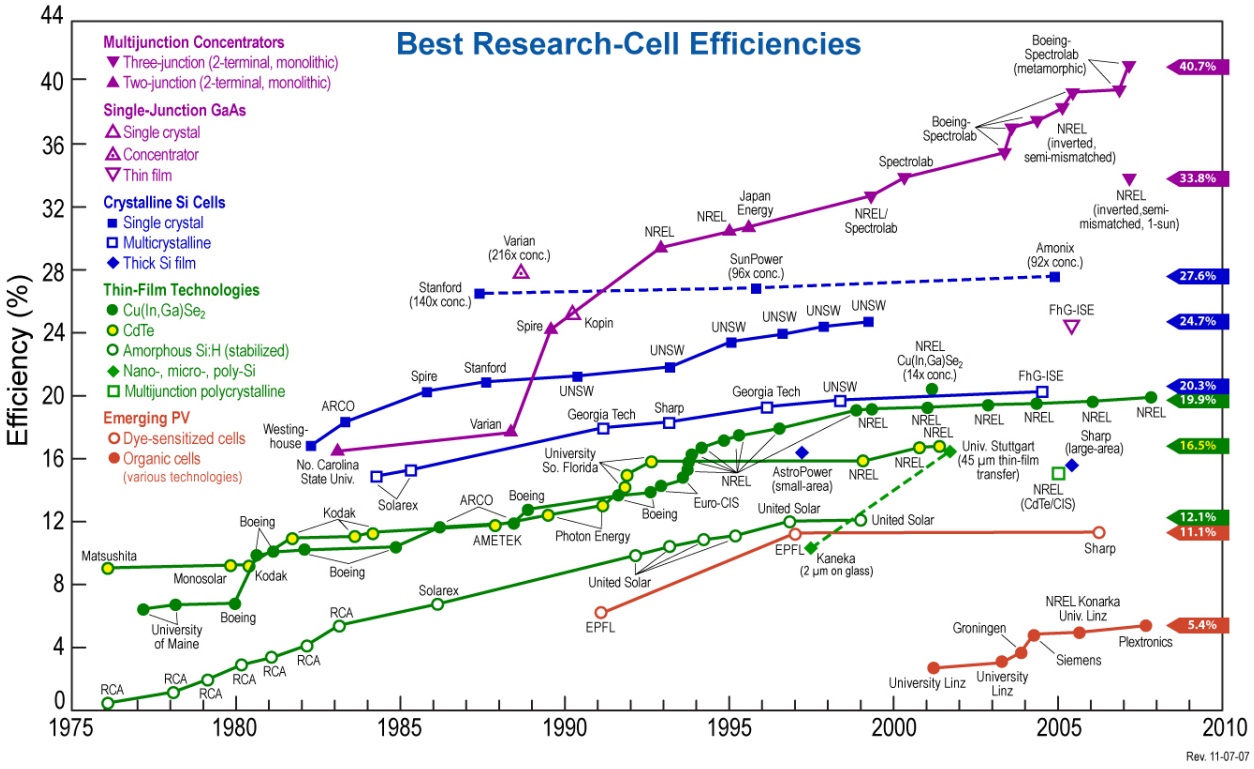

Figure 1.1. Power efficiency of major photovoltaic technologies since 1975.[1]

1.3. Dye-Sensitized Solar Cells

1.3.1. Introduction

While the efficiency of numerous classes of photovoltaic technology has been steadily climbing, one class – dye-sensitized solar cells (DSSCs) – has notably plateaued. After the original report of a 7% efficient DSSC in 1991, Grätzel and co-workers quickly pushed the efficiency to 10% by 1993.[9, 10] Despite the relatively incremental improvements in efficiency since then, reaching the current record of 11.2%, a sea of relevant literature has emerged to raise our basic science understanding at this intriguing confluence of electrochemisty, photophysics, and materials chemistry.[11-14]

Like organic photovoltaics, DSSCs rely upon an interface to efficiently split excitons, the tightly bound electron-hole pairs generated by the absorption of light. In the most common and most efficient devices to date, light is absorbed by a ruthenium complex, such as $(Bu_4N)_2$[Ru(4,4'-dicarboxy-2,2'-bipyridine)$_2$(NCS)$_2$],[15] that is bound to a metal oxide photoanode via carboxylate moieties. The photoanode, usually TiO_2, is composed of 10 – 20 nm diameter nanocrystals that have been spread on a transparent, conducting oxide (TCO) substrate and sintered to form a ~16 μm thick film. Following light absorption, the exciton is split across the dye/nanoparticle interface in femtoseconds to picoseconds. The injected electron diffuses through the sintered particle network to be collected at the TCO, while the oxidized dye is reduced by a redox shuttle, I^-/I_3^-, dissolved in a solution that both permeates the porous photoelectrode and contacts the circuit-completing dark electrode (typically, platinized TCO). Diffusion of the oxidized form of the shuttle to the counter electrode (dark electrode) completes the circuit, Figure 1.2. The slow, random walk of electrons through the nanoparticle film limits the collection of charges to the millisecond timescale. Considering the close proximity at which

opposing charges traverse the microns-thick device, the successful operation of DSSCs is a small wonder.

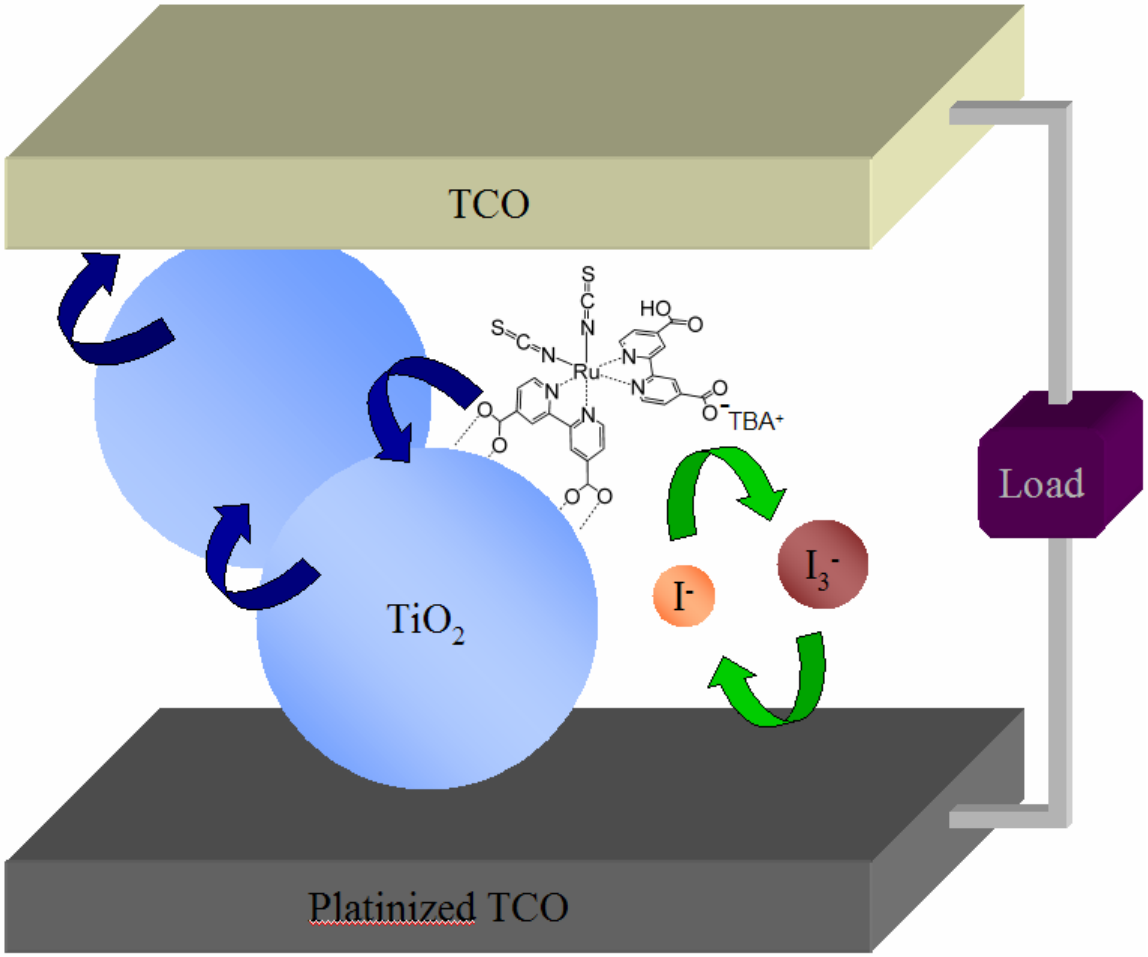

Figure 1.2. Schematic of dye-sensitized solar cell operation (not to scale). Arrows depict the desired flow of electrons through the device.

1.3.2. Charge Dynamics

In order to understand and advance DSSC technology, the kinetics and dynamics of charge movement have been examined in detail by many researchers, both experimentally and via computational modeling. The transfer of electrons and holes across several, often non-ideal and ill defined, heterogeneous interfaces is exceptionally complex. As such, the kinetics are sensitive to many subtle factors such as excitation wavelength and dye loading conditions.[16, 17] Since the kinetics are complicated and don't always conform to a simple rate law, rate constants aren't strictly meaningful. Herein I will follow the convention of reporting half-life times, Table 1.1, in order to appreciate the different time scales of the relevant processes that span nine orders of magnitude.

Process	*Half-life (s)*	*Reference*
Injection	150 ps	S. A. Haque, E. Palomares, B. M. Cho, A. N. M. Green, N. Hirata, D. R. Klug and J. R. Durrant, *Journal of the American Chemical Society* **2005**, *127*, 3456-3462.
Relaxation	12 ns	J. E. Kroeze, N. Hirata, S. Koops, M. K. Nazeeruddin, L. Schmidt-Mende, M. Gratzel and J. R. Durrant, *Journal of the American Chemical Society* **2006**, *128*, 16376-16383.
Regeneration	1 us	J. N. Clifford, E. Palomares, M. K. Nazeeruddin, M. Gratzel and J. R. Durrant, *Journal of Physical Chemistry C* **2007**, *111*, 6561-6567.
Recombination	3 us	E. Palomares, J. N. Clifford, S. A. Haque, T. Lutz and J. R. Durrant, *Journal of the American Chemical Society* **2003**, *125*, 475-482.
Charge Transport	100 us	B. C. O'Regan, K. Bakker, J. Kroeze, H. Smit, P. Sommeling and J. R. Durrant, *Journal of Physical Chemistry B* **2006**, *110*, 17155-17160.
Charge Interception	1 ms	B. C. O'Regan, K. Bakker, J. Kroeze, H. Smit, P. Sommeling and J. R. Durrant, *Journal of Physical Chemistry B* **2006**, *110*, 17155-17160.

Table 1.1. Kinetic processes in DSSCs near the power point.

For each time constant, the value shown in Figure 1.3 is the most current literature datum measured on a standard cell under operating conditions, preferably at the maximum power point (≈700 mV).[18-22] A standard cell is taken to be a complete device with configuration similar to the most efficient DSSC to date.[23] Processes refer to electron dynamics unless otherwise noted and rates in direct kinetic competition are shown with the same color. In order to relate these processes to PV performance, the charge dynamics are best viewed on a modified energy level diagram, Figure 1.4. Potentials are taken from literature reports, Table 1.2.

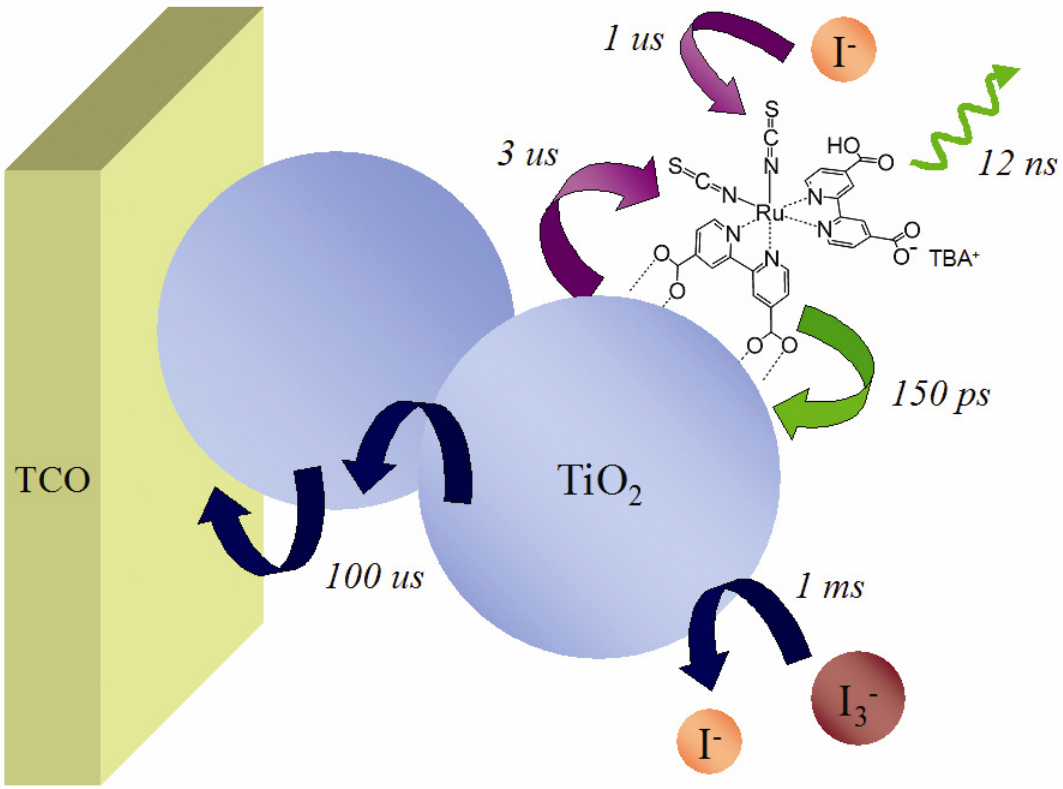

Figure 1.3. Kinetic processes in DSSCs. Processes in kinetic competition have similar colors.

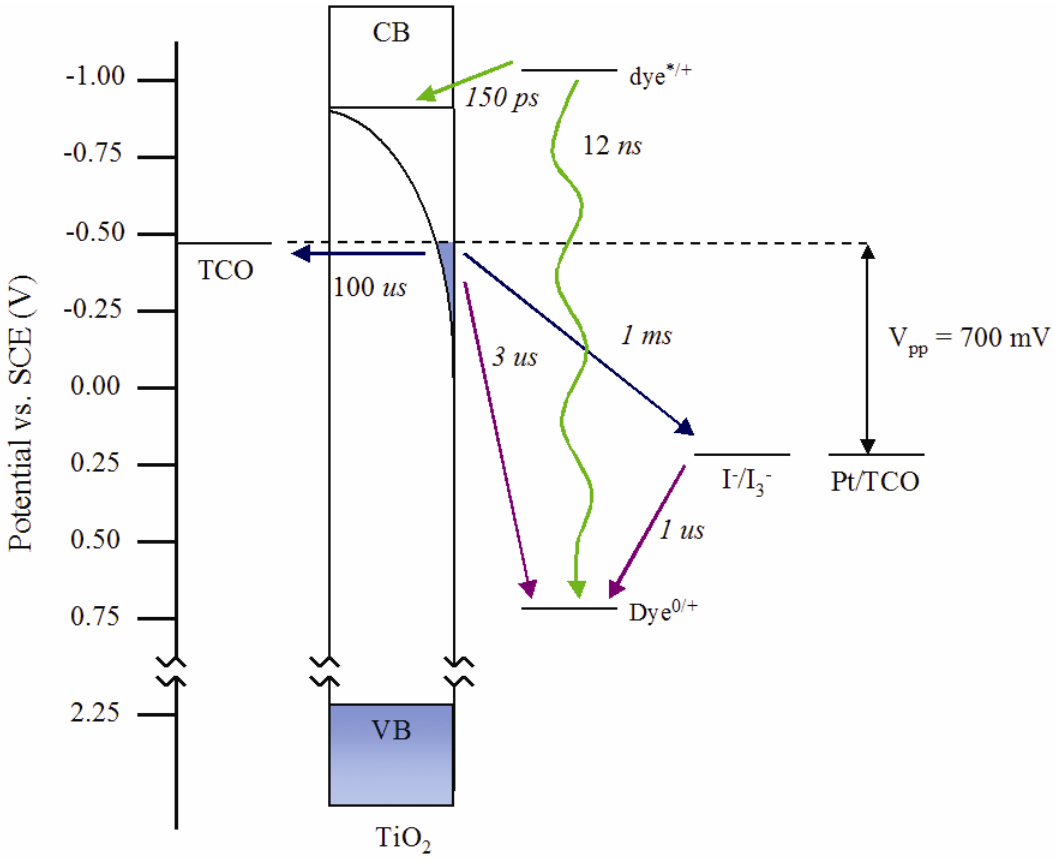

Figure 1.4. Kinetic processes in DSSCs on a modified energy level diagram.

	Potential vs. SCE	*Reference*
TiO_2 E_{CB}/q	-0.9 V	G. Redmond and D. Fitzmaurice, *Journal of Physical Chemistry* **1993**, *97*, 1426-1430. G. Rothenberger, D. Fitzmaurice and M. Gratzel, *Journal of Physical Chemistry* **1992**, *96*, 5983-5986
TiO_2 E_{VB}/q	2.2 V	$E_{VB} = E_{CB} + E_{bandgap}$ = -0.9 eV + 3.1 eV
$N719^{*/+}$	- 1.04 V	$E°^{*} = E° - E^{00}/q$ = 0.71 - 1.75 gap
$N719^{0/+}$	0.71 V ($N3^{0/+}$ = 0.87 V)	M. K. Nazeeruddin, S. M. Zakeeruddin, R. Humphry-Baker, M. Jirousek, P. Liska, N. Vlachopoulos, V. Shklover, C. H. Fischer and M. Gratzel, *Inorganic Chemistry* **1999**, *38*, 6298-6305.
I^-/I_3^-	0.23 V	Nernst corrected CRC value

Table 1.2. Potentials relevant to DSSC operation.

The convenience of reporting half times of reaction rates may result in the misconception that there is considerable room for improvement by minimizing kinetic redundancy. For example, it appears that charge injection is almost 100 times faster than the competing process, relaxation of the excited state. If this were the case, then V_{OC} could be substantially enhanced by shifting the conduction band edge of TiO_2 negative without loss of charge collection efficiency. That this is *not* the case (or at least not entirely) is due to the dispersive kinetics of charge injection. In fact, studies of competing processes have shown that in its most efficient configuration a DSSC has comparatively little kinetic redundancy.[18, 24] This point may be visualized in Figure 1.5, in which order-of-magnitude estimates of area normalized rates at the maximum power point are taken from literature and presented as gaussian curves on a logarithmic time scale.[18-22]

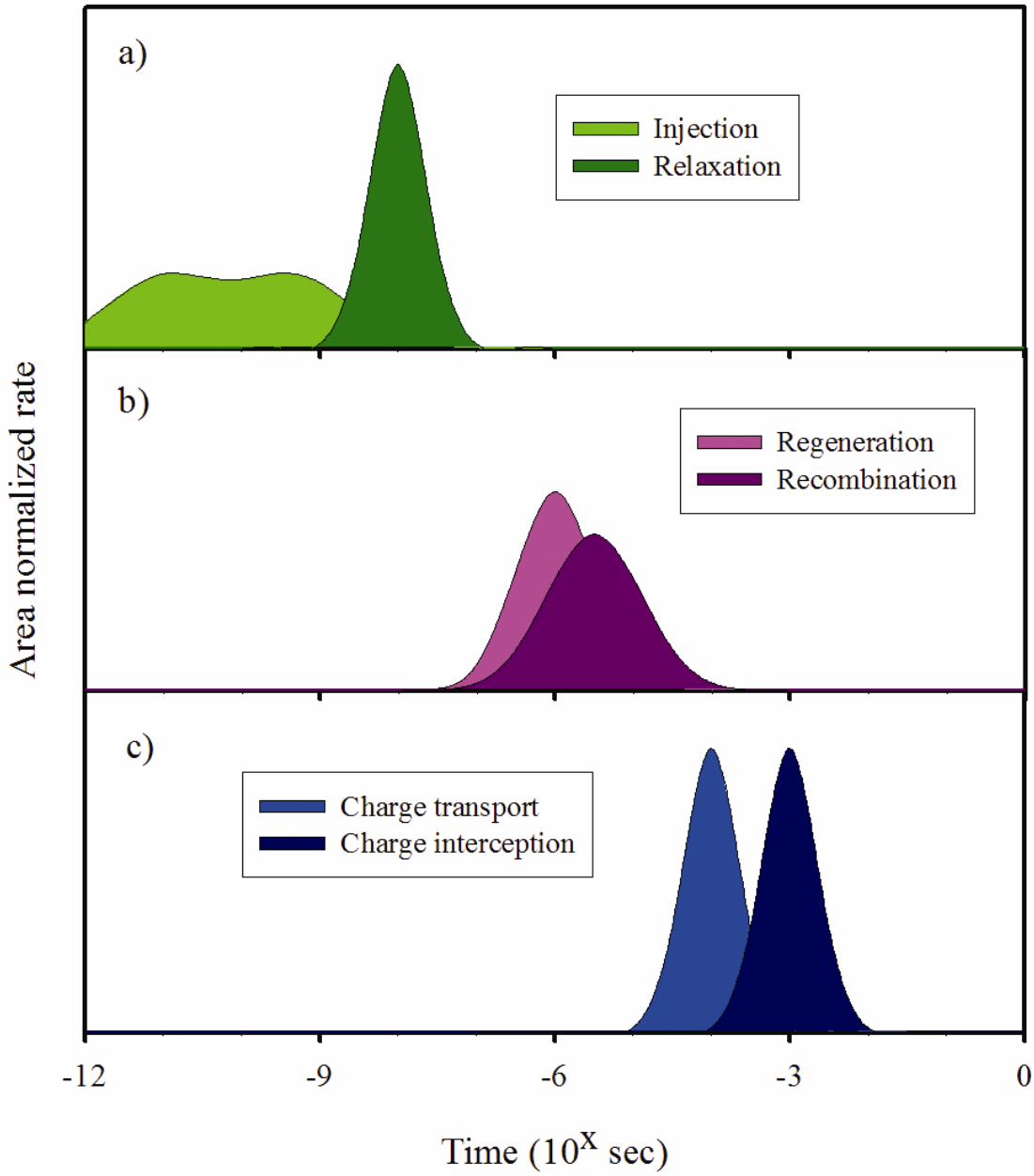

Figure 1.5. Area normalized rates from literature show charge dynamics in direct kinetic competition at the maximum power point.

As state-of-the-art DSSCs have been optimized for maximum voltage while retaining near unity absorbed photon-to-current efficiency, dramatically new versions of the key components are warranted to advance the field. These could include new super chromophores that can collect light 10 to 100 times more efficiently than existing chromophores, new shuttles that can regenerate dyes at low driving force yet exhibit slow interception of injected charges, or new photoelectrode architectures.

1.3.3. Photoanode Requirements

By combining optical transparency with superior dye loading, the introduction of a sintered titania nanoparticle (NP) film was paramount to the early success of DSSCs.[9] The NP film exhibits remarkably slow electron diffusion matched only by the exceedingly slow charge interception by adjacent I_3^-. Even sixteen years after its inception, a complete understanding of the competition between transport of the electron through the TiO_2 NP membrane versus interception by I_3^- – which is the key to the efficient operation of existing DSSCs – remains elusive.[13, 20] While the NP film is still present in the most efficient DSSCs to date, new materials and nanoscale architectures are attracting attention.

The demands on a DSSC photoanode are many-fold. These demands are best illustrated by examining a mathematical model that describes a photoanode's primary task, quantitative charge transport of injected electrons to the TCO. The continuity equation, introduced for DSSCs by Lindquist and popularized by Peter, describes electron generation, diffusion, and interception, respectively.[13, 25]

$$\frac{\partial n}{\partial t} = \eta_{inj} I_0 \alpha e^{-\alpha x} + D_n \frac{\partial^2 n}{\partial x^2} - \frac{n(x)}{\tau_n} = 0 \quad (1)$$

with boundary conditions:

$$n(0) = n^0 e^{\frac{qU}{k_B T}} \quad (2)$$

$$\frac{dn(d)}{dx} = 0 \quad (3)$$

Here the electron concentration, charge injection efficiency, incident photon flux, absorption coefficient, and apparent diffusion coefficient, are represented by n, η_{inj}, I_0, α, and D_n, respectively. The effective (trap-limited) lifetime of electrons, τ_n, describes the rate of interception of electrons in the photoanode by I_3^- through the film thickness, d. The variables n^0, q, U, k_B, and T represent equilibrium (dark) electron density, the elementary charge, voltage, Boltzman's constant, and temperature. This steady-state equation may be solved numerically throughout the thickness, x, of the film or solved exactly at the TCO in order to generate current-voltage plots.[25]

$$j(U) = q\eta_{inj} I_0 L\alpha \frac{-L\alpha \cosh\left(\frac{d}{L}\right) + \sinh\left(\frac{d}{L}\right) + L\alpha e^{-d\alpha}}{(1 - L^2\alpha^2)\cosh\left(\frac{d}{L}\right)} - qD_n n^0 \frac{\sinh\left(\frac{d}{L}\right)}{L\cosh\left(\frac{d}{L}\right)}\left(e^{\frac{qU}{kT}} - 1\right) \quad (4)$$

where the electron diffusion distance, L, is related to D_n and τ_n by

$$L = \frac{1}{\sqrt{D_n \tau_n}} \quad (5)$$

The kinetic competition between charge injection and excited state decay (Figure 3a) is parameterized by η_{inj}. The competition between dye regeneration and recombination to the dye$^+$ (Figure 1.5b) is notably absent, although it has been incorporated in more detailed models.[26] The primary duty of this model is to predict the distribution of electrons throughout the photoanode and the current-voltage characteristics for a given competition between τ_n and charge transport (τ_d), which is inversely proportional to D_n, Figure 1.5c.

A good photoanode will maximize the number of electrons generated, the rate at which they are collected, and their lifetime by maximizing each independent variable listed above. Briefly, η_{inj} is maximized by having a large density of unpopulated states in the photoanode positive of the dye$^{*/0}$ potential, preferably at optimal exoergicity. Maximizing the photon flux to the dye is dependent upon the transparency of the unsensitized semiconductor framework. The absorption coefficient is directly proportional to the effective molar concentration of the dye, which is determined by the roughness of the framework. D_n goes as the mobility of the semiconductor according to the Einstein relation, but is often determined by trap controlled hopping between low energy states.[27, 28] Finally, τ_n, is related to the quasi-Fermi level of electrons in the film, and also shows trap density dependence.[29, 30] All else being equal, a photoanode that increases one of these independent variables will increase efficiency, with the exception of D_n, which offers diminishing returns in the limit of kinetic redundancy (Figure 1.5c).

1.3.4. Nanoparticle Photoanodes

As a transparent, high surface area framework, a metal oxide NP film was an excellent starting point for DSSCs. The ease of fabrication, minimal cost, and control over light scattering has ensured these structures provide the basis for the most efficient DSSCs to date (11.2 %). Optimized films employ 10 – 20 nm spherical particles to form a high surface area, 12 μm thick transparent film, Figure 1.6. The surface area enhancement is described by the roughness factor, defined as the ratio of actual surface area to the projected surface area, with NP films exhibiting roughness factors in excess of 1000. A ≈4 μm thick film of much larger (≈400 nm) particle diameter is subsequently deposited in order to scatter red and near-IR photons back into the transparent film.[23] (The dyes employed in the most efficient cells typically absorb poorly in the red and near-IR region, so they can collect more photons in this region if a scattering layer is present.)

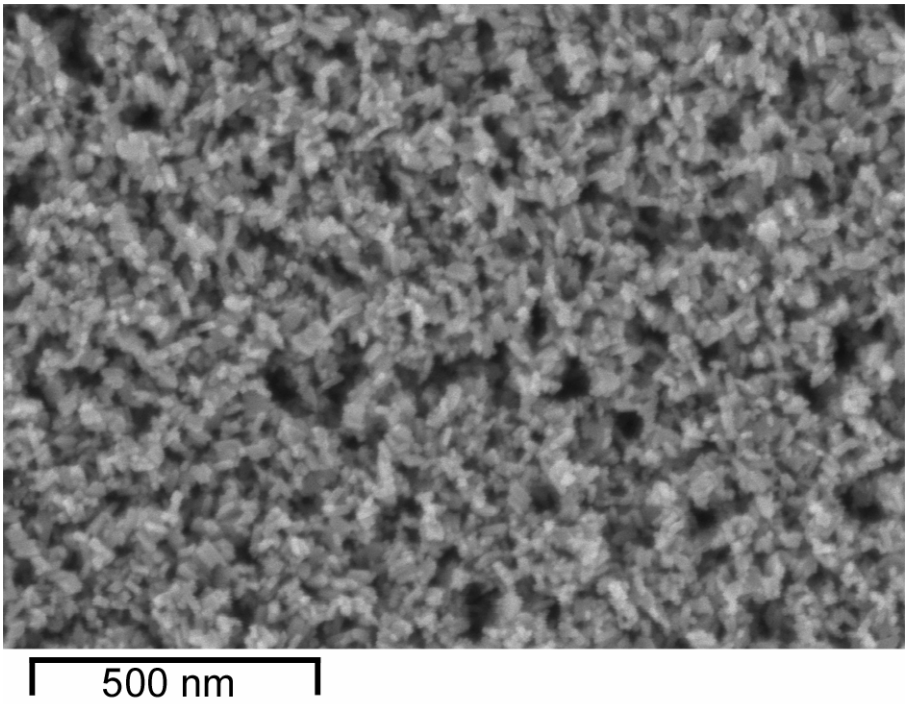

Figure 1.6. Conventional TiO_2 nanoparticle film.

Despite the adequate performance of nanoparticle films in conventional DSSCs, this photoanode geometry has several disadvantages. These include low porosity, lack of materials generality, and tedious particle synthesis. But the primary weakness of the NP photoanode is the extraordinarily small apparent diffusion coefficient, D_n. Electron transport to the TCO is often modeled as the trapping and thermal release of electrons from a distribution of sub-bandedge states. This process is highly dependent on the Fermi level, with TiO_2 nanoparticle films showing D_n of order 10^{-4} cm^2s^{-1} when electron concentration is similar to that at the power point.[22, 31] Using the Einstein relation

$$D = \frac{\mu \cdot k_B \cdot T}{q} \tag{6}$$

along with measured mobilities (μ) of 13 $cmV^{-1}s^{-1}$ for single crystal anatase TiO_2 [32], photoanodes with D_n of order 10^{-1} cm^2s^{-1} (i.e. a thousand times that in NP films) could be envisaged.

1.3.5. Strategies for Improving Photovoltage: Replacing I^-/I^{3-}

Strategies for improving the photovoltage at open circuit (V_{OC}) in DSSCs may be divided into two categories. The first strategy is to reduce the dark current (interception current) at a given photoanode Fermi level. The second is to push the counter electrode potential more positive by changing the redox couple to which its Fermi level is pinned, Figure 1.4. To further complicate matters, the two strategies are enmeshed, as (all else being equal) dark currents are anticipated to depend to some extent on the redox couple's potential. In any case, the photovoltage is the difference of the Fermi level for the counter electrode (fixed at the redox

shuttle potential, $E_{F,redox}$, if concentration polarization can be neglected) and the photo electrode, ${}_nE_F$.

$$q \cdot U_{photo} = {}_nE_F - E_{F,redox} \quad (7)$$

The V_{OC} of the most efficient DSSC to date is 850 mV.[23] In the absence of hot carrier injection, ${}_nE_F$ may not exceed the dye excited-state potential, thus limiting the V_{OC} to ~1.3 V in traditional I^-/I_3^- DSSCs, Figure 1.4. Clearly, even with I^-/I_3^- there is room for improvement based on the strategy of reducing dark current.

Further improvement of V_{OC} requires an alternative redox couple with a more positive potential, approaching the $dye^{0/+}$ potential (strategy 2). The optical gap of the Ru dye in the most efficient DSSC to date is ~1.8 eV, but the $dye^{0/+}$ potential differs from the I^-/I_3^- potential by ~500 mV.[10, 33] The potential difference is necessary to drive regeneration at an acceptable rate and is a consequence of the unusually large reorganization energy for I^-/I_3^-. While detrimental to regeneration, the large reorganization energy paradoxically is *beneficial* in terms of dark current minimization.

All reports of efficient (> 4% at 1 sun illumination) DSSCs to date have utilized the I^-/I_3^- couple as a dye regenerator and redox mediator. The uniquely good performance of I^-/I_3^- in these cells can be attributed to slow back electron transfer from TiO_2 to the mediator, maximizing V_{OC} in accordance with the diode equation. The I_3^-/ I^- couple, however, has a number of disadvantages, including the corrosive nature of the oxidized species toward a traditional silver current collection mesh, which inhibits the low cost commercialization of DSSCs. Further, the complex kinetics precludes a general understanding of the heterogeneous electron transfer

reactions in these photoelectrochemical systems. Additionally, the redox potential of I^-/I_3^- limits the maximum possible V_{OC} of the best DSSCs to 1.3 V owing to the roughly 500 mV of overpotential required for reduction of the oxidized dye as described above (see Figure 1.4). Attempts to increase the voltage by making the solution potential more positive require increasing the concentration of I_3^-, which simultaneously increases the rate of electron interception (lowers ${}_nE_F$), thereby preventing an overall V_{OC} improvement. Thus, in order to extract all the voltage available in a DSSC, alternative redox couples with potentials more closely matched to the dye oxidation potential need to be identified.

In general, one-electron, outer-sphere redox reagents such as ferrocenes have not been useful mediators in DSSCs.[34] Although such species often rapidly reduce the oxidized dye, these systems also have substantial dark reactivity, due to facile reduction of their oxidized form by electrons in the conduction band of the TiO_2. This rapid interception of electrons in the photoanode creates two distinct problems in the operation of a DSSC: loss of V_{OC} and diminished charge collection efficiency. The most well recognized detriment is the reduction in the V_{OC} in accordance with the diode equation. Unlike charge collection losses due to competing kinetic processes (Figure 1.5), slowing competing processes cannot circumvent this loss of V_{OC}. Since the light-generated current and dark current must be equal (and opposite) at open circuit, compensating for a dark-current induced loss of V_{OC} requires increasing the number of charges injected per unit time. In contrast, the loss of photocurrent (even under short circuit conditions) due to interception of diffusing electrons on their way to the TCO is controlled by a kinetic competition, shown in Figure 1.5c. This competition between charge lifetime (τ_n) and charge transport time (τ_d) has been extensively studied via both frequency and time resolved techniques.[13, 22, 35] The theoretical treatment, already introduced as Equation 1, is employed to

understand competition in DSSCs under steady state conditions. Using this formalism, the effects of accelerating electron interception (reducing τ_n) have been modeled as Figure 1.7. Initially, V_{OC} monotonically decreases with progressively shorter τ_n while the current density under short circuit conditions (I_{SC}) remains constant. Given sufficiently fast transport (short τ_n) only the effects of the increased dark current are visible in the I-V curve under illumination, i.e. lower V_{OC}. However, under conditions of even faster interception, or when the competition in Figure 1.5c becomes relevant, a loss of photocurrent is predicted. As must be the case for a system in which the collection efficiency approaches unity, τ_d has been shown to be significantly smaller than τ_n in systems in which I^-/I_3^- is employed. Yet, in many other DSSCs, the kinetic competition is relevant as evidenced in numerous reports of fast interception conditions.[34, 36, 37] In one particularly interesting example, DSSCs that used cobalt(III/II) tris(4,4'-di-*tert*-butyl-2,2'-bipyridyl), $[Co(t\text{-}Bu_2bpy)_3]^{3+/2+}$, as a redox mediator exhibited excellent efficiencies, while cobalt(III/II) tris(4,4'-di-methyl-2,2'-bipyridyl), $[Co(Me_2bpy)_3]^{3+/2+}$, systems showed poor performance.[38] If the *tert*-butyl group acts as a spacer group to slow electron interception, the performance difference could be due to τ_n being slightly larger than τ_n for $[Co(Me_2bpy)_3]^{3+/2+}$, but τ_n being slightly smaller than τ_d for $[Co(t\text{-}Bu_2bpy)_3]^{3+/2+}$.[39]

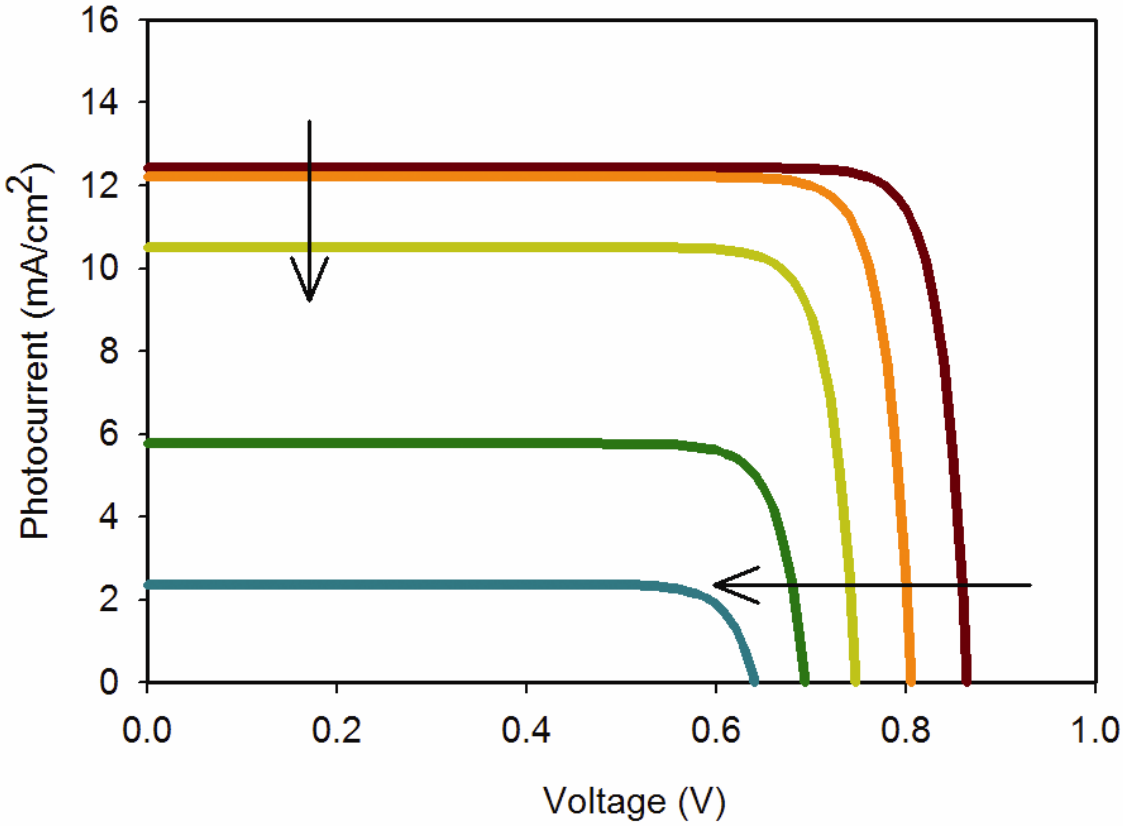

Figure 1.7. Current-voltage curves for DSSCs with progressively shorter charge lifetime (τ_n). Each line represents an order of magnitude faster interception. For simplicity, curves have been calculated assuming ideal behavior (diode quality factor of unity). Real DSSCs generally behave less ideally, exhibiting smaller fill factors and showing (or implying) even greater sensitivity of V_{OC} to τ_n variations.

Reducing charge collection losses at low applied potentials requires a photoanode that exhibits faster charge diffusion according to:

$$D_n = \frac{d^2}{4 \cdot \tau_d} \tag{8}$$

As previously discussed, D_n is surprisingly slow in NP thin films and dependent upon ${}_nE_F$, effects most readily explained by the activation energy of trapping/de-trapping required to facilitate charge hopping. The result is a potential dependence of both τ_n and τ_d (or equivalently, a light-flux dependence).

A related idea is to employ sensitizers with significantly larger extinction since this would allow equal light harvesting efficiency within a thinner photoanode. According to equation 8, a 10-fold reduction in photoanode thickness will reduce τ_d by 100-fold. Reducing the charge collection time in this manner has the same advantages as increasing D_n. Furthermore, a reduction in dark current is expected to accompany any decrease in surface area.

Building DSSCs with significantly faster charge transport kinetics should allow devices with a wider variety of redox mediators to be used. To date, successful experiments with only the very slowest of redox shuttles have been carried out. Studies of faster shuttles, notably ferrocene, have been characterized by almost complete device failure due to poor charge collection.[34] Alternative photoanodes should overcome this loss, as shown modeled in Figure 1.7, allowing for the further exploration of redox mediators including commercially attractive solid-state hole conductors.[40, 41] Furthermore, redox shuttles with more positive potentials may be studied, creating the possibility of voltages exceeding 1.0 V.

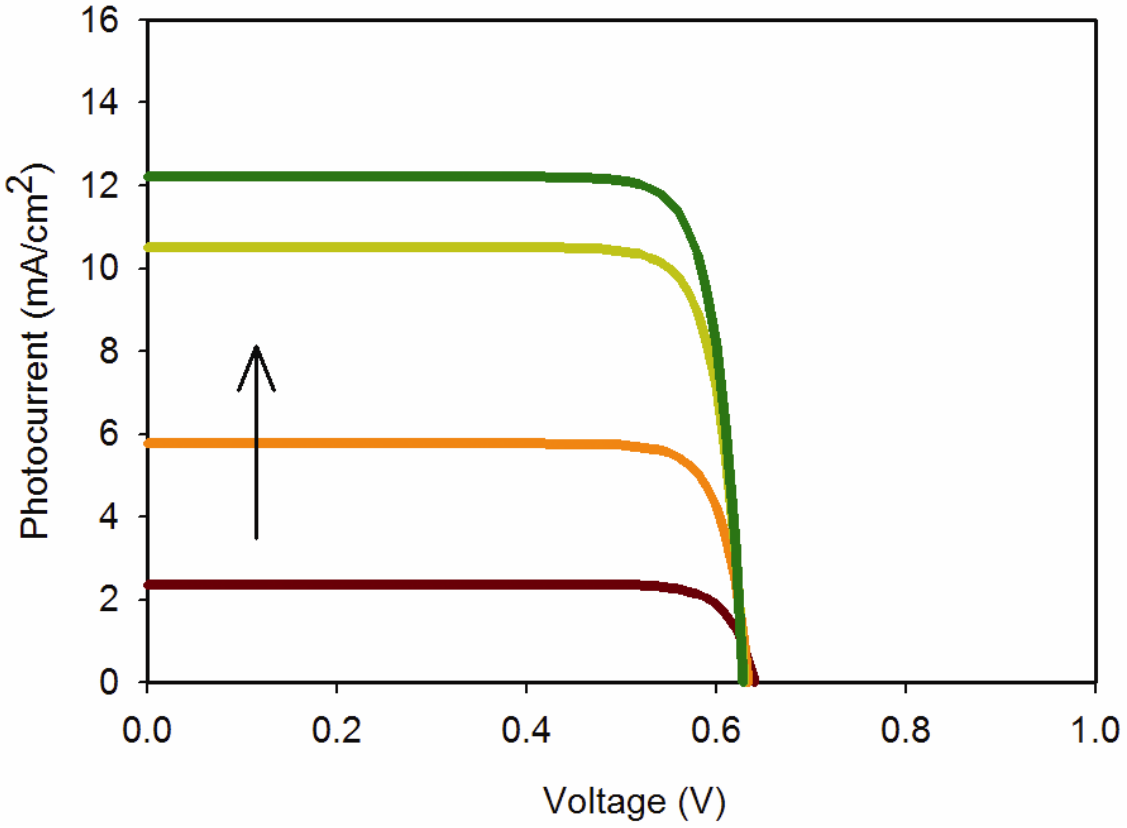

Figure 1.8. In devices with relatively short charge lifetimes (the shortest shown in Figure 1.7), charge collection at low applied potentials may be improved by increasing the diffusion rate. Each line represents an order of magnitude larger apparent electron diffusion coefficient (D_n).

1.3.6. Improving Photovoltage: Reducing the Dark Current

In the most efficient DSSCs, the primary recombination/interception pathway at open circuit is from electrons in the NP film to I_3^- in solution. In order to reduce the dark current at a given ${}_nE_F$, inorganic barrier layers, alkyl chain additions to the Ru dye, and co-absorbents have been utilized with moderate success.[19, 21, 42, 43] These physical barriers between semiconductors and redox shuttle comprise tunneling barriers, which attenuate the rate of electron transfer from the semiconductor to the shuttle.

A related notion centers on the reaction order for the electron interception process. For triiodide as the interceptor, the mechanism of this potentially multi-electron process is complex and controversial. In particular, the reaction order with respect to electrons is debated[30, 44]; nevertheless it is clear that the interception rate increases with increasing concentration of electrons in the photoanode. This implies that photoanodes with a lower density of states at a given ${}_nE_F$ will exhibit slower interception, all else being equal. This effect has been illustrated nicely by Haque et al. where the electrolyte composition was varied in order to shift the density of states which controlled the rate of electron interception.[18] The effect of reducing dark current on photovoltage may be modeled for an ideal photoanode using Equation 4. The result is an ~60 mV increase in V_{OC} with each order of magnitude reduction in dark current, Figure 1.9. In semiconductor electrodes with larger diode quality factor, the change is even more dramatic.

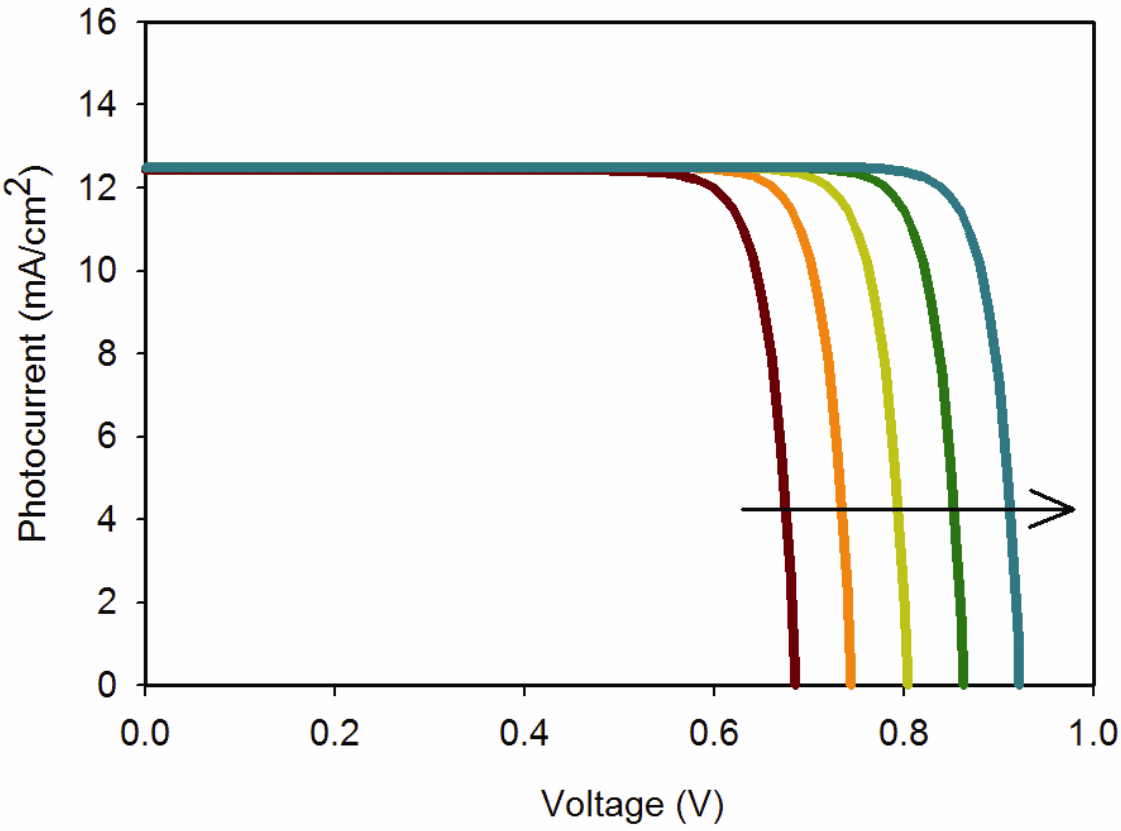

Figure 1.9. In ideal photoanodes, decreasing the dark current density increases the voltage at open circuit and at the power point. Each line represents an order of magnitude lower dark current density.

In nanostructured photoelectrodes, the relevant states likely comprise both conduction band states and trap states. Electron traps in TiO_2 arise mainly from "incorrectly" coordinated titanium ions found at intrinsic defect sites and surface sites, and near intercalated species. Both hydrothermal growth and ALD are expected to yield more pristine semiconductors with larger polycrystalline domains than found in NP films, thus reducing the number of trap states. It may be possible to further reduce the number of electron traps near the semiconductor surface by atomic layer deposition of a second material. For example, ultra-thin layers of insulators such as ZrO_2 are expected to react with and bury or "correct" the coordination of these sites while at the same time presenting a tunneling barrier to electron interception. Thus, fabrication of higher quality semiconductors and/or controlling the surface chemistry with ALD[43, 45] may lead to lower dark currents at a given ${}_nE_F$.

Novel electrode architectures may also influence the rate at which oxidizing redox equivalents interact with the semiconductor surface by altering the packing of chromophores. Like inorganic blocking layers, the dye itself acts to reduce the effective surface area of semiconductor exposed to the redox mediator.[19, 46] The extent of dark current reduction is dependent upon the size of the redox mediator and the porosity of the choromophoric monolayer. On flat surfaces, it has been shown that construction of chromophoric monolayers capable of blocking molecular species (while passing smaller ionic species, e.g. Li^+) is feasible.[47] As the length of choromophores is comparable to the pore size of high area photoelectrodes in many DSSCs, the curvature of the photoanode is likely to influence porosity. The convex interior surface of a tube is more likely to the block entry of oxidizing equivalents compared to the convex surfaces of particles and rods, Figure 1.10.

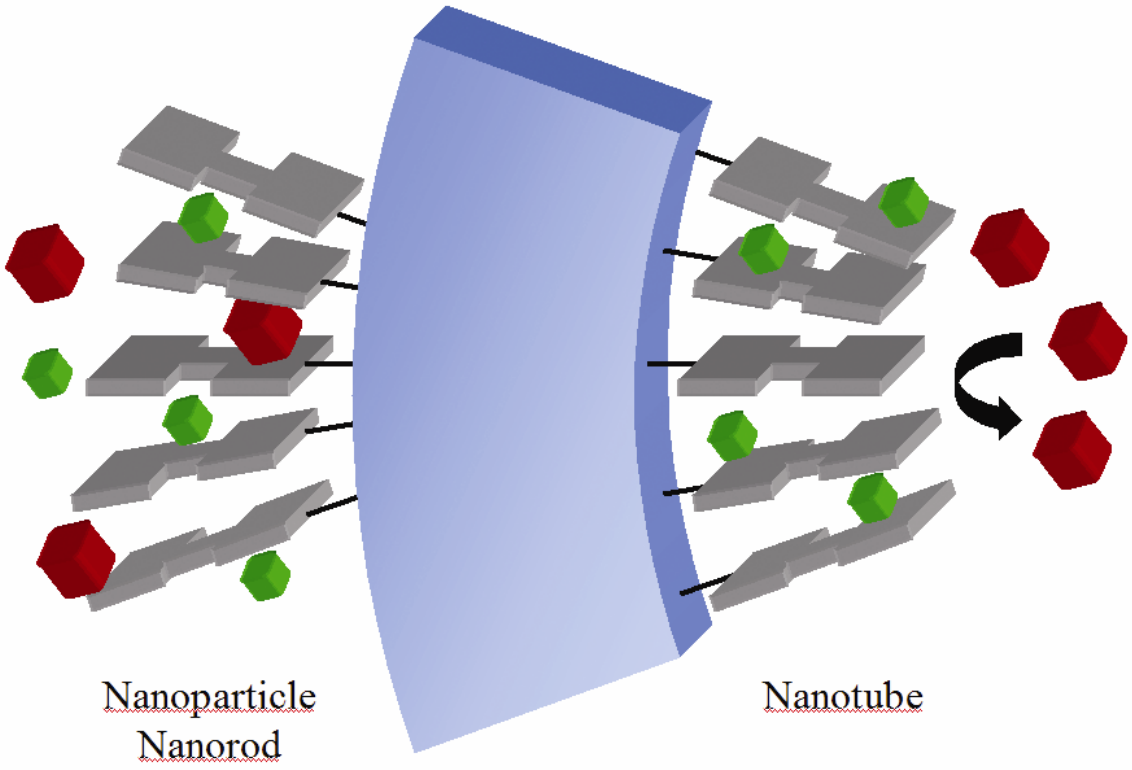

Figure 1.10. Idealized dyes bound to convex and concave surfaces may sieve different size species in solution, for example lithium ions (small, light green blocks) versus molecular redox shuttles (large, dark red blocks).

Novel photoelectrode architectures also should accommodate higher extinction chromophores. The porphyrin oligomer shown in Figure 1.11[48] comprises one example of a potentially strongly absorbing and broadly absorbing chromophore suitable for an advanced DSSC. This next generation of chromophores, with lengths in excess of 5 nm, will have difficulty permeating typical nanoparticle photoanodes. These new "super-chromophores" have the potential to significantly reduce dark currents in DSSCs by allowing an order of magnitude lower surface area photoanode to be used without loss of light harvesting efficiency.

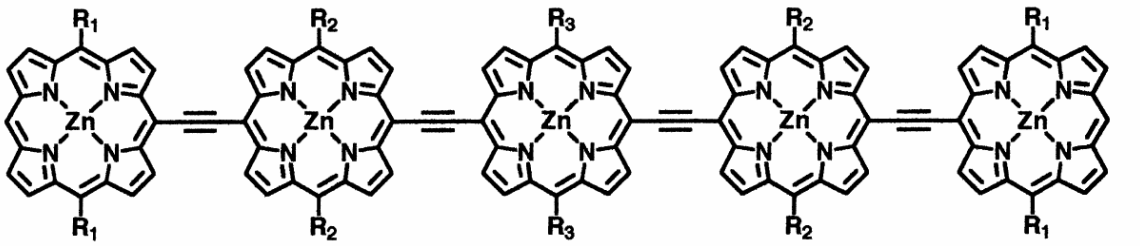

Figure 1.11. Porphyrin oligomers have greater extinction than traditional inorganic DSSC dyes. Incorporation of these larger chromophores will require a more porous photoanode.

1.3.7. Strategies for improving J_{SC}

The possibility of employing alternative redox mediators in DSSCs creates a cascade of new opportunities. The most exciting prospect is the ability to rapidly reduce an oxidized dye with smaller optical gap using minimal driving force. Since incident photon-to-current efficiencies already approach unity from 350-650 nm in the most efficient DSSCs, increasing the photocurrent requires extending dye absorption into the infrared. Under ideal conditions, a single junction solar cell with optical gap of ~1.4 eV (corresponding to 900 nm light) has the potential to generate 33 $mAcm^{-2}$. Comparison of this with the highest current reported to date for a DSSC (which employs the "black dye" Ru complex) of 21 mA/cm^2 indicates that there is much room for improvement if alternate redox couples can be utilized.[49]

There are two approaches to narrowing the dye's optical gap in order to collect a greater portion of the AM1.5 spectrum. Shifting the $dye^{*/+}$ potential less negative is one possibility, but the overpotential required for electron injection into the metal oxide at a rate sufficient to compete with radiative and nonradiative decay is already essentially optimized for a given photoanode material (Figure 1.5a). The second approach is to push the $dye^{+/0}$ level more negative; however this approach is subject to a combination of problems that have thus far limited its implementation. A more negative (less positive) $dye^{+/0}$ potential is expected to engender slower regeneration kinetics due, at least in part, to the lower driving force of the reaction. Further compounding the problem, recombination to oxidized ruthenium and osmium dyes has been shown (at least at shorter timescales) to be subject to Marcus "inverted region" kinetics.[50, 51] (At longer times recombination seems to be trap limited, so is insensitive to the $dye^{0/+}$ potential).[52-54] Therefore, shifting the ground state potential of the dye negative results in

a lower driving force and hence faster recombination. The concomitant problems of slower regeneration and faster recombination make the successful use of dyes that extend the spectral coverage in the current system extremely challenging.

Yet faster redox shuttles (that are incompatible with nanoparticle DSSCs) have already been shown to rapidly reduce oxidized dyes with less driving force.[34, 37] Therefore, we expect the application of faster redox shuttles to allow the competitive reduction of the oxidized form of smaller bandgap dyes, when combined with alternative photoanode geometries. These smaller band gap dyes may enable greater J_{SC}, pushing DSSCs performance closer to the still-distant thermodynamic limit.

1.4. Conclusions

Energy is an important resource for improving the human condition. Given that the current energy infrastructure is unsustainable, a new mix of renewable energy production is crucial to establishing our future health and security. In contrast to other renewable technologies, solar energy comprises a vast and nearly limitless supply that may be harnessed by photovoltaics. Dye-sensitized solar cells are a relatively new and potentially disruptive PV technology with the potential to make solar energy conversion competitive with coal fired generation.

By making feasible the use of faster redox shuttles and by (potentially) enabling new approaches to dark current suppression, new photoelectrode architectures and fabrication strategies are opening up the possibility for improvement of DSSCs that have been otherwise almost completely optimized. Under short circuit conditions these novel architectures with fewer traps may exhibit lower electron concentrations owing to faster charge transport to the TCO. Faster charge transport will enable a wide variety of redox mediators to be studied while

retaining reasonable charge collection efficiency. This may, in turn, allow dyes with greater spectral coverage to be employed in DSSCs.

Chapter 2. Electron Transport and Interception in ZnO Nanorod Arrays

2. Chapter Overview

In Chapter 1, the relevant electronic processes of the most efficient DSSCs to date were reviewed. Several approaches for advancing both understanding and efficiency in these promising PV were presented. In this chapter, the feasibility of accelerating charge transport in DSSC photoanodes is explored. Specifically, the nanoscale architecture and crystalline domain size is varied while employing the same wide bandgap semiconductor. A comparison of transport and interception dynamics for sintered nanocrystalline particle versus nanorod array electrodes of zinc oxide within operating DSSCs featuring the Grätzel group's ruthenium chromophore, "N719" is presented. Average electron transport times, τ_d, were evaluated by intensity modulated photocurrent spectroscopy (IMPS), while average recombination times were determined by intensity modulate photovoltage spectroscopy (IMVS).[1-4] The transport time and effective diffusion coefficient are inversely related:

$$\tau_d = \text{constant} \bullet L^2 / D_n \qquad (1)$$

where L is the thickness of the photoelectrode, and the magnitude of the constant (typically between 0.25 and ~0.4) depends on factors such as the uniformity (or not) of carrier generation through the thickness of the electrode.

Since the objective was to understand and compare dynamics, rather than maximize cell efficiency, optically dilute cells were employed. These provide for simplified behavior by allowing for uniform illumination/light-collection through the full depth of the photoelectrode. Using such cells, it is clear that nanorod geometries do offer substantial dynamical advantages relative to nanocrystalline particulate (NP) geometries.

2.1. Introduction

Compared to the most efficient nanocrystalline TiO_2 photoanodes, devices fabricated with ZnO electrodes show significantly lower conversion efficiencies (< 4%).[5-7] Yet ZnO DSSCs continue to be actively investigated due to the ease with which alternative and potentially superior high-area semiconductor morphologies may be fabricated. Particularly interesting are nanorod arrays.[8-11] Compared with standard photoanodes based on sintered nanocrystalline particles, a nanorod photoanode should show significantly faster electron transport, owing to a more direct path to the conductive glass electrode combined with fewer sites for trapping electrons.[8]

If one can avoid simultaneously accelerating back electron transfer from the photoelectrode to the dye or regenerator, speeding up electron transport provides opportunities for increasing performance of DSSCs in several ways. The useful thickness of a photoanode is determined by its effective electron diffusion length,

$$L_n = (D_n \tau_n)^{1/2} \qquad (2)$$

where D_n is the effective diffusion coefficient for the electron within the photoelectrode and τ_n is the survival time of the electron with respect to recombination to the oxidized dye or interception by the reducing species in solution. DSSCs employing solid-state hole-conductors in particular suffer from an L_n less than the thickness required to absorb the majority of incident light.[12] The result is low light harvesting efficiency (LHE) or poor charge collection efficiency (η_c), both of which limit the incident photon-to-current efficiency (IPCE) according to

$$IPCE = LHE \cdot \Phi_{inj} \cdot \eta_c \qquad (3)$$

where Φ_{inj} is the efficiency of electron injection from the excited dye into the semiconductor framework. Faster transport, therefore, can increase L_n and thus increase light harvesting efficiency and increase photocurrent.

In the most efficient liquid electrolyte DSSCs, L_n is already greater (at most wavelengths) than the thickness required to collect most of the incident photons. Here the value of faster transport (larger D_n) would be to make the cells tolerant to faster interception (shorter τ_n (Equation 2); recall that the electron collection efficiency is a measure of the competition between transport and interception/recombination). In principle, faster redox shuttles could then be employed. As dye regeneration by inherently faster shuttles need not be accelerated by large overpotentials, this change could directly address the problem of low photovoltage that has plagued DSSCs since their inception.

Work by Law and co-workers establishes that electron transport within isolated ZnO nanorods is indeed rapid.[8] However, this important earlier study does not directly address the dynamics of transport within operating solar cells nor does it examine recombination/interception dynamics.

2.2. Experimental

2.2.1. Materials

All photoelectrodes were prepared on fluorine doped tin oxide coated glass (8 Ω cm^{-2}). Nanocrystalline ZnO films were prepared using a commercial ZnO powder (Aldrich,

nanopowder, 99.999%) according literature reports.[13] A ZnO slurry was made by mixing ZnO powder and hydroxy propyl cellulose in distilled water followed by evaporation until the ZnO content reaches 6 wt %. Nanorod ZnO films were prepared via a two-step procedure similar to the various literature reports of ZnO nanorod arrays on conductive glass.[10, 14, 15] Briefly, RF magnetron sputtering of ZnO served to deposit a reproducible seeding surface upon which nanorod growth initiates. Growth of the rods was accomplished by immersing the slides in a 0.2 mM aqueous solution of $Zn(NO_3)_2$ adjusted to pH 10.3 with aqueous ammonia (28 wt %) at 65 ºC for 6 hrs in a sealed vessel. This typically yielded nanorod coatings showing a single morphology across the entire 15 x 25 mm slide that are 4.5 ± 0.2 μm high and 100-200 nm in diameter. Thicker samples were obtained by re-immersing the electrodes in a fresh growth solution, similar to previously reported methods.[10, 15] Active areas were patterned with nail polish. The remainder of the nanorod sample was dissolved in 10 wt% HCl (aq). The nail polish was washed away with acetone. The samples were sintered in air at 400 ºC for 0.5 hours and cooled to 100 ºC. The warm slides were submerged in N719 dye $(Ru(mpdcb)_2(SCN)_2 \bullet (^nBu_4N)_2$ where mbdcb is monoprotonated 4,4'-dicarboxy-2,2'-bipyridine) for 24 hrs. Film thicknesses were measured on a Tencor P10 profilometer. SEM images were collected on a Hitachi S-4500 cFEG SEM.

Cells were assembled according to literature procedures and infiltrated with an electrolyte solution containing 0.60 M butylmethylimidazolium iodide, 0.03 M I_2, 0.10 M guanidinium thiocyanate and 0.50 M *tert*-butylpyridine in a mixture of acetonitrile and valeronitrile (85:15). The active areas of NP and nanrod array devices were ~0.4 cm^2 and ~0.7 cm^2, respectively.

2.2.2. Instrumentation

Completed cells were illuminated by an array of high intensity blue LEDs (Nichia Corporation, 471 nm) driven by a Solartron 1260 frequency response analyzer (FRA). The dc light intensity was varied from 0.34 – 3.70 mW/cm^2 by changing the current through the LEDs. A 10% ac modulation was also applied to the LEDs via the FRA. For IMVS, the amplitude and phase shift of the modulated open-circuit photovoltage relative to the modulated illumination was measured directly by the FRA. For IMPS, the modulated short-circuit photocurrent was measured by a Solartron 1286 electrochemical interface and passed as a voltage to be read by the FRA. Data acquisition was performed using the GPIB output of the FRA attached to a personal computer.

2.3. Results and Discussion

2.3.1. IMPS and IMVS Theory

The protocol in photomodulation experiments is to systematically (sinusoidally) vary a small fraction of the light intensity, thereby systematically varying the number of charge carriers (i.e. injected electrons). The external electrical response – either the photocurrent at short circuit (IMPS) or photovoltage at open circuit (IMVS) – is then monitored as the modulation frequency is increased.[1, 2] At some point the electrical response begins to lag behind the optical perturbation, indicating rate-limiting dynamics for either charge transport or interception/recombination. A recent review by Peter details the usefulness of this technique in the study of DSSCs.[16]

It should also be noted here that photomodulation experiments are limited in several ways and have begun to be replaced by electrochemical impedance spectroscopy, the subject of

Chapter 4. The first disadvantage of the photomodulation experiment is the need for charge injection via illumination. This means the instrumentation is slightly complicated (i.e. the need for a fast, calibrated LED), the device must be reasonably efficient (since the signal is proportional the current density), and the experiment cannot be run in the dark (i.e. recombination cannot be ignored). Another disadvantage is the range of applied potentials over which the experiment can be run. The rate of interception may only be monitored under open-circuit conditions while the rate of electron transport can only be probed at short-circuit. Unfortunately, this provides no information about the most relevant applied potential – the power point – nor does it elucidate the two relevant parameters at the same applied potential, so that an effective diffusion length may be calculated. Nevertheless, the experiment is straightforward and useful for the relative comparisons discussed below.

2.3.2. Photoanode Characterization

Scanning electron microscopy (SEM) images of a sintered NP network (Figure 2.1a) and a nanorod array (Figure 2.1b) illustrate the differences in photoelectrode morphology. The sintered network consists of 20-200 nm diameter particles with similar size pores. The array comprises largely aligned rods of average length 4500 nm and of average diameter 150 nm, yielding an average aspect ratio of ~30. Previous reports have shown that ZnO rods prepared by similar hydrothermal methods are highly crystalline.[10, 14, 15] In the experiments described below, photoelectrode thicknesses have been approximately matched so that transport times can be directly compared and uncertainties associated with conversion to diffusion coefficients can be avoided.

a)

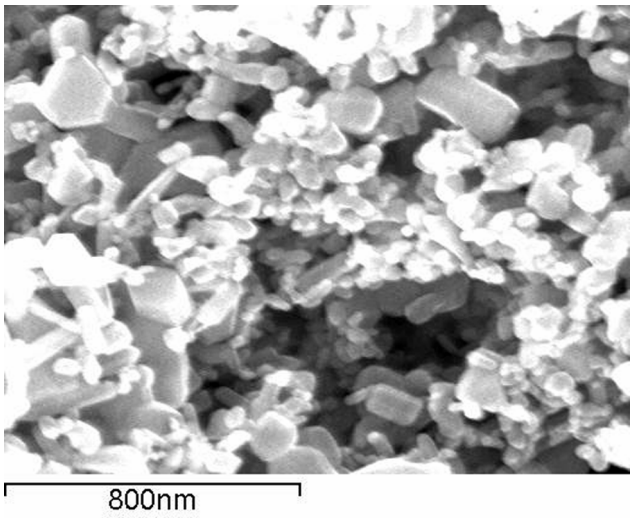

b)

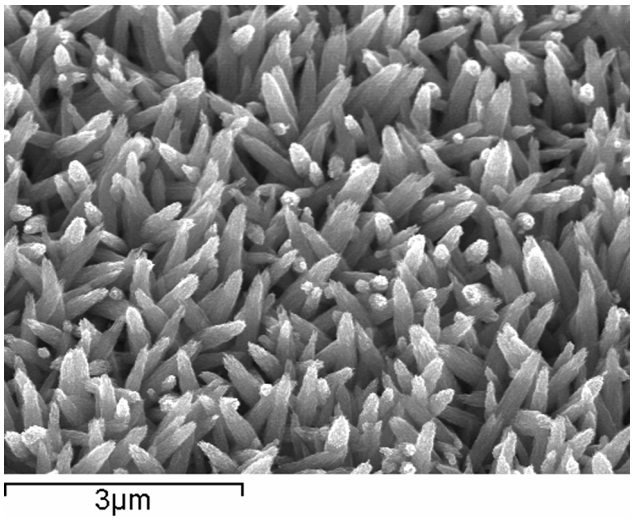

Figure 2.1. Scanning electron micrograph of a) nanoparticulate ZnO photoanode and b) ZnO nanorod array photoanode.

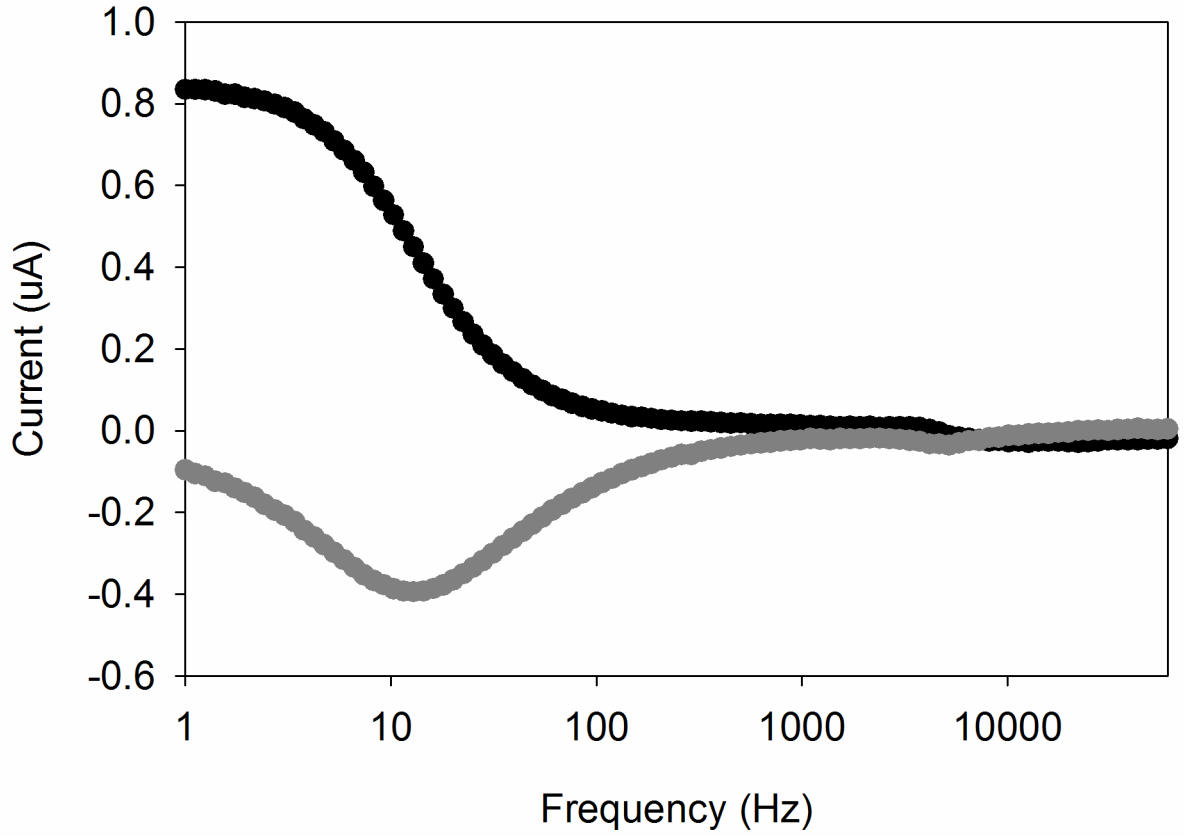

Figure 2.2. Real (black) and imaginary (grey) components of the photomodulated current for a 3.8 μm thick nanoparticle electrode as a function of modulation frequency.

2.3.3. Charge Dynamics

Figure 2.2 shows real and imaginary components of the photomodulated current for a 3.8 μm thick NP electrode as a function of modulation frequency, f (= ω/2π). The average transport time may be estimated from the minimum angular frequency in the imaginary plot:[1]

$$\tau_d = \omega_{d,min}^{-1} \qquad (4)$$

The value obtained is 12 ms.

Figure 2.3 shows the results of the same type of experiment, but now for a 4.5 μm thick nanorod array electrode. The striking feature is a shift of two orders of magnitude toward higher characteristic lag frequency, indicating that τ_d is two orders of magnitude shorter and the transport dynamics are two orders of magnitude faster for electrons within the nanorod array electrode. Closer examination shows that the current versus frequency plots deviate slightly from the expected sigmoidal and (approximately) Gaussian lineshapes for the real and imaginary components, respectively. Distortions are expected when transport becomes fast enough that other impedance elements, such as the cell series resistance (R) and the photoelectrode capacitance (C), limit the dynamical response of the photocell. To correct for these effects, the real and imaginary IMPS signals were divided by the complex attenuation function, A(ω):[4]

$$A(\omega) = \frac{1 - i\omega RC}{1 + \omega^2 R^2 C^2} = \frac{1}{1 + i\omega RC} \qquad (5)$$

As shown in Figure 2.3 (open symbols), the correction shifts the minimum frequency still higher, yielding an average transport time of 74 μs and indicating that electrons are transported ~160 times more rapidly through the nanorod array electrode than through the NP electrode. If corrections are made for the slight mismatch in thickness (transport is slower through thicker electrodes; see Equation 3), the difference in transport dynamics is even greater: ~220-fold.

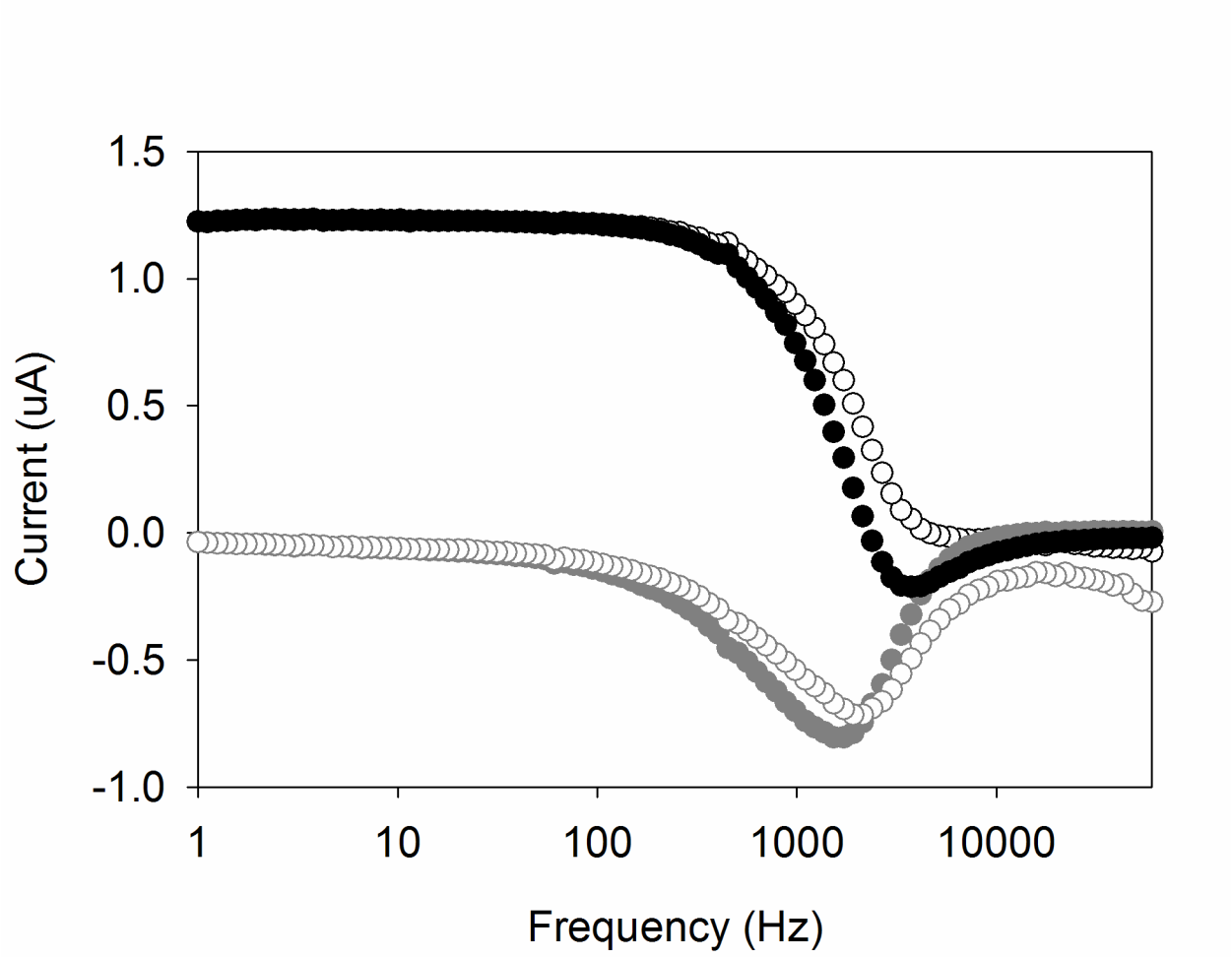

Figure 2.3. Real (black) and imaginary (grey) components of the photomodulated current for a 4.5 μm thick nanorod electrode as a function of modulation frequency. Open circles show the current corrected for RC attenuation (equation 4) where R and C are typical literature values, 15Ω and 30μF per cm^2.

The dynamics of interception can be evaluated from similar plots of real or imaginary contributions to the modulated photovoltage under open-circuit conditions.[1] Equating the observed angular frequency at the minimum imaginary photovoltage with τ_n^{-1}, we obtained average lifetimes of 47 and 170 ms, respectively, for the np and nanorod array electrodes at the light intensity used in Figures 2.2 and 2.3. These findings are significant because they clearly show that the enhanced transport obtained with the nanorod array geometry does not come at the expense of similarly enhanced interception dynamics. Indeed, charges live longer in the nanorod array geometry than in the NP geometry. (The difference may be due, in part, to differences in total electrode area. In general, the rate of electron interception by I_3^- accelerates when the electrode area increases. While we have not been able to quantify the difference, the areas of NP electrodes of a given thickness almost certainly are greater than those of nanorod electrodes of the same thickness.)

Figure 2.4 shows the dependence of dynamics on mean light intensity. The NP electrode behaves as expected: Electron transport and interception both accelerate with increasing light flux, but their ratio remains essentially constant ($\tau_d/\tau_n \approx 3.5$). Thus, reasonably efficient charge collection is achievable with L = 3.8 μm, but should be much less so with an optically thick electrode (e.g. L greater than, say, 10 or 15 μm).

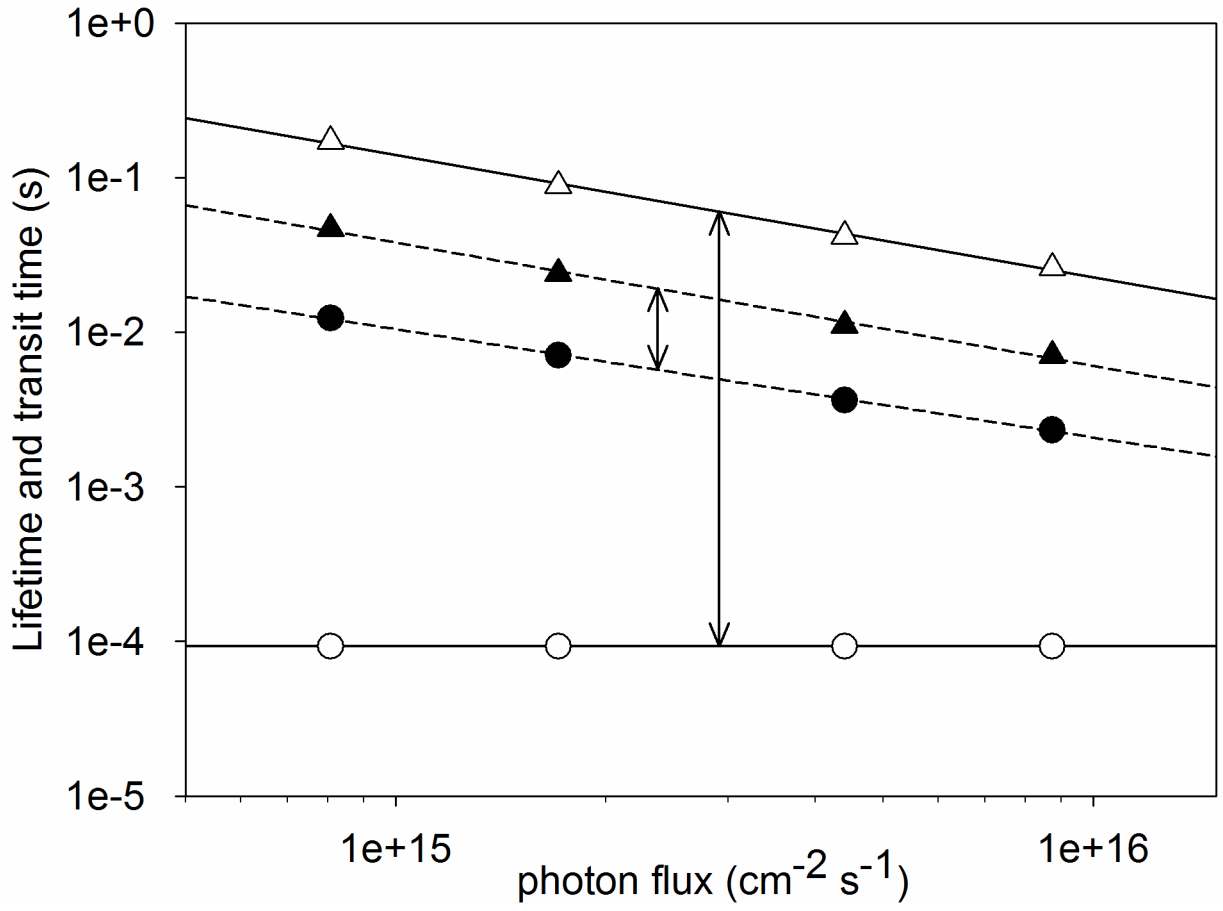

Figure 2.4. Electron lifetime (triangles) and average transit time (circles) over a range of illumination intensities. Arrows highlight the difference between τ_n and τ_d for nanoparticle (filled symbol) and nanorod (open symbol) devices.

For the nanorod array electrode, the dynamics of interception are similarly intensity dependent. The observed shorter lifetime at higher light intensity is expected because the local concentrations of reactant (injected electrons) is increased. Surprisingly, however, the dynamics of electron transport are insensitive to photon flux. The more typically observed enhancement of transport dynamics with increasing light flux has usually been explained by assuming that many electron traps exist and that they are distributed over a range of energies. Transport is thought to occur by a multistep process: occasional Boltzmann-governed thermal detrapping, followed by rapid movement through the conduction band until trapping occurs once again and the electron is largely immobilized.[17] At low light intensities, only the lowest energy traps are filled. At higher intensity, more electrons are present so more traps are filled and a smaller energy difference exists between the highest-energy filled traps and the conduction band. The smaller the energy difference, the more likely that transient detrapping (and electron transport) will occur. Phenomenologically, this behavior would be manifest as an increase in effective diffusion coefficient (decrease in transport time) with increasing light intensity.

That this behavior is *not* seen for the nanorod array electrode suggests either that all traps are filled, even at the lowest light intensity, or that traps are clustered around a single energy rather than being widely distributed in energy. (Typically an exponential distribution has been assumed.) Alternatively, a bottleneck unrelated to transport through the nanorod could conceivably exist. If so, then the measured transport times are only lower-limit estimates of the nanorod dynamics, i.e. the true times could be shorter and the true dynamics faster than indicated in Figure 2.4.

From Figure 2.4, the measured ratio of recombination time to transport time for the nanorod electrode varies from 280 to 1850. If the results are extrapolated to the number of

photons incident in the absorbing range of the dye under AM 1.5 illumination, the ratio becomes ~64 – or about 18 times that seen with the NP electrode geometry. Thus, nanorod array cells should be capable of sustaining efficient charge collection over much greater thicknesses than nanoparticle-based cells.

2.3.4. Device Performance

Finally, for completeness, we show in Figure 2.5 plots of photocurrents versus photovoltages for the two types of cells. We emphasize, however, that comparisons are complicated because differences in real area and in light harvesting efficiency for the two types of cells. Nevertheless, the observation of comparable photocurrent from the nanorod cell relative to the np cell, despite significantly lower light-harvesting efficiency for the nanorod cell points to more effective charge collection for the nanorod cell.

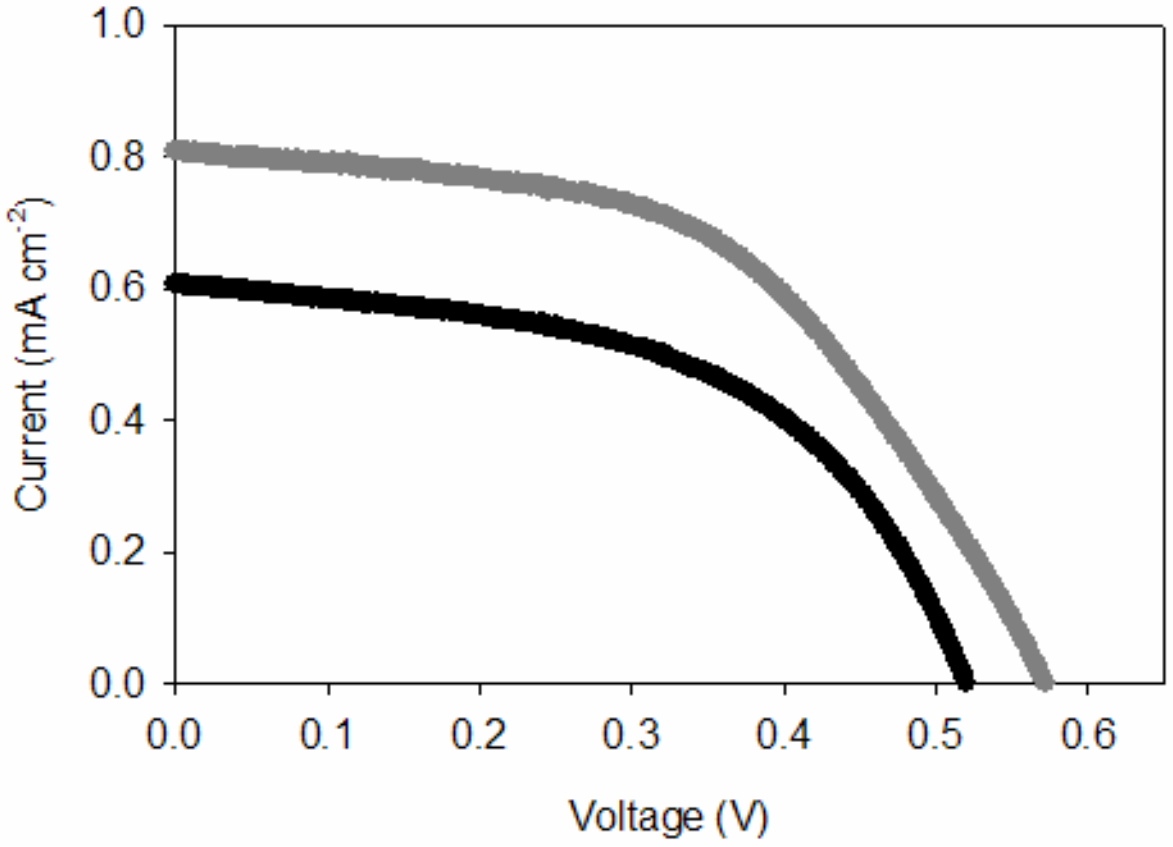

Figure 2.5. Plots of current versus voltage for NP (grey) and nanorod (black) cells under white light at approximately 1 sun. Note that dye loadings and, therefore, light-harvesting efficiencies, are low in both cases. Note also that the real area of the nanorod cell is significantly less than that of the np cell.

2.4. Conclusions

In summary, photomodulation experiments with dye-sensitized ZnO solar cells show that electron transport is tens to hundreds of times faster in nanorod array electrodes than in nanocrystalline particulate electrodes. Electron interception by triiodide, on the other hand, is slightly slower. Taken together, these findings support the contention that nanorod geometries are likely to provide very substantial dynamical advantages in operating dye-sensitized solar cells.

Chapter 3. ZnO Nanotube Based Dye-Sensitized Solar Cells

3. Chapter Overview

Chapter 2 described the synthesis and characterization of ZnO nanorod arrays operating as DSSC photoanodes. While fabrication of the reported architecture is straightforward, the aspect ratio (and therefore roughness) of the ZnO array is insufficient for ample light harvesting using common DSSC sensitizers. The inability of this ZnO nanorod arrays to collect a significant swath of the visible spectrum ultimately limits the power conversion efficiency of these otherwise promising systems. Furthermore, translation of the solution-phase growth method to the variety of metal oxides suitable for DSSC photoanodes is not clear. In this chapter I will describe a new photoanode design featuring higher aspect ratio sub-structures and having the potential for roughness factors (RF) greater than 1000 (although our initial studies are limited to RF $\leq$ 450). The design implementation strategy combines anodic aluminum oxide (AAO) templating and atomic layer deposition (ALD) to yield oriented arrays of electrically interconnected semiconductor nanotubes. Because it is both a stepwise and conformal coating technique, ALD provides exceptional control over nanoscale device composition and architecture. The large number of metal oxides accessible by ALD (including, but not limited to, TiO_2, ZnO, SnO_2, ZrO_2, and NiO) makes the technique potentially very widely applicable for the development of new photoelectrodes. In this chapter I demonstrate the viability of ZnO versions of these structures as dye sensitized electrodes (shown schematically as Figure 3.1) by characterizing their morphology, light harvesting efficiency, and photovoltaic performance.

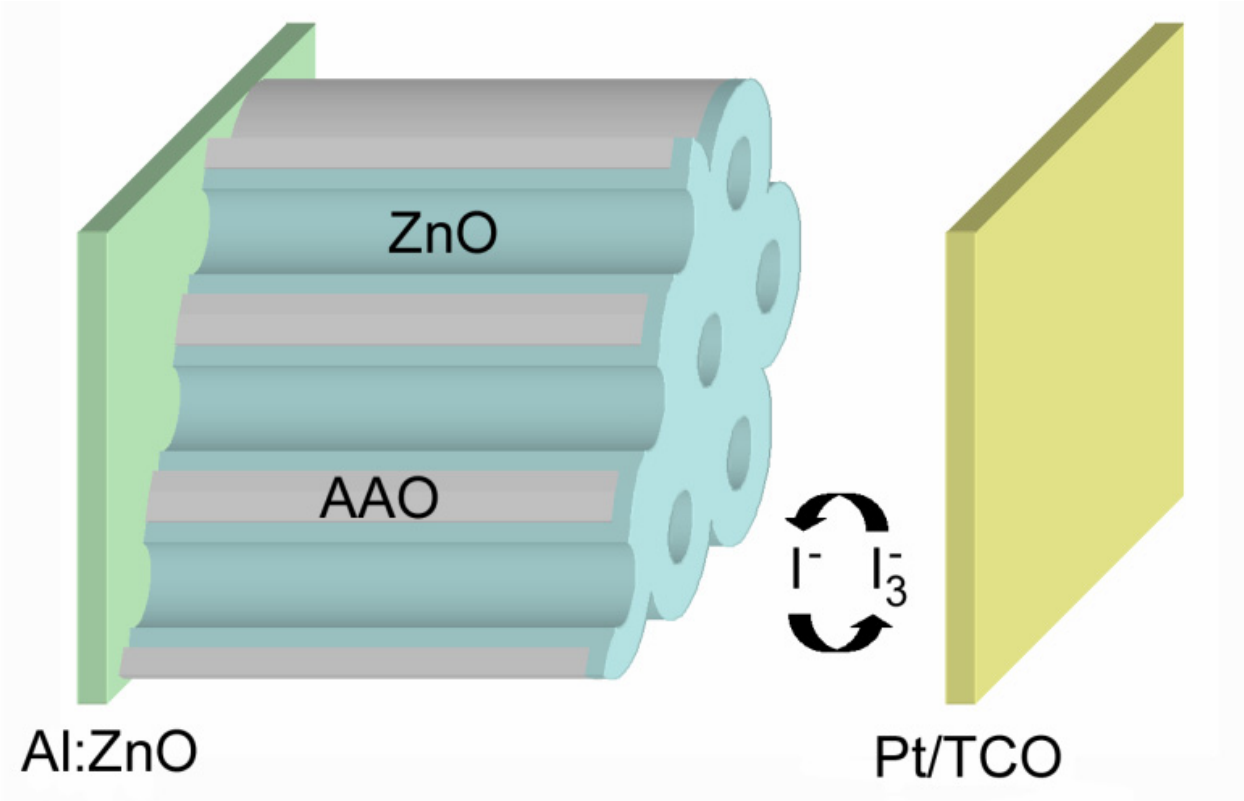

Figure 3.1. Schematic representation of proposed ZnO nanotube device architecture.

3.1. Introduction

The good light harvesting efficiency of the best DSSCs is the product of a dye with moderate extinction and a photoanode of high surface area (~1200 times the area of a flat electrode). This combination allows for ample absorbance over the majority of the visible spectrum with room for improvement in the red wavelengths.[1] In the most efficient cells, the photons intercepted by these molecular dyes create excitons that split on the tens of femtoseconds time scale resulting in charge separation efficiencies approaching unity.[2, 3] The efficiency of the final step, charge collection, is governed by the difference between the rate of charge transport and the rate of electron interception by I_3^- (or less likely recombination to dye^+). In order to compete with relatively slow (millisecond) transport through the nanoparticle network an exceedingly slow redox shuttle such as iodide/triiodide must be employed to hinder electron interception.[4] Thus, prototypical DSSCs, based on TiO_2 and iodide/triiodide, exhibit very good electron collection, despite small apparent electron diffusion coefficients. This remarkable behavior is important in accounting for the record high efficiency (~11%) of these cells.[1]

In order to push device performance beyond its current limits, a faster redox shuttle (that requires a smaller overpotential to reduce the oxidized dye) may be employed to increase the photovoltage (provided that dark current in not enhanced). Alternatively, a higher surface area framework would increase light harvesting efficiency and, therefore, photocurrent. Successful implementation of either scenario will require slowing charge recombination. Methods to decrease the rate of parasitic reactions with the redox shuttle include inorganic barrier layers on the metal oxide framework and modification of the dyes.[5-7] A faster redox shuttle or higher surface area framework may also require faster charge transport though the metal oxide framework to allow for complete charge collection under cell operating conditions. Indeed,

simply replacing iodide/triiodide with faster shuttles, but without implementing other changes, has been shown to *decrease* power conversion efficiencies due to the emergence of electron collection problems.[8, 9] To this end, several novel photoanode architectures have been fabricated, including but not limited to hydrothermally grown ZnO nanorod arrays, electrodeposited ZnO platelets, and TiO_2 pores formed via titanium anodization.[10-12] Due to their lower trap density and more direct path to the current collecting electrode, arrays of nominally 1-D nanostructures are expected to speed charge migration without adversely affecting interception. In the most successful application of this idea to date, a 1.5% efficient ZnO nanorod array has been shown to exhibit much faster transport than nanoparticle networks.[10, 13, 14] The efficiency of the nanorod devices, however, is limited by low light-harvesting efficiency. Increasing the surface area of the nanorod array depends on growing higher aspect ratio rods via hydrothermal methods, which remains a significant technological challenge.[15]

3.2. Experimental

3.2.1. Fabrication

A nominally 60 μm thick membrane with 200 nm pores that is 25-50% porous (Anodisc, Whatman) was coated with ZnO by atomic layer deposition via alternate exposure to diethyl zinc and water at a temperature of 200°C using reactant exposure times of 6 s and nitrogen purge periods of 5 s between exposures.[16] The membranes were fired at 400ºC in air for 30 minutes to increase crystallinity. A 1 μm thick electrode composed of transparent, conductive aluminum-doped zinc oxide (AZO) was deposited on one side by ALD. The commercial AAO membranes chosen for this study have pores that narrow to 20 nm within the last micron of thickness of one side. During AZO deposition, a steel fixture masked all but the small-pore face of the

membrane. To improve the electrical contact to the AZO coating, 100 nm of Au was evaporated onto the coating along the edges of the AAO membrane.

After heating to 200ºC and subsequent cooling to 80ºC the warm membranes were introduced to 0.5 mM $(Bu_4N)_2$[Ru(4,4'-(COOH)-2,2'-bipyridine)$_2$(NCS)$_2$] ("N719", Dyesol, B2 dye) in ethanol for 30 min followed by a quick rinse with acetonitrile. A 50 μm thick Surlyn frame was sandwiched between the open-pore side of the membrane and a platinized fluorine-doped tin oxide (FTO) electrode. Light pressure was applied at 130ºC to seal the cell. A solution of 0.5 M LiI, 0.05 M I_2, and 0.5 M *t*-butylpyridine in 3-methoxypropionitrile was introduced into the cell via vacuum backfilling through a hole in the FTO electrode. Additional Surlyn and a microscope cover slip sealed the electrolyte into the cell.

3.2.2. Instrumentation

Monochromatic illumination was achieved through the excitation monochromator of a Jvon-Ybon fluorescence spectrometer. Incident-photon-to-current-efficiencies (IPCE) were measured with a CH Instruments 1202 potentiostat. Active areas were limited to 0.28 cm^2 by the Surlyn frame and were additionally masked from illumination by black electrical tape to the same size. AM1.5 efficiencies were measured on a Class A solar cell analyzer from Spectra-Nova Technologies with a power of 906 W/m^2. To better understand charge collection, cells were also illuminated through the Pt/FTO electrode, which attenuated ~20% of the light at visible wavelengths due mostly to Pt absorption. For an identical batch of photoanodes, dye loading was quantified on a Varian Cary 5000 by measuring the absorbance of N719 desorbed from the membranes by 10 mM KOH.

3.3. Results and Discussion

3.3.1. Anodic Aluminum Oxide Template

As an inert, robust, and colorless framework, anodic aluminum oxide is an ideal foundation for solar cell electrodes. A large literature exists describing the theory and methodology for fabricating freestanding AAO membranes with hexagonally ordered pores ranging in size from 10-300 nm and pore densities in excess of 100 billion pores/cm^2.[17-19] For this study, commercial membranes were selected for their ready availability. Limitations of commercial membranes include ill-defined pore ordering, strong scattering of visible light, and restriction to only a few pore sizes and lengths. Geometric consideration of hexagonally arranged pores allows roughness factors to be estimated from:

$$RF = \frac{4\pi}{\sqrt{3}} \frac{rl}{d^2} \qquad (1)$$

where r, l and d are the pore radius, membrane thickness, and center-to-center pore spacing, respectively. Although poorly ordered, an average pore diameter of 210 nm, spacing of 329 nm, and length of 64 μm were estimated by SEM, giving RF ≈ 450. This compares well to the measured BET surface area of 487 cm^2/cm^2 of the membrane.

3.3.2. Photoanode Characterization

As expected for an ALD sequence entailing sufficient exposure times, the resulting polycrystalline ZnO film is continuous and conformal, Figure 3.2. Measurements of the resistance through the 64 μm thickness of the membrane (~48 Ω, 8 nm thick ZnO) provide additional evidence that coatings span the length of the pores. As-deposited, ALD ZnO has

numerous oxygen vacancies that make films moderately conductive and account for the relatively low resistance. The polycrystalline nature of the ZnO films may be directly observed by SEM and is corroborated by X-ray diffraction data. Both methods suggest a grain size of ~20 nm.

As shown in Figure 3.3, a thick coating of AZO was applied selectively to one side of the membrane by ALD. The combination of narrow pore termini and short exposure times (0.15 s) prevented the typically conformal deposition technique from significantly coating the pore interiors.

As shown in Figure 3.4, reducing *r* by coating the pores reduces the dye loading, in agreement with surface area calculations. The peak absorbance is 0.71 at 500 nm for a 2 nm coating of ZnO and decreases with increasing thickness. As expected, the modest RFs (~1/3 those of the best DSSCs) results in relatively low overall light harvesting efficiencies that we expect to limit photocurrent densities.

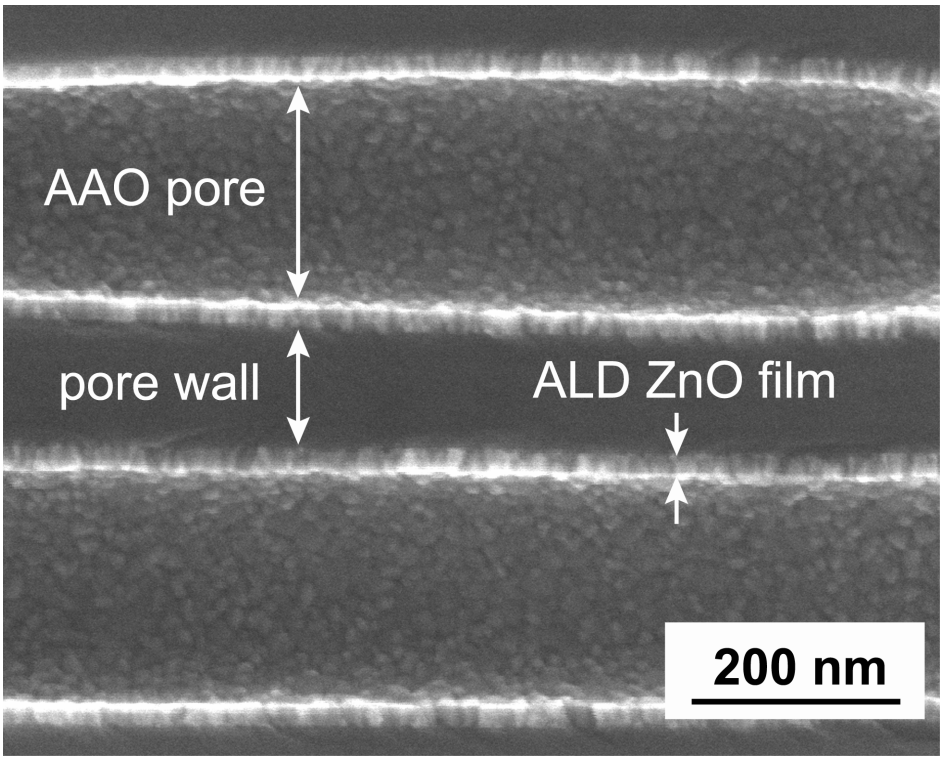

Figure 3.2. Cross-sectional SEM image of commercial AAO membrane pores coated with 20 nm of ZnO by ALD.

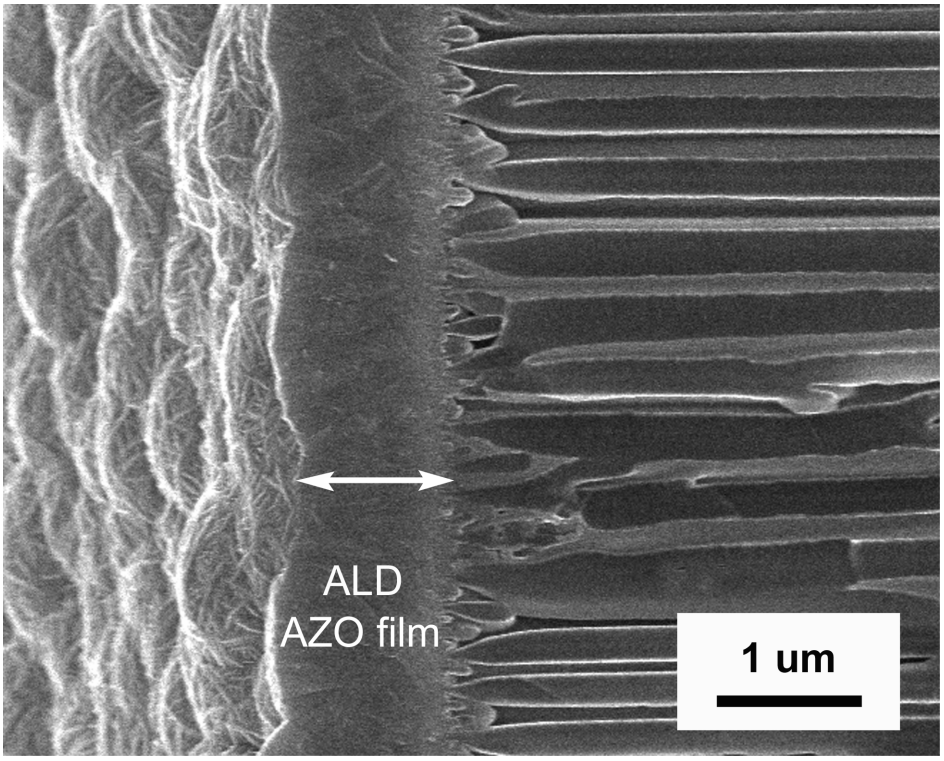

Figure 3.3. Cross-sectional SEM image of commercial AAO face coated with transparent conductive oxide AZO.

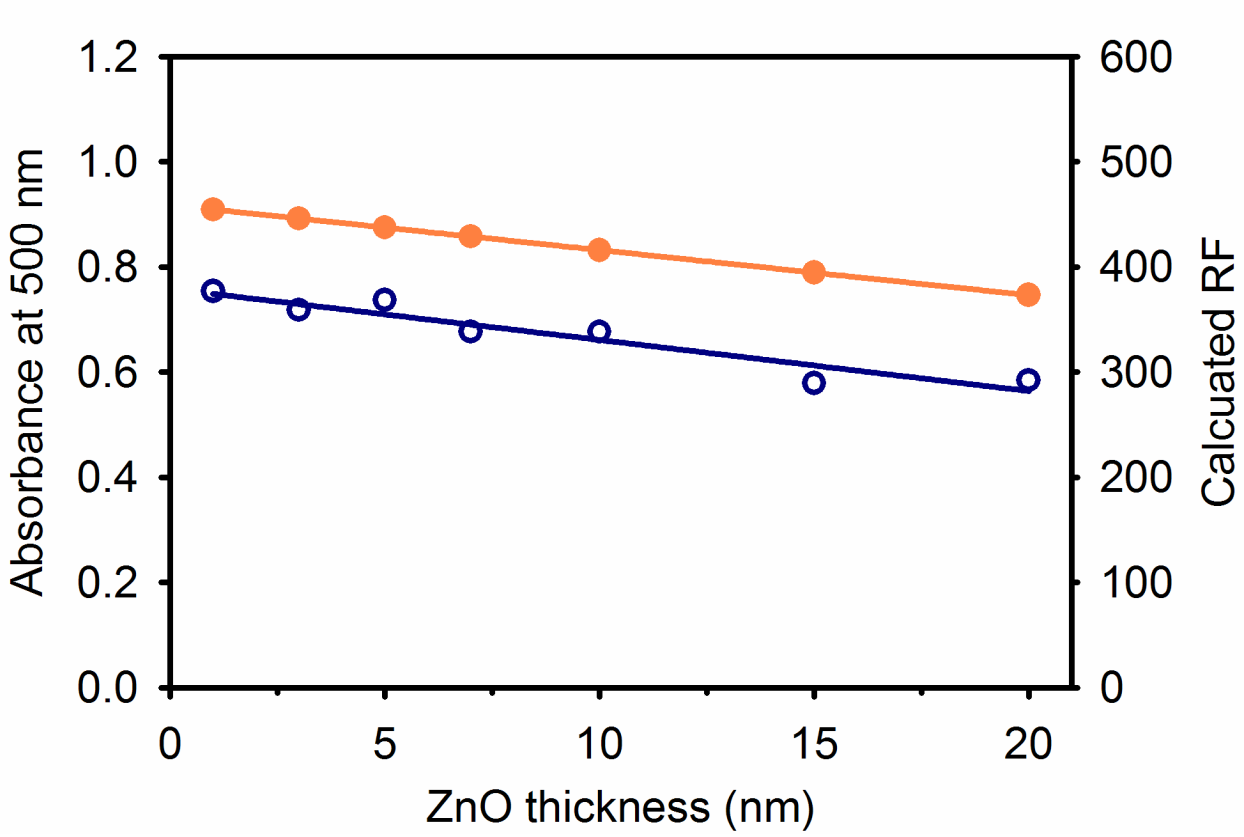

Figure 3.4. Absorbance of desorbed dye at 500 nm (blue, open symbols) and calculated roughness factor (orange, closed symbols). Lines are best linear fits to the data.

3.3.3. Device Performance

Figure 3.5 shows the short-circuit photocurrent densities (J_{sc}) for a series of devices with increasing nanotube wall thickness. In the control device, lacking ZnO, J_{sc} is extremely low. This is not surprising given that the useful surface area is similar to that of a flat electrode. With the thinnest tube walls relatively small amounts of charge are collected by the AZO electrode, most likely due to a combination of slow charge transport through the ZnO and accelerated recombination owing to high steady-state concentrations of dye-injected electrons. As the nanotube walls thicken, electrons flow more freely and J_{sc} rises sharply. Subsequent tapering with thicker walls is consistent with decreasing dye loading (Figure 3.4).

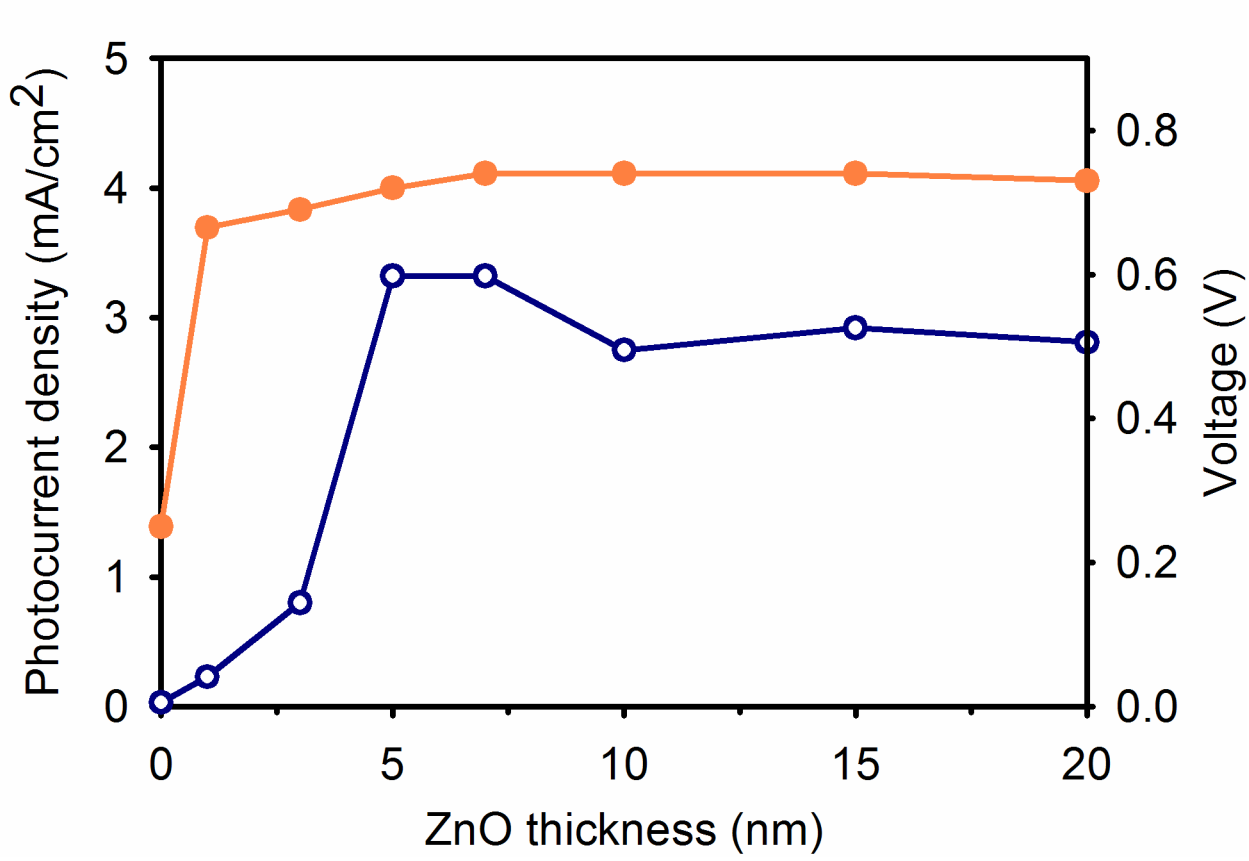

Figure 3.5. Short-circuit photocurrent (blue, open symbols) and open-circuit photovoltage (orange, closed symbols) as a function of ZnO wall thickness.

The photovoltage at open circuit (V_{oc}) rises sharply after deposition of only 1 nm of ZnO. The exceptionally low voltage in the absence of ZnO is likely caused by the direct contact of the redox shuttle with the heavily doped AZO layer, whose conduction band (in contrast to ZnO's) is unable to fix the cell photovoltage. The photovoltage increases with increasing ZnO wall thickness until it plateaus after 7 nm. This V_{oc} (739 mV) exceeds that of the highest previously reported ZnO DSSC photovoltages (ca. 670 – 710 mV).[10, 20] The excellent photovoltage is most likely not a result of improved charge transport, but a consequence of the low area of transparent conducting oxide (TCO) exposed in the new device geometry. While many TiO_2 based DSSCs employ a dense blocking layer or $TiCl_4$ treatment to inhibit the parasitic reaction of the redox shuttle at the TCO, there is little precedence for this type of passivation in ZnO systems. For the photoanodes of interest here, an increasing ZnO film thickness serves a second function, namely to narrow the nominally 20 nm pores directly adjacent to the TCO. An increase in photovoltage coincides with tapering these small pores until the photovoltage peaks around the thickness expected to completely restrict electrolyte access to the TCO. Inhibited recombination via the TCO in addition to a significantly smaller (~1/3) ZnO surface area for recombination, relative to nanoparticle films, may explain the superior V_{oc}. The V_{oc} value observed here, while high, is still about 200 to 260 mV less than the maximum theoretically obtainable based on the difference of redox-shuttle and dye-excited-state potentials. In principle, it should be possible to capture some fraction of the remaining 200 to 260 mV by suppressing dark current (slowing charge recombination). Deposition of a barrier layer[6] may be one way to achieve such a result.

Insight into the improvement of cell performance with increasing ZnO layer thickness may be obtained by investigating charge carrier lifetimes. Analysis of the photovoltage decay

affords electron lifetimes (τ_n) related to the slope of the photovoltage vs. time plot by the expression

$$\tau_n = \frac{k_B T}{q}\left(\frac{dV_{OC}}{dt}\right)^{-1} \qquad (2)$$

where k_B is the Boltzmann constant, T is the absolute temperature, and q is the positive elementary charge.[21] Electron lifetimes as a function of photovoltage are shown for two ZnO film thicknesses, Figure 3.6. Compared to other ZnO devices, the photovoltage decay of the best ZnO nanotube devices are similar.[22] At equal potentials (0.6 V), electron lifetimes increase as a function of ZnO pore wall thickness up to 9 nm, inset Figure 3.6. The trend is striking and parallels the behavior shown in Figure 3.5 (i.e. increasing J_{sc} with increasing ZnO layer thickness). Whether this reflects an intrinsic change in ZnO reactivity with increasing thickness, or simply better blockage of electron recombination from exposed TCO, has yet to be established.

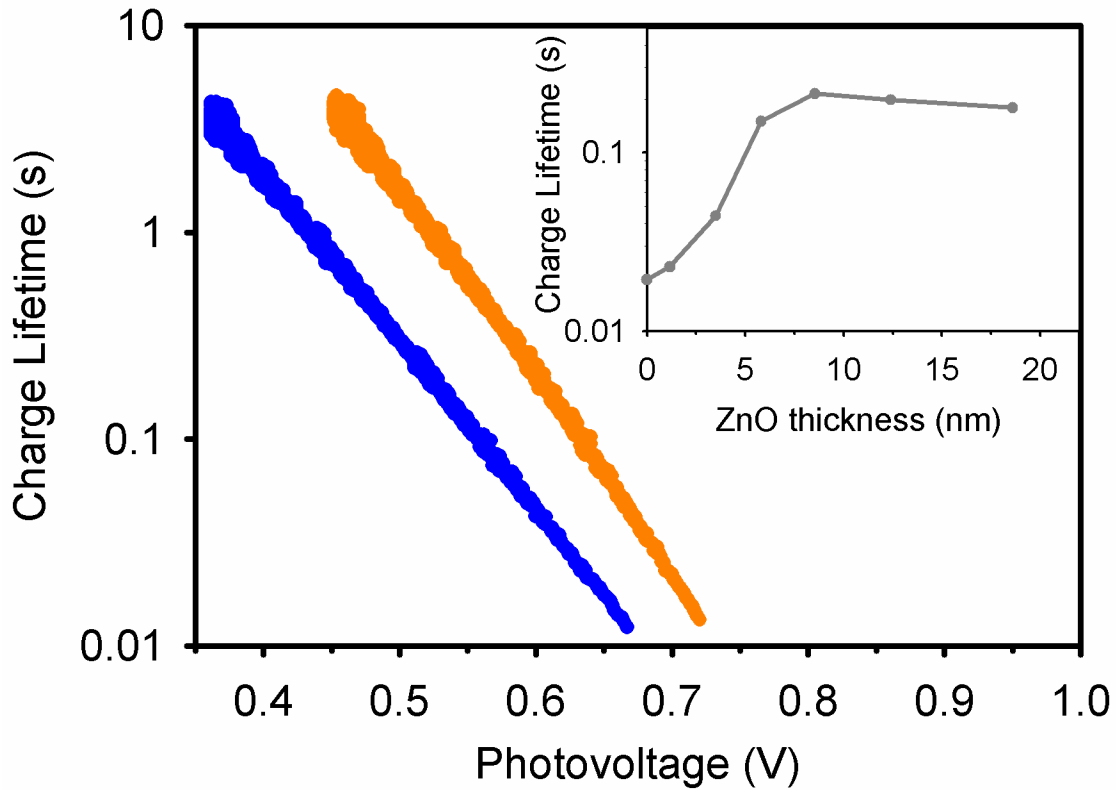

Figure 3.6. Charge lifetime vs. photovoltage for a device with 4 nm pore wall (blue) and 9 nm pore wall (orange). Inset shows charge lifetimes as a function of pore wall thickness at equal cell potential (600 mV).

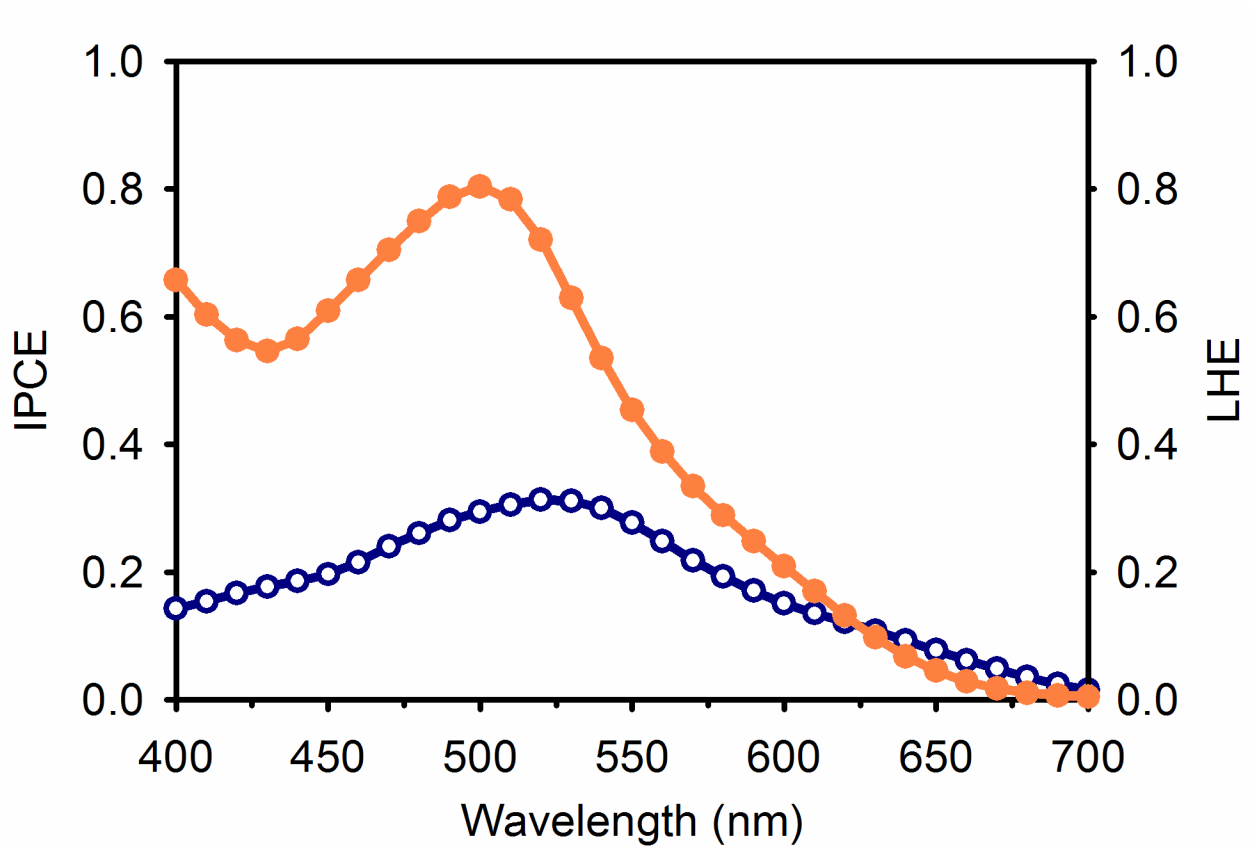

Figure 3.7. The incident-photon-current-efficiency (blue, open symbol) and light harvesting efficiency (orange, closed symbols) of ZnO cell with 5 nm pore wall.

Figure 3.7 shows the peak in LHE at 500 nm, characteristic of N719. As expected for an electrode of modest surface area, a small fraction of the AM1.5 spectrum is absorbed by the cell. The peak incident-to-photon-efficiency (IPCE) occurs 20 nm red-shifted from the apparent LHE peak evaluated with desorbed dye. Necessarily neglected in the LHE evaluation are additional effects due to reflection and scattering by the commercial membranes.

Under AM1.5 illumination the most efficient cell gives a J_{sc} of 3.3 mA/cm^2, V_{oc} of 739 mV, and fill factor (FF) of 0.64, yielding an overall conversion efficiency of 1.6%, Figure 3.8. To our knowledge, the FF is the highest yet measured for a ZnO DSSC. Clearly, the overall efficiency of this system is limited primarily by the photocurrent. The relatively low photocurrent is a result of several factors including small RF, photoanode reflectivity/scattering, and either (or both) low injection yield + charge collection efficiency. In the most efficient DSSCs a scattering layer of large particles is intentionally deposited on top of a transparent semiconductor network to reflect light back into the transparent electrode.[1] Yet photoanodes that are scattering throughout, as is the case in the current devices, show high reflectivity and poor light harvesting.[23] Finally, ZnO DSSCs generally exhibit much smaller absorbed-photon-to-current-efficiencies than do similar TiO_2 cells (implying inefficient electron injection and/or collection). We reasoned that the reduced dimensionality of the nanotube array electrodes, relative to nanoparticulate electrodes, would allow for efficient charge collection over long distances (50 μm) due to more rapid electron transport (as previously shown for nanorod arrays[13, 14]). That the nanotube arrays indeed can collect charge with equal efficiency over the entire length of the tubes was established by evaluating photocurrent densities based on backside illumination, Figure 3.9. If correction for light losses of ca. 20% due to the dark electrode were

to be made, identical J_{sc} values to front-side illumination would be obtained. As expected, the increase in collection efficiency correlates closely with the increase in electron lifetime.

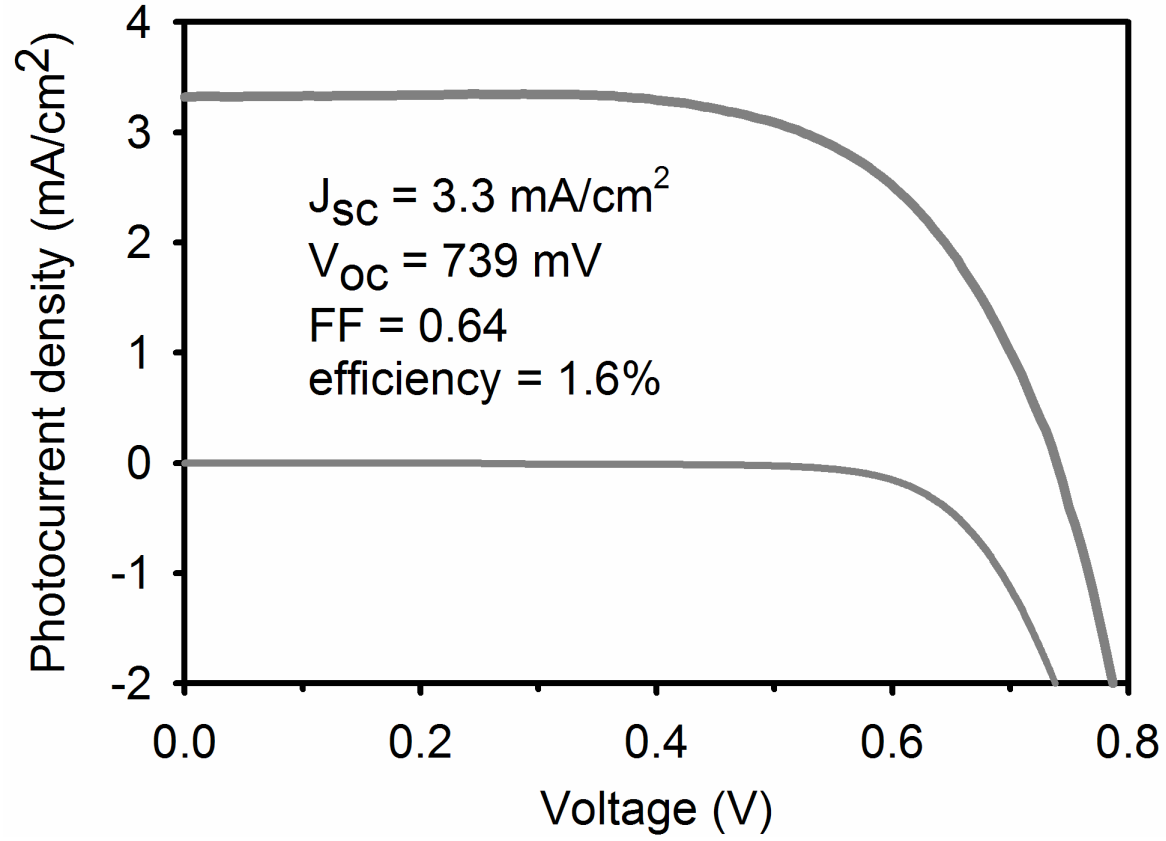

Figure 3.8. I-V curve for the most efficient cell, 7 nm ZnO, under simulated AM1.5 illumination.

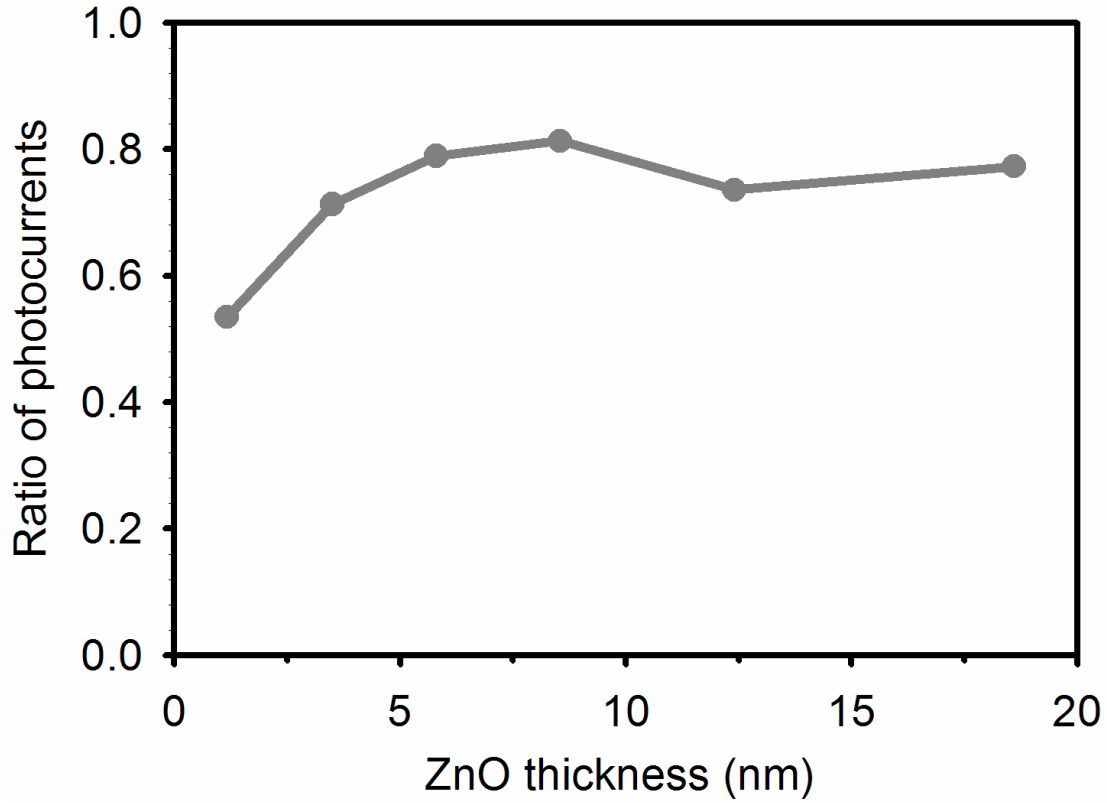

Figure 3.9. Ratio of photocurrents, backside versus frontside illumination. The ratio has *not* been corrected for light loss (ca. 20%) through the platinized counter electrode under backside illumination.

3.4. Conclusions

ZnO nanotube arrays embedded in a porous alumina template by atomic layer deposition have been combined with AZO coatings to generate relatively high area photoelectrodes (RF = 350-450). The electrodes have been incorporated into dye-sensitized solar cells where they display reasonable light harvesting efficiency, excellent photovoltage, and good fill factors in addition to moderate power efficiency. While the new nanotube cells compare favorably with other ZnO-based DSSCs, increased surface area (ca. 3-fold or more) will clearly be needed in order to obtain overall energy conversion efficiencies approaching that of the best ZnO cells (4%).[20] Current work is focused on determining the extent to which the substantial optical + structural advantages of custom-made membranes can be translated into better photoelectrode performance. Finally, in contrast to other nominally 1-D photoanode assembly schemes, the ALD template approach should provide straightforward access to other high area semiconductor electrodes[5, 24] including some previously inaccessible via traditional nanoparticle networks.

Chapter 4. Electron Transport and Interception in ZnO Nanotube Arrays

4. Chapter Overview

Secondary evidence for exceptionally long (> 20 μm) charge collection in ZnO nanotube DSSCs was described in the previous chapter. As discussed in the Chapter 1, the realization of accelerated electron diffusion will dramatically increase the number of feasible redox shuttles and sensitizers used in DSSCs. This chapter describes my attempt to quantify electron diffusion in ZnO nanotubes and better understand the charge dynamics of these promising 1-D photoanodes.

In this chapter, dye-sensitized solar cells based on polycrystalline ZnO nanotube array photoanodes are shown to exhibit electron diffusion lengths in excess of 64 μm. Electrochemical impedance spectroscopy, open-circuit photovoltage decay measurements, and incident-photon-to-current efficiency spectra are used to quantify charge transport and lifetimes. An effective diffusion constant in excess of 7×10^{-3} $cm^2V^{-1}s^{-1}$ make these psudeo-1D photoanodes the fastest reported for an operating DSSC to date. The rapid electron collection further allows for the use of alternative redox shuttles without loss of charge collection efficiency.

4.1. Introduction

Since the breakthrough in dye-sensitized solar cell (DSSC) technology in the early 1990s, the most efficient versions of these devices have exhibited exceptional monochromatic incident photon-to-current efficiencies (IPCEs).[1, 2] Phenomenologically, this measure can be further divided into at least three separate processes according to:

$$IPCE = \eta_{LH} \cdot \eta_{CS} \cdot \eta_{CC} \qquad (1)$$

where η_{LH}, η_{CS}, and η_{CC} describe the efficiency with which light is harvested, the opposing charges are separated, and the charges are collected at their corresponding electrodes, respectively. That the IPCEs approach unity at the peak absorbance in the most efficient DSSCs implies that nearly every photon of this wavelength is harvested by the moderately high extinction dyes bound to the high surface area electrode. Furthermore, it must be the case that the excited state of the sensitizer injects an electron into the semiconductor network before the excited state decays to its ground state. Finally, the injected electron must pass through the nanoparticle network to be collected at the transparent electrode without recombining with the oxidized dye or being intercepted by adjacent oxidizing equivalents (I_3^-) in solution.

It has been duly noted that of particular improbability in this electrochemical system is the high η_{CC}, considering the millisecond timescale over which electrons may traverse the photoanode in such close proximity to oxidizing species.[3] For comparison, carriers traverse silicon photovoltaics in tens of microseconds[4] while charge collection in efficient organic photovoltaics occur on the tens of nanoseconds timescale.[5] Indeed, it is this relatively slow electron collection in DSSCs that is responsible for the very small number of feasible DSSC redox shuttles discovered to date. Due to a simple kinetic competition between electron collection and interception, IPCEs are dramatically reduced when electron interception is accelerated (lifetime shortened), an effect which has been modeled in detail.[6-8] It is not surprising then, that several novel photoanode architectures with the prospect of rapid charge collection have recently been explored.[3, 9-11] Psuedo 1-D nanostructures, particularly with single or polycrystalline domians, are especially interesting since electrons transported through the semiconductor are believed to be diffusion controlled.

Here we quantify the charge lifetime, τ_n, and charge extraction time, τ_d, for ZnO nanotube array photoanodes via electrochemical impedance spectroscopy. Rapid screening of several redox shuttle solutions by photovoltage decay under open-circuit conditions corroborates τ_d and illustrates the opportunity for efficient charge collection under accelerated interception conditions. Analysis of IPCEs under increasing $[I_3^-]$ (faster interception) and with a $Co^{2+/3+}$ species further support the hypothesis that electrons are successfully collected from the entire 64 μm photoanode thickness. Electron diffusion and interception time constants are derived from equivalent circuit analysis to reveal the fastest reported diffusion constant of any DSSC photoanode to date.

4.2. Experimental

4.2.1. Materials

Devices were constructed similarly to those previously reported.[10] Briefly, commercial anodic alumina oxide (AAO) membranes (Whatman 13, 0.02 um) were uniformly and conformally coated with polycrystalline ZnO via atomic layer deposition (ALD) at 150ºC. To simplify equivalent circuit modeling, an additional ~50 nm ZnO layer was grown exclusively on the small pore side of the disc, also by ALD. This ensures that the similarly and subsequently deposited transparent conducting oxide (TCO), namely Al:ZnO, is never in contact with the liquid electrolyte that will fill the pores. Prior to deposition of the TCO the photoanodes were fired in air at 450ºC for 30 minutes to increase crysallinity. A Surlyn hot melt spacer (25 um, Solaronix) was sandwiched between the photoanode and platinized fluorine doped tin oxide (FTO) electrode at 80ºC. The iodide-based redox shuttle solution is comprised of 0.5 M LiI, 0.5 M tert-butylpyridine, and 0.05 M I_2 in 3-methoxypropionitrile. For experiments with increasing

$[I_3^-]$, additional LiI and I_2 were added with the assumption that their reaction goes nearly to completion. A previously reported $Co^{2+/3+}$ redox shuttle[12] was also employed in a solution of 0.3 M $[Co^{II}(4,4'\text{-di-}tert\text{-butyl-}2,2'\text{-dipyridyl})_3]\{ClO_4\}_2$, 0.03 M nitrosonium tetrafluoroborate, 0.2 M lithium perchlorate, and 0.2 M tert-butylpyridine also in 3-methoxypropionitrile.

4.2.2. Instrumentation

Electrochemical impedance spectra were obtained on a Solartron 1260A frequency response analyzer coupled to a Solartron 1286 electrochemical interface. Cells were measured in two-electrode configuration in the dark over a frequency range of 60 mHz to 60 kHz. In order to reduce electromagnetic interference and stray light the devices were enclosed in an environmental chamber (Sun Electronics, EC10). Zview equivalent circuit modeling software was used to fit the data by utilizing built-in extended element (DX Type 11 - Bisquert #2) which allows for transmission line modeling as shown in Figure 4.1.

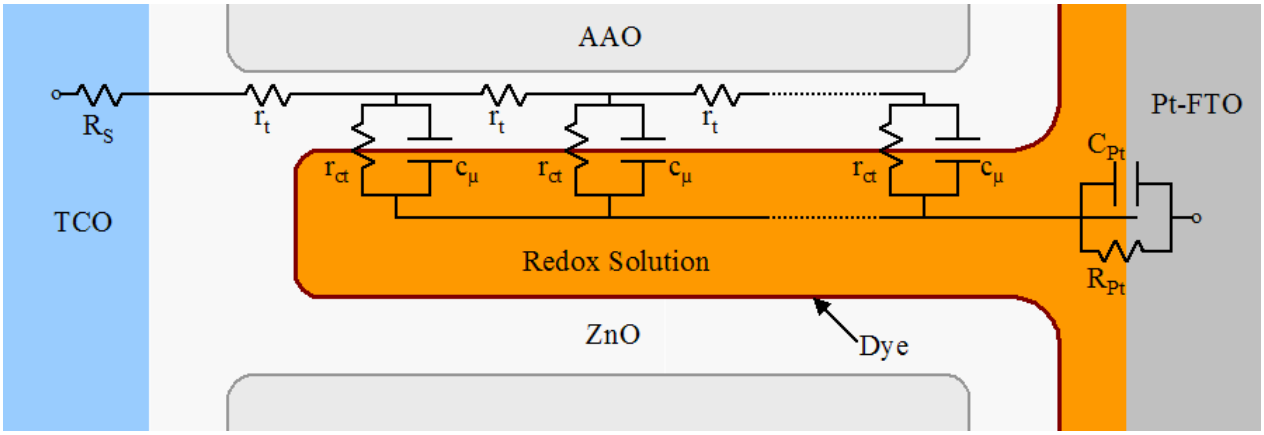

Figure 4.1. The equivalent circuit to which impedance spectra are fit overlays a highly idealized photoanode schematic. Equivalent circuit elements overlay the geometrically appropriate interface.

4.3. Results and Discussion

4.3.1. Electrochemical Impedance Spectroscopy

Electrochemical impedance spectroscopy (EIS) is an effective technique for elucidating the competition between electron interception (typically by I_3^-) and diffusion to the TCO.[13-15] As a useful point of reference, the most efficient (10 to 11% power efficient) DSSCs to date have been characterized using EIS.[3] Similar to this and other literature reports, impedance spectra were fit to a geometrically appropriate equivalent circuit[16], Figure 1. The most detailed literature models may be simplified for the system described here due to the absence of exposed TCO and the restriction to low current conditions in which electrolyte diffusion impedance (Z_d) is vanishingly small. A representative Nyquist plot, Figure 4.2, shows characteristic features of the ZnO nanotube device impedance from left (high frequency): small semicircle [$R_{Pt}C_{Pt}$], ~45º straight line [R_t coupled to C_μ], and large semicircle [$R_{ct}C_\mu$].

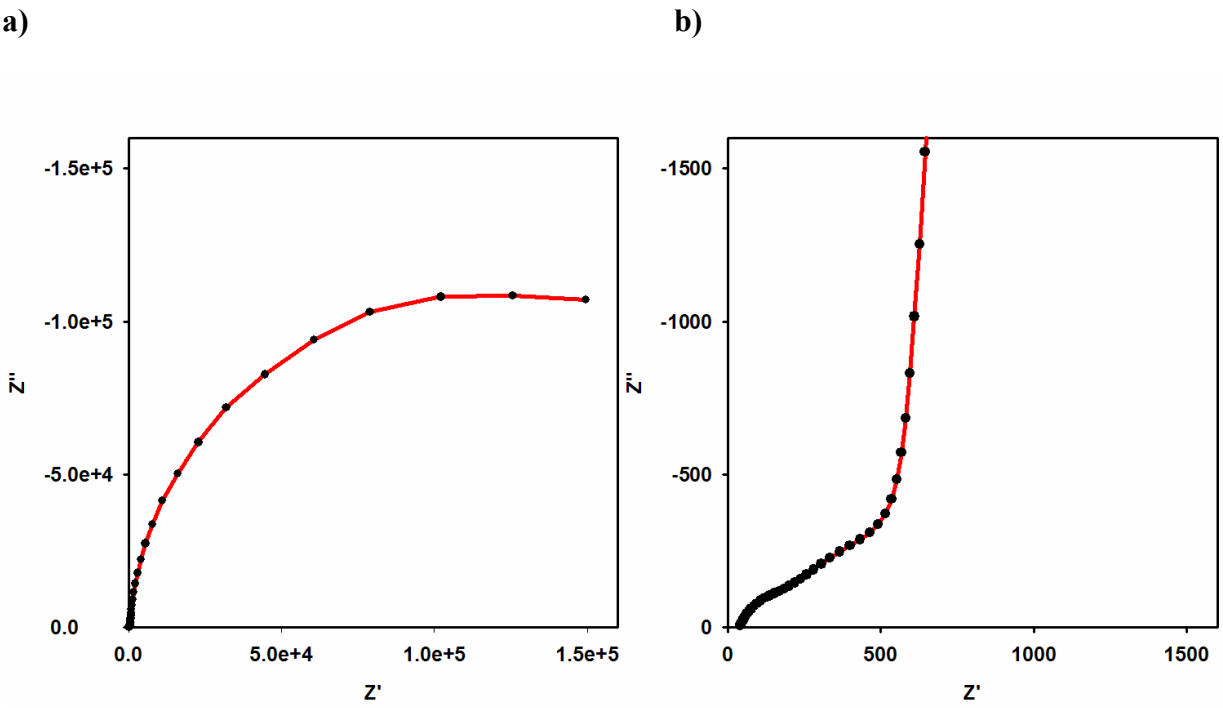

Figure 4.2. a) Impedance spectra of representative EIS data at 300 mV forward bias in the dark. b) 100x magnification of the same spectra shows the high frequency response.

Assuming an interpretation of capacitance and diffusive transport similar to nanoparticle photanodes, the relevant time constants for electron collection, $\tau_d = R_t C_\mu$, and lifetime, $\tau_n = R_{ct} C_\mu$, may be extracted from the fitted data as well as the effective rate of electron diffusion, $D_n = (L^2 \tau_d^{-1})$.

Good fits to the equivalent circuit were obtained for ZnO nanotube arrays with pore wall thickness of 16 nm. In arrays with thinner ZnO pore walls an unexpected feature grows in, especially at small applied potentials, near 100 Hz that prohibits quantitative determination of τ_d. Even for the 16 nm pore wall arrays, the relative size and variability of impedance at the platinized FTO electrode adds uncertainty to the measurement. To be cautious, two different fits are shown with two reasonable extremes of $R_{Pt}C_{Pt}$, Figure 4.3.

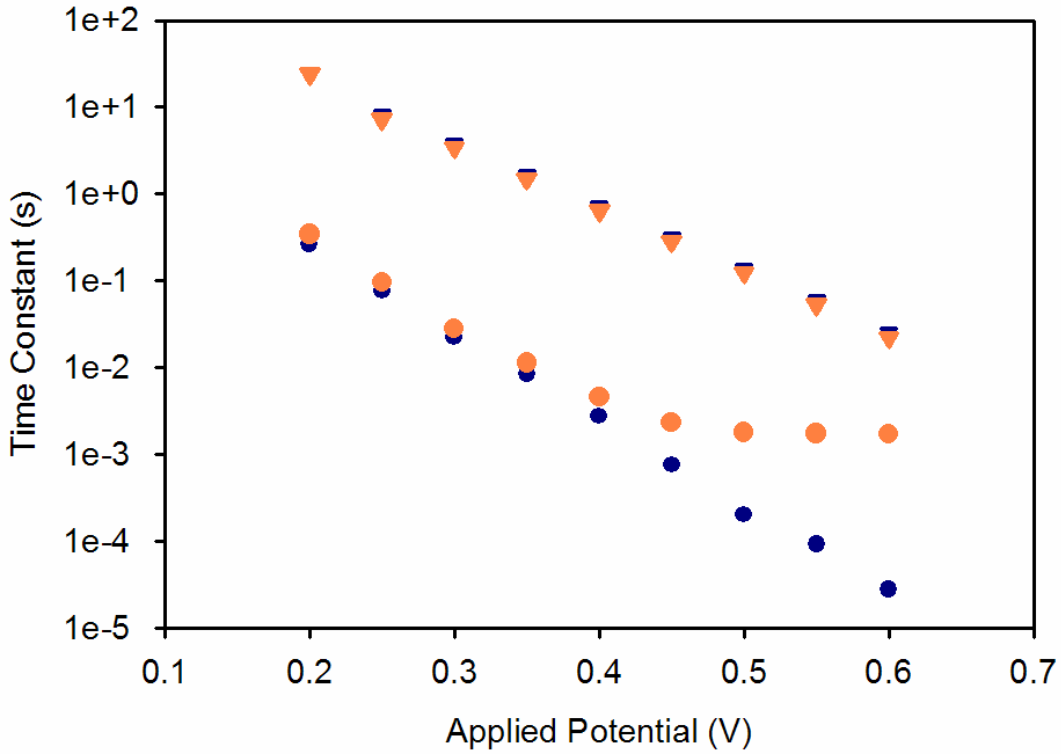

Figure 4.3. Charge lifetime (triangles) and charge collection time (circles) derived from two fits to the equivalent circuit. Blue symbols assume largest reasonable dark electrode impedance while orange symbols denote fit with smallest reasonable dark electrode impedance.

While the linear and roughly parallel trend in τ_n and τ_d with increasing applied potential are typical of most DSSC, several features are noteworthy. The first important point is that charge extraction is more than an order of magnitude faster than the lifetime ($\tau_d < \tau_n$) at all measured potentials, independent of the fit. This implies that the η_{CC} of the exceptionally thick photoanode is nearly unity. Furthermore, the values of τ_d reported here are more than an order of magnitude shorter than those measured at the same applied potentials in the most efficient nanoparticle TiO_2 DSSCs. Since diffusion goes as the square of distance, the advantage in D_n for the relatively long nanotube photoanode is even more pronounced. The two maximum values measured for D_n (7×10^{-3} and $0.4\ cm^2s^{-1}$) exceed any DSSC photoanode previously reported by 17 and 1000 times. The feasibility of these values may be weighed against the theoretically predicted diffusion coefficient for polycrystalline ZnO. According to Einstein's relation

$$D = \frac{\mu k_B T}{q} \qquad (2)$$

where μ, k_B, T, and q represent mobility ($cm^2V^{-1}s^{-1}$), Boltzman's constant (JK^{-1}) and temperature (K) and the unit charge (C). It should be note here that no DSSC photoanode to date has approached this theoretical value but that there is no well-understood reason preventing it. The range of reported μ for polycrystalline ZnO films grown by ALD before firing is ~3 to 27 $cm^2V^{-1}s^{-1}$, roughly and order of magnitude lower than the accepted single crystal value of 180 $cm^2V^{-1}s^{-1}$.[17, 18] Therefore, at room temperature the anticipated range of electron diffusion through an (unfired) polycrystalline film is 0.1 to 0.7 cm^2s^{-1}, while D is not expected to exceed 5 cm^2s^{-1} in a ZnO single crystal. Given this range, even the fit to the fastest value of D_n (0.4 cm^2s^{-1}) is not unreasonable.

4.3.2. IPCE Analysis

Since electron extraction is significantly faster in ZnO nanotube array photoanodes, we expect the device to be more tolerant to "faster" redox shuttles. That is, we expect the same J_{SC} even upon intentional acceleration of the rate of electron interception (decresing r_{ct}), up to the point at which at which $\tau_n \approx \tau_d$. This hypothesis has been tested on a 8 nm ZnO pore wall nanotube array-based DSSC by systematically increasing the $[I_3^-]$ as well as employing a previously studied Co complex to shuttle the hole. Here, open-circuit photovoltage decay measurements were used in place of EIS in order to more quickly screen the range of τ_n.[19] As expected, τ_n becomes progressively shorter with greater $[I_3^-]$ and dramatically shorter in the case of the Co shuttle, Figure 4.4.

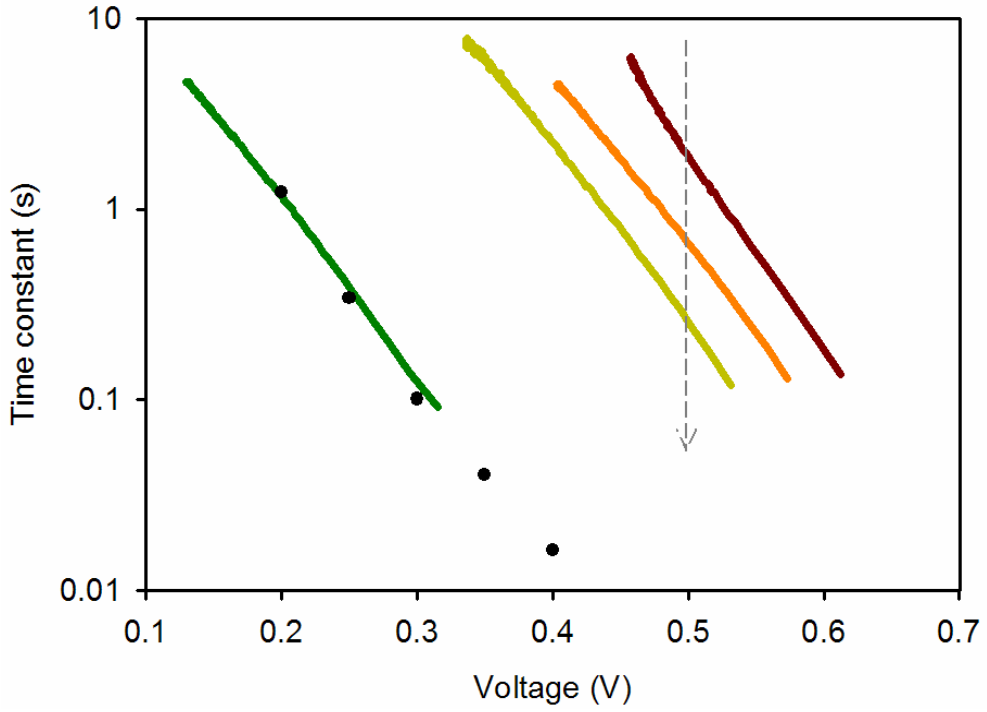

Figure 4.4. Electron lifetime in completed DSSC (from right to left) with $[I_3^-]$ = 0.05 M (dark red), 0.1 M (orange), 0.2 M (yellow) and $[Co^{3+}]$ = 0.03 (green). For reference, the black circles show a portion of the slowest electron extraction data from Figure 3. The dashed gray arrow shows the decrease in electron lifetime (at the same voltage) with increasing $[I_3^-]$.

While the τ_n and τ_d shown in Figure 4.4 are derived from slight different devices, 8 and 16 nm pore walls are used (respectively), we expect charge extraction to be competitive in each case tested. More concretely, the effective diffusion length, L_n, over which charges may be extracted

$$L_n = \sqrt{D_n \cdot \tau_n} = L\sqrt{\frac{\tau_n}{\tau_d}} \qquad (3)$$

will approach L, the photoanode thickness, when $\tau_d \approx \tau_n$. Thus, even for a redox shuttle that results in 100× shorter electron lifetime, we still expect charge collection over the entirety of the 64 μm photoanode thickness.

To test this hypothesis, the L_n of a DSSC may be probed (to a first approximation) by analysis of monochromatic IPCEs. Since monochromatic IPCEs are a function of at least 3 distinct microscopic processes (Equation 1) it is necessary to deconvolute in order to understand the competition between electron extraction and interception. While the η_{LH} of these photoanodes is not trivial to quantify, owing to the scattering nature of the membranes, it may be estimated by an integrating sphere or by subtracting the scattering from a membrane prior to dye loading. Regardless, relative changes in the other to two variables (η_{CS} and η_{CC}) may be probed by simply holding η_{LH} (and the incident light) constant. That is, if a nominally identical photoanode is employed, any change in the IPCE must be due to changes in η_{CS} and/or η_{CC}. The same can be said for η_{CS}, which has not been quantified for these DSSC but is expected to remain constant for identically prepared photoanodes in contact with similar redox solutions. Thus a relative measure of the remaining variable of interest, η_{CC}, is reported by the magnitude of the IPCE. That charge extraction (and therefore L_n) is approximately equal for each electrolyte probed is illustrated in Figure 4.5.

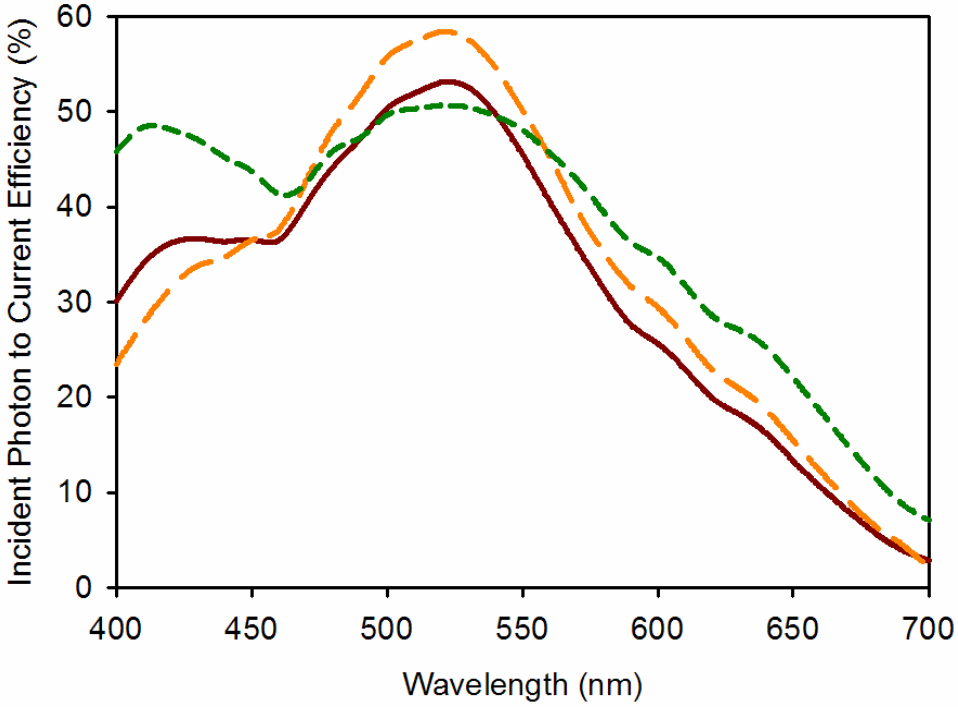

Figure 4.5. Incident photon to current efficiencies for devices with of $[I_3^-] = 0.05$ M (dark red , solid line), $[I_3^-] = 0.1$ M (orange, long dashed line) and $[Co^{3+}] = 0.03$ M (green, short dashed line).

That the shape of the spectral response is similar in each case further implies that L_n is the same. For example, if electrons only within the first 32 μm of the 64 μm thick photoanode are collected, only dye molecules absorbed to the front half of the tubes (closest the TCO) will contribute to the photocurrent. Therefore, owing to the log relationship between absorbance and η_{LH}, the absorbance peak would sharpen with decreasing L_n (decreasing τ_n). Clearly the primary light harvesting peak is not sharpening with decreasing τ_n for these devices. When normalized at peak IPCE (data not shown), the two DSSC with I^- based electrolyte show almost identical line shapes from 470 to 700 nm. At wavelengths less than 470 nm the attenuated response when the $[I_3^-]$ is doubled is due to greater light attenuation by the redox concentrated shuttle. The small discrepancy in photoresponse of the Co-based device is most likely also due to a difference in incident light attenuation by the solution. Combined, the similar magnitude and spectral shape of the IPCE response suggest electrons are collected throughout the length of the photoanode even under accelerated interception conditions.

4.4. Conclusions

In summary, the effective diffusion coefficient of electrons through ZnO nanotube array photoanodes are measured to be from 1 to 3 orders of magnitude faster than any DSSC photoanode reported to date. Photovoltage decay measurements and analysis of IPCEs with increasing $[I_3^-]$ in addition to an Co-based redox shuttle further support the values of τ_n and τ_d as measured by electrochemical impedance spectroscopy. Despite the relatively long photoanode thickness, electrons are efficiently and rapidly extracted throughout its 64 μm length.

Chapter 5. Atomic Layer Deposition of Transparent Conducting Oxides

5. Chapter Overview

Two new ZnO photoanode geometries, nanorods and nanotubes, were fabricated and their charge dynamics detailed in the previous three chapters. Both of these systems are in close analogy to the most efficient TiO_2 nanoparticle devices in that injected electrons diffuse (at different rates) through multiple microns of semiconductor to be collected at the TCO. In this chapter the path toward a decidedly different architecture is paved. We hypothesized that by extending the TCO into the semiconductor framework the electron diffusion distance may be reduced from microns to nanometers, Figure 5.1. Since diffusion time scales as the square of distance we expect this design to reduce electron transport times by several orders of magnitude, even compared to the more rapid extraction of electrons through ZnO nanotubes, as described in Chapter 4. As an adequate deposition technique and precursor did not exist to fabricate the proposed structure, a new atomic layer deposition precursor to In_2O_3 (and eventually ITO) was identified and characterized. This chapter describes a new method for depositing In_2O_3 thin films by atomic layer deposition (ALD) using alternating exposures to cyclopentadienyl indium and ozone. A significant advantage of this synthesis route over previous techniques is the ability to conformally coat porous materials such as anodic aluminum oxide membranes. The deposited films are crystalline, cubic phase In_2O_3 and are highly transparent and conducting. In situ quadrupole mass spectrometry and quartz crystal microbalance measurements elucidate the details of the In_2O_3 growth mechanism. Furthermore, a new atomic layer deposition (ALD) method for preparing indium tin oxide (ITO) thin films using nonhalogenated precursors is presented. The indium oxide (In_2O_3) was deposited using alternating exposures to cyclopentadienyl indium (InCp) and ozone, and the tin oxide (SnO_2) used alternating exposures to tetrakis(dimethylamino) tin (TDMASn) and hydrogen peroxide. ITO films were characterized

using four-point probe and Hall probe measurements, spectrophotometry, ellipsometry, scanning electron microscopy, atomic force microscopy, X-ray fluorescence, and X-ray diffraction.

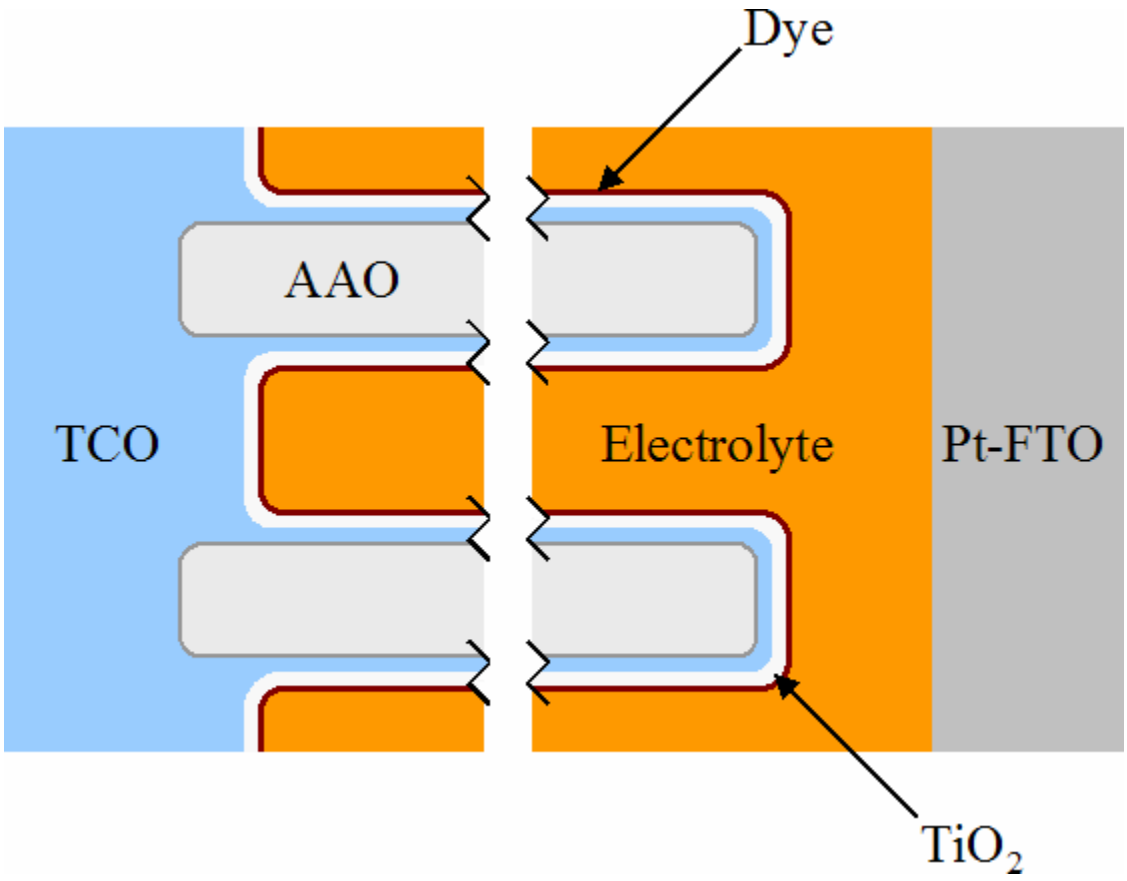

Figure 5.1. Proposed design of interdigitated TCO DSSC. For clarity an aspect ratio of ~3 is shown. Efficient DSSC operation using conventional sensitizers require an aspect ratio in excess of 1000.

5.1. Introduction

In_2O_3 thin films have applications as transparent conducting oxides (TCOs)[1], gas sensors,[2-4] and catalysts[5-9]. For optimum performance, all of these applications require precise control over film thickness and composition, and some require the ability to coat high aspect ratio or porous materials.[2, 5-7] In_2O_3 thin films can be deposited using a variety of methods including sputtering[10, 11], chemical vapor deposition[12-15], and atomic layer deposition (ALD)[16-20]. Of these techniques, ALD shows significant promise as this method affords excellent control over both the thickness and composition of the deposited film.[21] Most importantly, ALD offers unmatched conformality that enables the coating of porous materials with aspect ratios in excess of 1000.[22-24]

Previously, In_2O_3 ALD has been accomplished using $InCl_3$ with either H_2O[16] or H_2O_2[19] as the oxygen source. Although useful for coating planar surfaces, this method suffers from several limitations. First, the $InCl_3$ chemistry requires high growth temperatures of ~300-500°C and yields a low growth rate of only 0.25-0.40 Å/cycle. In addition, the $InCl_3$ has a very low vapor pressure and must be heated to 285°C just to saturate a planar surface. Furthermore, the corrosive HCl byproduct can damage the deposition equipment. But the greatest limitation of the $InCl_3/H_2O$ method, especially for coating nanoporous materials, is that $InCl_3$ can etch the deposited In_2O_3.[16] Nanoporous materials require very long precursor exposures that are likely to completely remove the In_2O_3 from the outer portions of the nanoporous substrate.

The primary goal of this study was to develop an improved ALD process for In_2O_3 that allows the coating of nanoporous materials. A number of alternate precursors have been investigated previously including beta-diketonates[20] ($In(hfac)_3$ (hfac=hexafluoropentadionate),

$In(thd)_3$ (thd=2,2,6,6-tetramethyl-3,5-heptanedioneate) and $In(acac)_3$ (acac=2,4-pentanedionate)) and trimethyl indium[25], ($In(CH_3)_3$). Unfortunately, these efforts were unsuccessful. No growth was observed using beta-diketonates with water or hydrogen peroxide, while trimethyl indium did not yield self-limiting growth. In this paper we describe a new method for In_2O_3 ALD using cyclopendadienyl indium (I) (InCp) and ozone. A related compound, pentamethylcyclopentadienyl indium(I), has been used previously for InP chemical vapor deposition.[26] We utilize *in situ* quadrupole mass spectrometer (QMS) and quartz crystal microbalance (QCM) measurements to understand the growth mechanism. Next, we deposit In_2O_3 films on Si(100) and glass substrates and analyze the films using spectroscopic ellipsometry, x-ray powder diffraction, four-point probe resistivity, atomic force microscopy, UV-visible absorption spectroscopy, and scanning electron microscopy. These analyses reveal that cubic phase, nanocrystalline In_2O_3 is deposited at a growth rate of 2.0 Å/cycle. Finally, we apply this technique to conformally coat nanoporous anodic aluminum oxide (AAO) membranes.

5.2. Experimental

5.2.1. Growth Condition

The ALD films were deposited in a custom viscous flow reactor similar in design to those that have been described previously.[27] Briefly, a stainless steel flow tube with an inside diameter of 5 cm houses substrates for film growth as well as the quartz crystal microbalance (QCM). Ultrahigh purity nitrogen carrier gas continuously passes through the flow tube at a mass flow rate of 360 sccm and a pressure of 1 Torr. A constant reactor temperature is maintained by four separate temperature controllers connected to resistive heating elements attached to the outside

of the reactor. The four heating zones create a uniform temperature profile along the length of the flow tube to reduce the influence of temperature transients on the QCM measurements.[28]

In_2O_3 ALD was performed using alternating exposures to cyclopendadienyl indium (I) (InCp, Strem, electronic grade 99.999+% In) and ozone. The InCp is held in a stainless steel bubbler maintained at 40 °C, and the tubing connecting the bubbler to the ALD reactor is maintained at 200 °C to prevent the deposition of InCp on the reactor walls. Ultrahigh purity nitrogen (99.999%) at a mass flow rate of 60 sccm was sent through the bubbler during the InCp exposures, and was diverted to bypass the bubbler following the InCp exposures. The ozone was produced using a commercial ozone generator (Ozone Engineering L11) using a feed of ultrahigh purity oxygen at a flow rate of 400 sccm to produce ~10% ozone in oxygen. We also attempted In_2O_3 ALD using beta-diketonate precursors with ozone. The beta-diketonate precursors used were: $In(hfac)_3$, (Gelest), and $In(acac)_3$, (Gelest). Additional oxygen sources evaluated for In_2O_3 ALD included deionized water (18 MΩ cm), hydrogen peroxide (30% solution in water, Aldrich), ultrahigh purity oxygen, and nitrous oxide (Aldrich, 99%)).

The ALD timing sequences can be expressed as t1-t2-t3-t4 where t1 is the exposure time for the first precursor, t2 is the purge time following the first exposure, t3 is the exposure time for the second precursor, t4 is the purge time following the exposure to the second precursor and all units are given in seconds (s). The timing sequence for In_2O_3 ALD was typically 2-4-2-2 s.

In_2O_3 ALD films were deposited on 1 cm x 2 cm Si(100) and glass substrates. Prior to loading, the substrates were ultrasonically cleaned in acetone and then isopropanol and blown dry using nitrogen. After loading, the substrates were allowed to outgas in the ALD reactor for 10 minutes at the deposition temperature (typically 250°C) in 1 Torr of flowing ultrahigh purity

nitrogen. Next, the substrates were cleaned *in situ* using a 60 s exposure to 10 % ozone in oxygen at a pressure of 2 Torr and a mass flow rate of 400 sccm.

5.2.2. Instrumentation

A QCM was installed in the ALD reactor in place of substrates enabling *in situ* measurements during the In_2O_3 growth. These measurements utilized a Maxtek BSH-150 bakeable sensor and AT-cut quartz sensor crystals with a polished front surface obtained from the Colorado Crystal Corporation, part # CCAT1BK-1007-000. The QCM measurements were made using a Maxtek TM400 film thickness monitor interfaced to a personal computer. In addition, the ALD reactor was equipped with a QMS (Stanford Research Systems RGA300) located downstream of the QCM in a differentially-pumped chamber separated from the reactor tube by a 35 micron orifice and evacuated using a 50 l/s turbomolecular pump.

Scanning electron microscopy (SEM) images were acquired using an Hitachi S4700 SEM with a field emission gun electron beam source, secondary electron and backscattered electron detectors, and an energy dispersive analysis of X-rays (EDAX) detector for elemental analysis. Atomic force microscopy (AFM) measurements were performed on a Digital Instruments Dimension 3000 with a NanoScope IIIa controller operated in tapping mode. X-ray diffraction (XRD) measurements were taken on a Rigaku Miniflex Plus diffractometer. Ellipsometric measurements of the In_2O_3 films deposited on Si(100) surfaces were performed using a J. A. Woolam Co. M2000 variable angle spectroscopic ellipsometer (VASE) using a table of refractive indices for In_2O_3 supplied with the instrument. Optical absorption spectra were acquired from ALD In_2O_3 films deposited on glass using the M2000 operated in transmission mode and were fit to a model using the same In_2O_3 optical constants. Anodic aluminum oxide

membranes (AAO, Whatman Anodisc 13) with pore diameters of 200 nm and a membrane thickness of 70 microns were also coated by In_2O_3. Prior to SEM analysis, cleaved cross sections of the membranes were embedded in conducting epoxy and polished with progressively finer diamond polishing compound ending with 0.25 micron.

5.3. Results and Discussion

5.3.1. Initial Studies using Beta-Diketonates

A previous study measured virtually no In_2O_3 growth using indium beta-diketonates ($In(acac)_3$, $In(hfac)_3$, and $In(thd)_3$) with either water or hydrogen peroxide as the oxygen source.[20] The lack of growth was attributed to the very low reactivity of these beta-diketonate precursors to the In_2O_3 surface; however, ALD with ozone was not tested in this previous study. Ozone is often successful in ALD with beta-diketonates [29-31], so we initially tried using $In(acac)_3$ and $In(hfac)_3$ with O_3. *In situ* QCM experiments performed at 150-300°C on a previously deposited ALD Al_2O_3 surface consistently yielded 0.3-1.0 Å In_2O_3 during the first ALD cycle, but little or no growth afterwards. This suggests that the reactivity of the indium beta-diketonates is relatively high on Al_2O_3 but too low on the In_2O_3 to support growth even using O_3. We attempted to deposit In_2O_3 films on Si(100) and glass substrates using $In(hfac)_3/O_3$ at higher temperature of 350-500°C. Using an $In(hfac)_3$ bubbler temperature of 160°C, the growth rate increased sharply with temperature from 0.03 Å/cycle at 350°C to 0.51 Å /cycle at 500°C, but the results were erratic. These difficulties may result from thermal decomposition of the $In(hfac)_3$ inside the reactor tube or in the bubbler or possibly sintering of the solid indium compound.

After our lack of success with $In(acac)_3$ and $In(hfac)_3$, we shifted our attention to InCp. Our initial measurements were encouraging as we discovered that we could deposit In_2O_3 films using $InCp/O_3$. Preliminary experiments were performed to determine the appropriate InCp bubbler temperature. In_2O_3 films were deposited using the timing sequence 2-2-1-2 on Si(100) substrates at 250°C for 100 cycles while varying the InCp bubbler temperature between 30-60°C. These measurements demonstrated that the InCp growth rate was nearly constant using bubbler temperatures above 40°C. Using the baratron pressure gauge, we measured a vapor pressure for InCp of 0.1 Torr at 40°C. We tried using InCp with other oxygen sources, but the growth rates were substantially lower as shown in Table 5.1. It is curious that the water did not allow growth considering that H_2O is a typical oxygen source in metal oxide film ALD utilizing cyclopentadienyl precursors.[30, 32, 33] It may be that the more powerful oxidizing agent, O_3, is necessary to oxidize the In from +1 to +3.

Oxygen Source	*In_2O_3 Growth Rate Thickness (Å/cycle)*
ozone	1.3
oxygen	0.16
water	0.068
hydrogen peroxide	0.039
nitrous oxide	0.065

Table 5.1. Growth rate for In_2O_3 films deposited on Si(100) substrates using 100 cycles of InCp and different oxygen sources at 250-275°C.

5.3.2. In situ Measurements during In_2O_3 ALD

In situ QCM and QMS measurements were used to investigate the mechanism for In_2O_3 ALD using InCp and O_3. These measurements were performed at 250°C using the timing sequence 2-5-2-15. The In_2O_3 ALD process can be described by a generalized reaction scheme:

$$* + InCp \rightarrow InCp_x* + (1\text{-}x) \text{ products} \quad (1)$$

$$InCp_x* + \text{Oxidant} \rightarrow InO_{1.5}* + (x) \text{ products} \quad (2)$$

In these reactions, the surface species are designated with an asterisk and x is the fraction of Cp ligands remaining on the surface following each InCp exposure. The gas-phase products, the initial reactive sites, and the oxidant are all left unspecified but will be determined from the *in situ* measurements.

QMS measurements were performed to determine the gas phase products of the InCp and ozone half reactions. Representative QMS data recorded during the InCp and O_3 half-reactions are shown in Figures 5.2a and 5.2b, respectively. As shown in Figure 5.2a, a peak at m=66 appears during the InCp half reaction, but not during the O_3 half reaction. When the InCp exposure follows an O_3 exposure, the m=66 peak has a sharp spike at the leading edge followed by a smaller plateau that persists as long as the InCp dosing valve is held open as illustrated by the first two ALD cycles in the figure. However, if no O_3 exposure precedes the InCp exposure, the sharp spike in the m=66 peak is absent as shown by the final two ALD cycles in Fig. 5.2a. From these observations we conclude that the sharp feature represents a gas-phase product of reaction 1, while the smaller plateau is simply decomposition of the InCp precursor in the QMS.

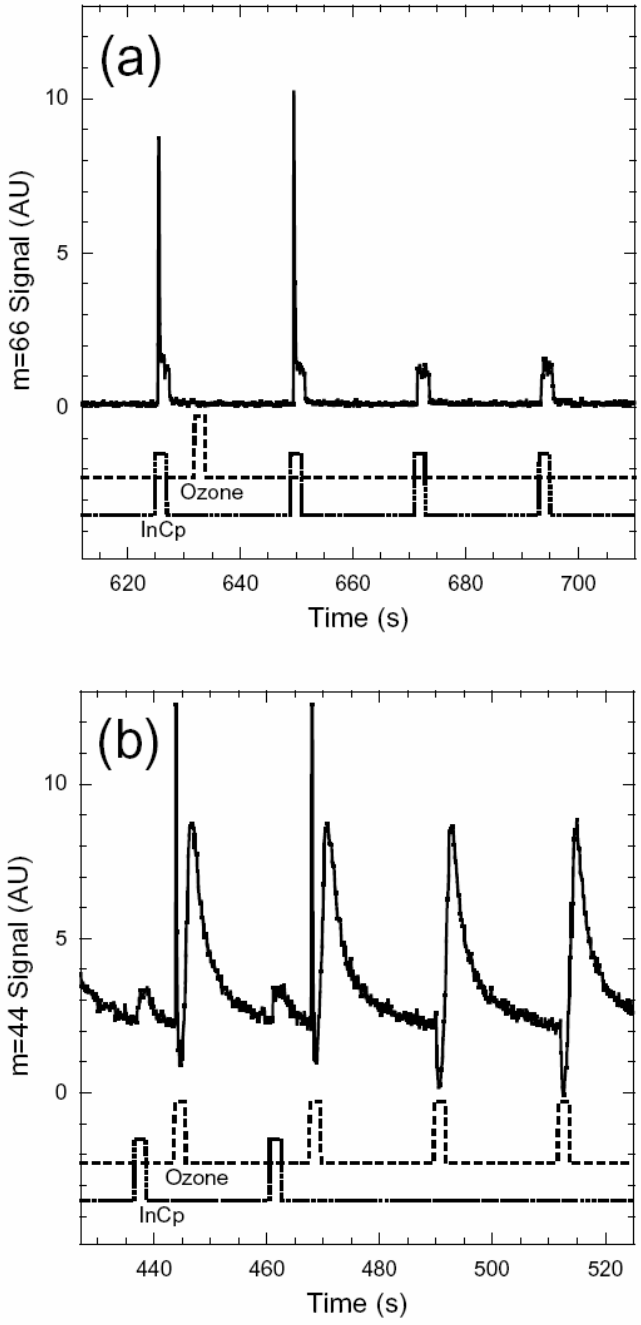

Figure 5.2. (a) QMS signal for m=66 (cyclopentadiene, solid line) versus time during alternating exposures to InCp (dotted line) and O_3 (dashed line) at 250°C using the timing sequence: 2-5-2-15. (b) QMS signal for m=44 (CO_2) recorded using the same conditions as (a).

Similarly, we see a sharp spike in the m=44 signal coincident with the O_3 exposures that are preceded by InCp exposures (Figure 5.2b); however, this spike is not seen when the InCp exposures are absent. Consequently, we conclude that m=44 is a gas-phase product of reaction 2. The small peak in the m=44 data coincident with the InCp exposures is present whether or not the InCp exposure is preceded by an O_3 exposure, and therefore this is a crack of InCp rather than a reaction product. The large, slow transient feature in the m=44 signal that appears during the purge cycle of each O_3 exposure results from a CO_2 impurity in the ultrahigh purity oxygen which is pumped slowly by our system.

By collecting QMS data over the mass range 12-115 AMU, we discovered that m=44 (CO_2) is the only product of the O_3 reaction, while the InCp reaction yields the following products (and relative abundances): m=66 (100), 65 (67), 39 (53), 40 (33). This mass pattern matches closely the fragmentation pattern for cyclopentadiene (C_5H_6) [34]. It is surprising that we do not observe water during the O_3 half reaction. One explanation is that the hydrogen from the Cp ligands in reaction 2 remains on the surface as hydroxyl (OH) groups that subsequently react with InCp to form HCp (cyclopentadiene, m=66). This would explain why no m=18 is observed in reaction 2, while the main product from reaction 1 is m=66 rather than m=65.

The ratio of gas phase products measured during the InCp and O_3 half reactions can be used to calculate x in Eqns. 1-2. By integrating the product mass peaks observed during the InCp exposures and correcting for variations in electron multiplier gain, quadrupole transmission, and ionization efficiency, we calculate that the amount of Cp released during equation 1 is (in arbitrary units): (1-x)=15. Similarly, after correcting for the relative effusion rate of CO_2 versus cyclopentadiene, the amount of CO_2 released during equation 2 is: (5x)=13.8

where the quantity 5x accounts for the fact that 5 CO_2 molecules are released from each Cp ligand. Combining these expressions, (1-x)/(5x)=1.09 so that x=0.15.

Figure 5.3a shows the QCM data recorded simultaneously with the QMS measurements demonstrating that alternating $InCp/O_3$ exposures results in a linear mass increase versus time. The slope of the data in Figure 5.3a yields a net mass change of 55 ng/cm^2/cycle. Assuming a bulk density for In_2O_3 of 7.19 g/cm^2, this corresponds to a growth rate of 0.76 Å/cycle. As described in the next section, this growth rate is lower than the 1.3-2.0 Å/cycle measured on Si(100) substrates. This difference arises because the QCM is located ~33 cm downstream of the substrates where the O_3 concentration is lower.

Figure 5.3b shows an expanded view of the QCM data for two ALD cycles. There is an abrupt mass increase during each InCp exposure and a transient mass decrease coincident with each O_3 exposure followed by a slow increase such that the net mass change produced by the O_3 exposures is almost zero. We attribute the apparent mass decrease during the O_3 exposures to a transient heating of the QCM produced by the thermal decomposition of O_3 or the oxidation of the Cp ligands.[28] The mass changes produced by the individual half reactions can predict the fraction of Cp ligands remaining on the surface after the InCp exposures. Using the relationship $R=\Delta m/\Delta m_2$ where Δm is the mass change from one complete cycle and Δm_2 is the mass change during reaction 1, we calculate from equations 1-2 and the atomic masses that $\Delta m=(InO_{1.5})=139$ and Δm_2= (In)+x(Cp)=115+65x so that R=139/(115+65x). From Figure 5.2a, R=1.0 so that x=0.37 which implies that, on average, 37% of the Cp ligands remain on the surface after reaction 1. This value is somewhat higher than the value x=0.15 calculated from the QMS data. The difference may arise from inaccuracies caused by the temperature-induced transient feature during the O_3 exposures. Nevertheless, the primary conclusion from the QCM data is the same

as from the QMS data: a majority of the Cp ligands are lost during the InCp exposures and the small fraction remaining is subsequently removed during the following O_3 exposure.

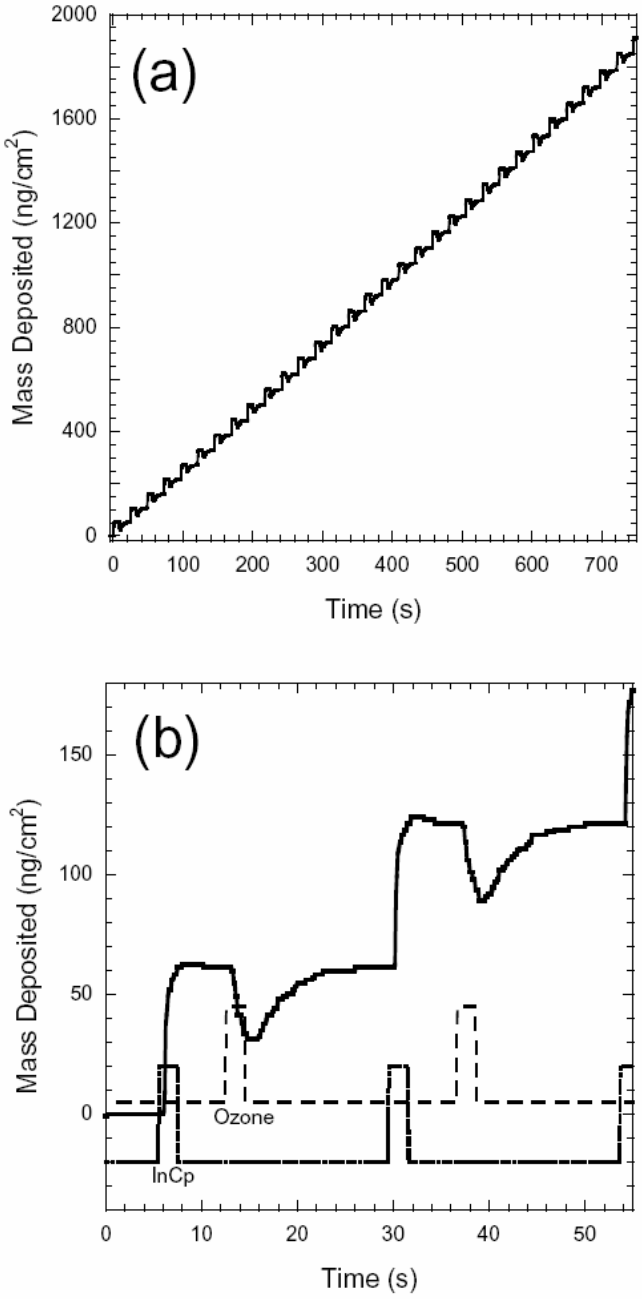

Figure 5.3. (a) QCM signal versus time during alternating exposures to InCp and O_3 at 250°C using the timing sequence: 2-5-2-15. (b) Expanded view showing correlation between QCM signal (solid line) and exposures to InCp (dotted line) and O_3 (dashed line).

One additional finding from the *in situ* measurements is that the reactive oxygen species during the In_2O_3 ALD is most probably oxygen radicals formed by the thermal decomposition of ozone ($O_3 \rightarrow O_2 + O$). The In_2O_3 growth rate drops off abruptly at 200°C to nearly zero (Figure 5.8) suggesting that we must exceed a threshold temperature for ozone decomposition to enable In_2O_3 growth. This interpretation is supported by the observation that the m=48 QMS signal from ozone is ~10x larger at temperatures below 200°C. Furthermore, In_2O_3 appears to catalyze O_3 decomposition more efficiently than Al_2O_3. Figure 5.4 demonstrates that when we first execute InCp/O_3 cycles following Al_2O_3 growth, the m=48 signal is initially high, but decreases nearly to zero following 40-50 In_2O_3 cycles. Moreover, the thicknesses of the In_2O_3 films deposited immediately following Al_2O_3 growth are thinner than expected, and in-situ QCM measurements reveal that the In_2O_3 growth is initially inhibited following Al_2O_3 growth. To compensate for this effect, we always deposited an In_2O_3 buffer layer on the inside of the reactor using ~100 InCp/O_3 cycles following depositing of a different material or after attempting In_2O_3 growth below 200°C. Taken together, these results suggest that the ozone decomposes to form a more active oxidizing species, and this species is most likely oxygen radicals.

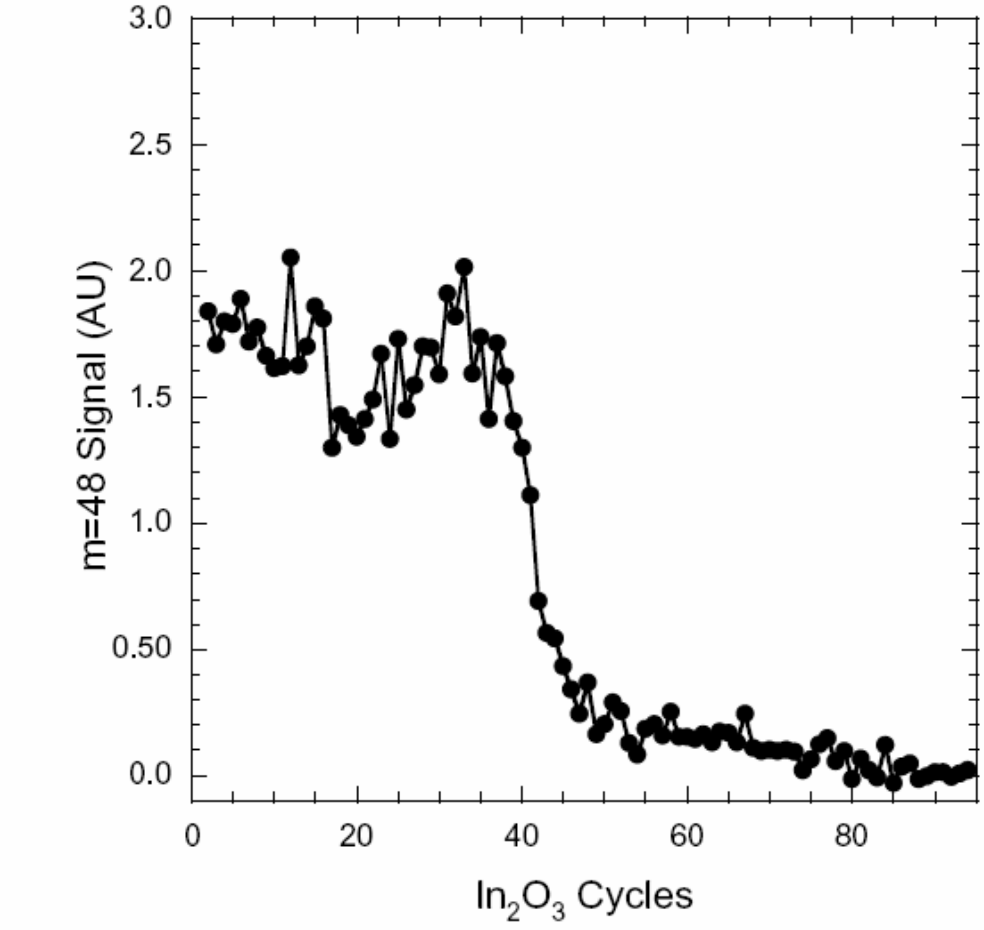

Figure 5.4. QMS signal for m=48 (ozone) versus number of $InCp/O_3$ cycles using the timing sequence: 2-5-2-15 at 250°C after previously coating the ALD reactor with Al_2O_3.

To summarize the in-situ measurements, we can rewrite Eqns. 1,2 with the unknown surface species, gaseous products, and oxidant filled in:

$$5\ OH^* + O^* + 6\ InCp \rightarrow 5\ O\text{-}In^* + O\text{-}In(Cp)^* + 5\ C_5H_6 \quad (3)$$

$$5\ O\text{-}In^* + O\text{-}In(Cp)^* + 17.5\ O \rightarrow 5\ O\text{-}In(O)_{0.5}\text{-}OH^* + O\text{-}In(O)_{1.5} + 5CO_2 \quad (4)$$

In reaction 3, the initial reactive sites are 5 OH groups and one surface oxygen species. Six InCp molecules react with the surface liberating 5 cyclopentadiene molecules leaving 1 Cp ligand on the surface. In reaction 4, 17.5 oxygen radicals react the surface and release the carbon from the remaining Cp ligand as 5 CO_2, but the 5 hydrogen atoms remain to reform 5 new hydroxyl groups. Consequently, reaction 4 regenerates the initial surface and forms In_2O_3 with the proper stoichiometry, In:O=1:1.5. Equations 3-4 yield x=1/6=0.17 which is in the range of x=0.15-0.37 determined from the *in situ* measurements. Although somewhat speculative, this mechanism has the appeal that the single remaining Cp ligand will exactly balance the 5 OH groups so that no hydrogen-containing products are released during the O_3 reaction. Although the In oxidation state is not explicit in Eqns. 3-4, the conversion from In(+1) to In(+3) probably occurs mostly during the oxygen radical step. *In situ* measurements using infrared absorption spectroscopy[35] could verify the existence of OH groups following the O_3 exposures. If oxygen radicals are indeed the necessary reactive species in this process, then substituting an oxygen plasma[36] in place of the O_3 may allow In_2O_3 growth below 200°C.

5.3.3. Growth of In_2O_3 Films

Following the *in situ* measurements, we proceeded with In_2O_3 deposition on Si(100) and glass substrates to study the In_2O_3 growth. Figure 5.5a shows the results of uptake measurements made while varying the exposure time to InCp using the timing sequence x-2-2-2. This figure demonstrates self-limiting behavior for InCp for exposure times of ~2 seconds. Figure 5.5b shows a similar graph exploring the effect of increasing ozone exposures using the timing sequence 2-2-x-2 and demonstrates self-limiting In_2O_3 growth for ozone exposure times beyond ~2 s. Increasing the InCp and O_3 purge times did not affect the In_2O_3 growth rates indicating that purge times $\geq$ 2 s are sufficient to avoid mixing the precursors. For the remainder of the measurements, a timing sequence of 2-4-2-2 was used unless otherwise noted.

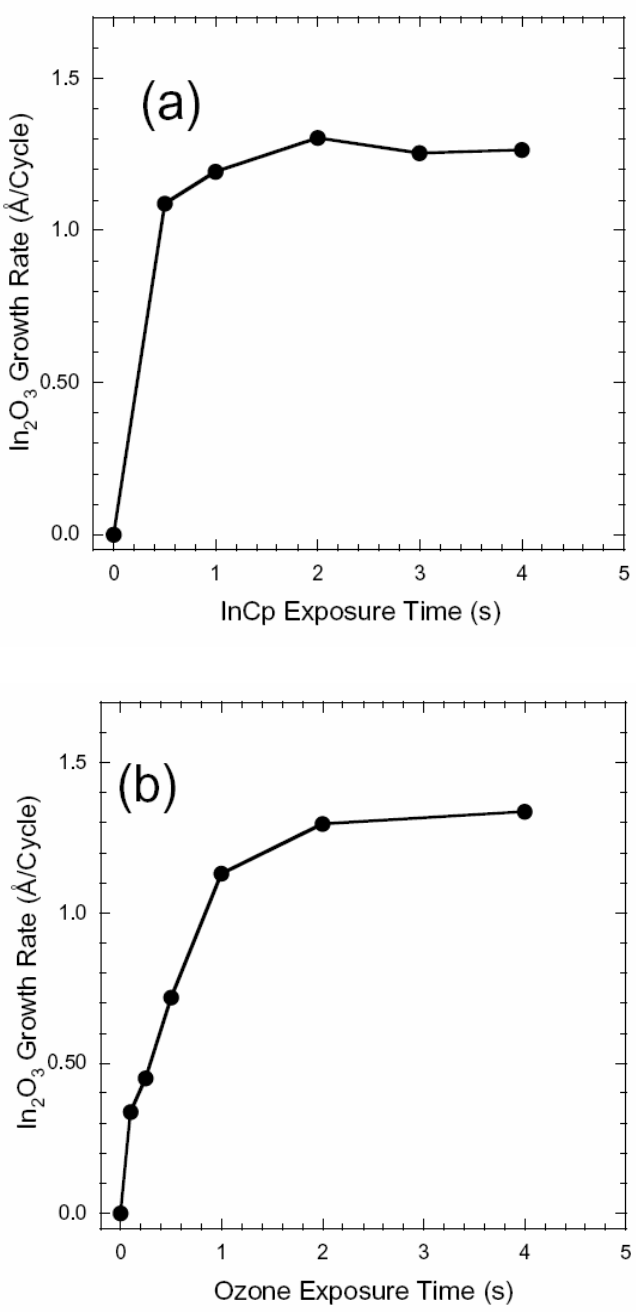

Figure 5.5. (a) In_2O_3 growth rate versus InCp exposure time measured by ellipsometry for films deposited on Si(100) using the timing sequence x-2-2-2 at 250°C. (b) In_2O_3 growth rate versus O_3 exposure time measured similar to Fig 4a using the timing sequence 2-2-x-2.

Figure 5.6 reveals nearly linear In_2O_3 growth over the range of 50-1000 InCp/O_3 cycles at an average growth rate of 2.0 Å/cycle. Figure 5.7 demonstrates that the In_2O_3 growth rate actually increases somewhat with the number of cycles from 1.3-2.0 Å/cycle over the range of 50-2000 ALD cycles. This increase probably results from an increase in surface area with the evolution and growth of the In_2O_3 nanocrystals. Gradual changes in ALD growth rates have been observed previously for nanocrystalline materials in which the morphology or crystal size evolves with film thickness [37, 38]. The effect of deposition temperature on the In_2O_3 growth is shown in Figure 5.8. Surprisingly, the In_2O_3 growth rate drops precipitously below 200°C. We believe that 200°C is the threshold temperature below which ozone no longer decomposes to form oxygen radicals necessary for In_2O_3 growth. Between 200 and 450°C, the In_2O_3 growth rate is nearly constant at 1.2-1.4 Å/cycle. At 500°C, it was difficult to control the film thickness because most of the InCp decomposed at the leading edge of the sample holder in the reactor.

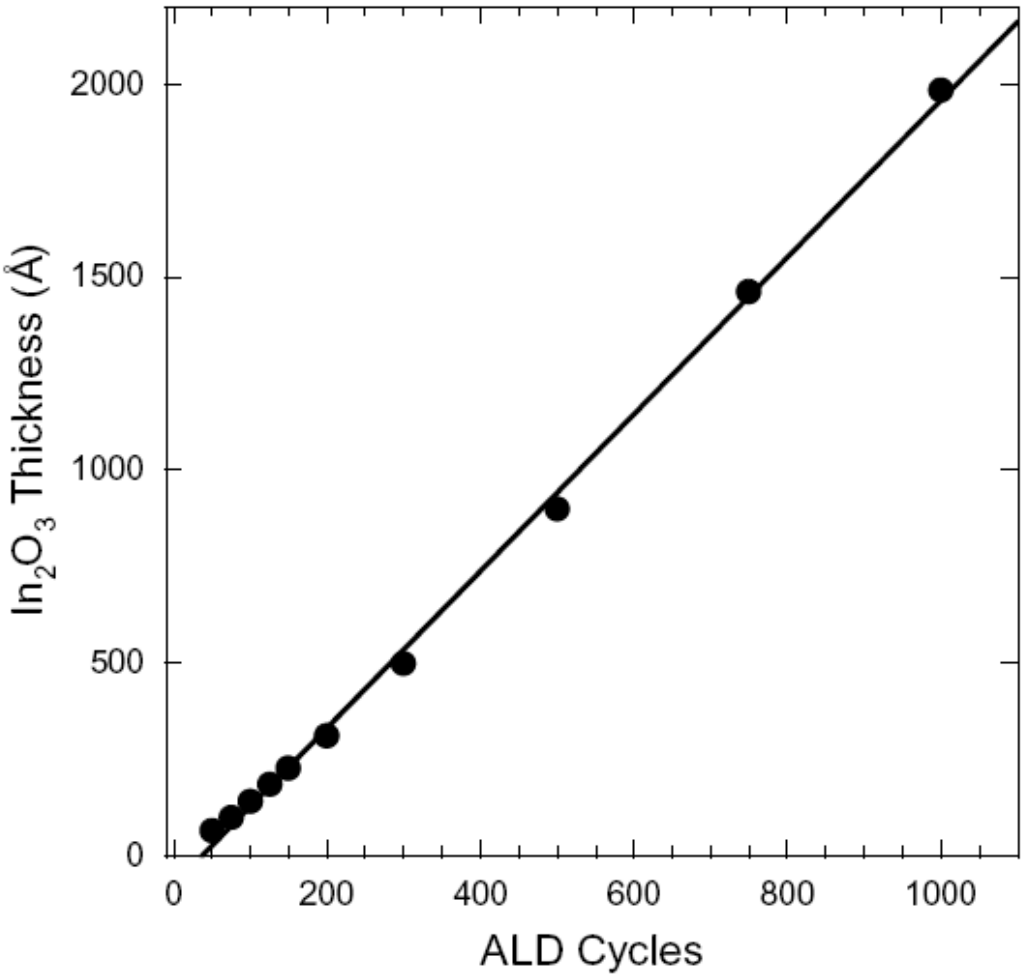

Figure 5.6. In_2O_3 thickness versus number of $InCp/O_3$ cycles measured by ellipsometry for films deposited on Si(100) using the timing sequence 2-4-2-2 at 275°C.

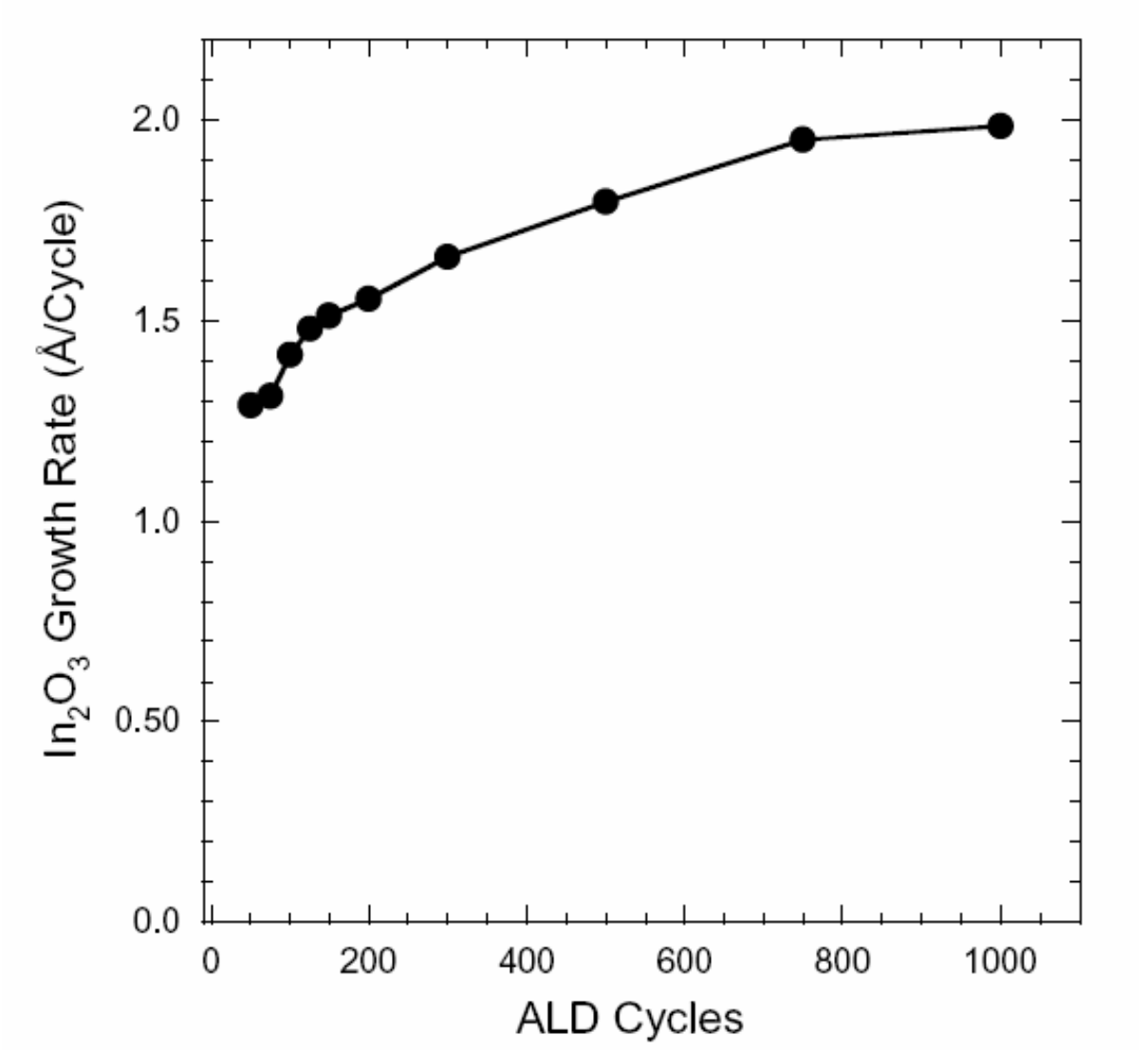

Figure 5.7. In_2O_3 growth rate versus number of cycles derived from Fig. 5.5.

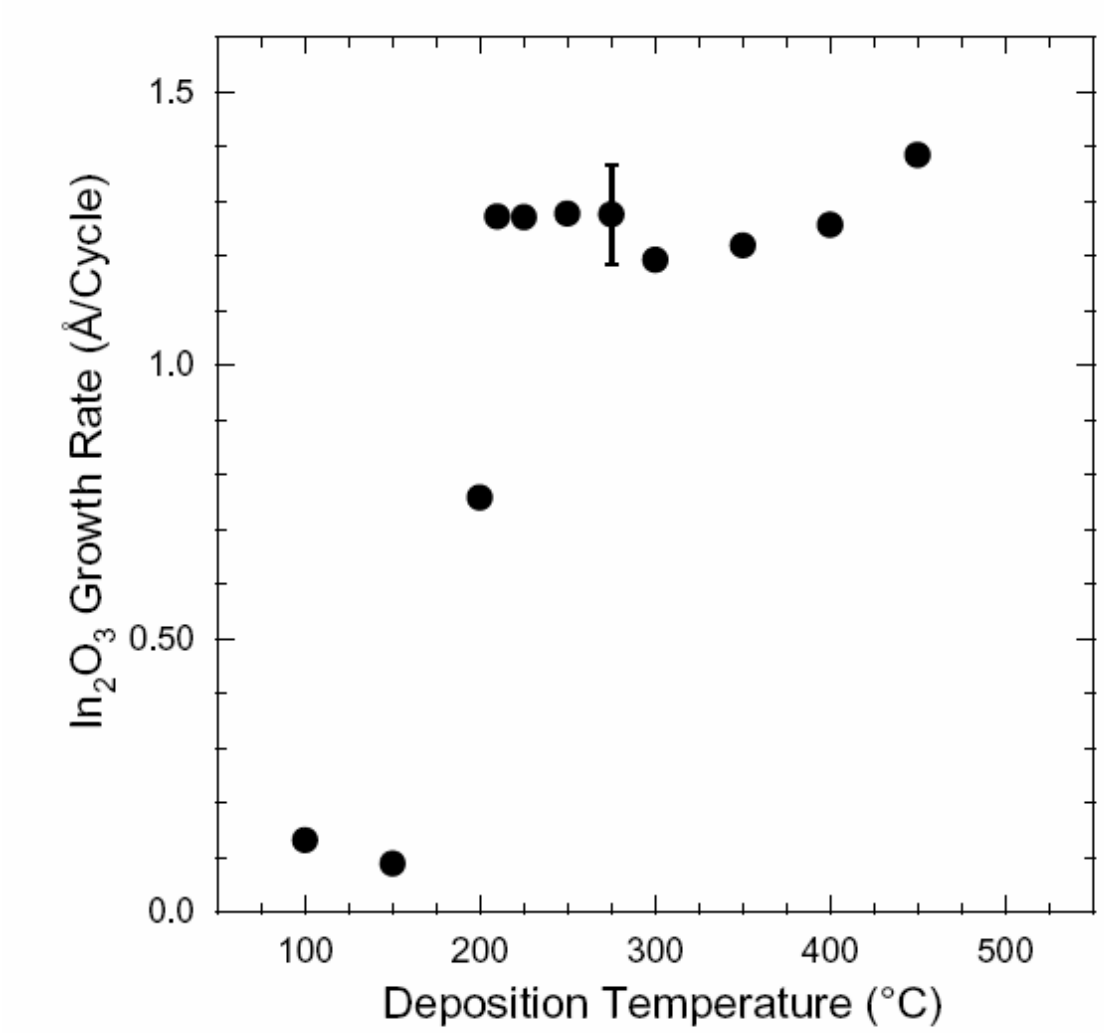

Figure 5.8. In_2O_3 growth rate versus deposition temperature measured by ellipsometry for films deposited on Si(100) using the timing sequence 2-4-2-2.

We also examined the variation in In_2O_3 film thickness along the flow direction of the reactor. Using the 2-4-2-2 timing sequence, the film thickness was constant for the first ~15 cm of the reactor, after which the film thickness dropped off by 53% over 22 cm. The film uniformity improved using 15 s O_3 exposure times so that the thickness decreased by only 33% over 22 cm, but the thickness variation was unaffected using longer InCp exposure times. We attribute this behavior to the depletion of oxygen radicals due to recombination along the flow direction of the reactor.

The results of the film growth studies are summarized in Table 5.2 where we compare the InCp/O_3 process with the existing In_2O_3 ALD process using $InCl_3/H_2O_2$.

Indium Precursor	*$InCl_3$*	*InCp*
Oxygen Source	H_2O_2	O_3
ALD Temperature Window (°C)	300-500	200-450
Precursor Temperature (°C)	285	40
Growth Rate (Å/cycle)	0.4	2.0
Precursor Etching?	Yes	No
Reference	[19]	This work

Table 5.2. Comparison of $InCl_3$ and InCp precursors for In_2O_3 ALD.

5.3.4. Properties of In_2O_3 Films

Figure 5.9 shows an XRD measurement for a 176 nm film deposited on glass at 275°C. The peaks in Figure 5.9 match closely cubic, polycrystalline In_2O_3 (PDF number 00-006-0416) as illustrated by the Miller indices in the figure. In agreement with the XRD, the AFM image in Figure 5.10 reveals a relatively rough, nanocrystalline topography for a 100 nm In_2O_3 film eposited on Si(100). This image has a z-range of 30 nm and yields a root-mean-squared (RMS) roughness of R=3.96 nm for the 1x1 micron scan. The RMS roughness increases somewhat to R=4.9 and 5.8 nm for scan sizes of 2x2 and 10x10 micron, respectively. Nanocrystals with a lateral dimension of 50-100 nm are evident in the plan view SEM image for the 100 nm In_2O_3 sample on Si(100) shown in Figure 1.11. Cross-sectional SEM images (not shown) demonstrate that In_2O_3 films are dense and free of voids, pinholes or cracks.

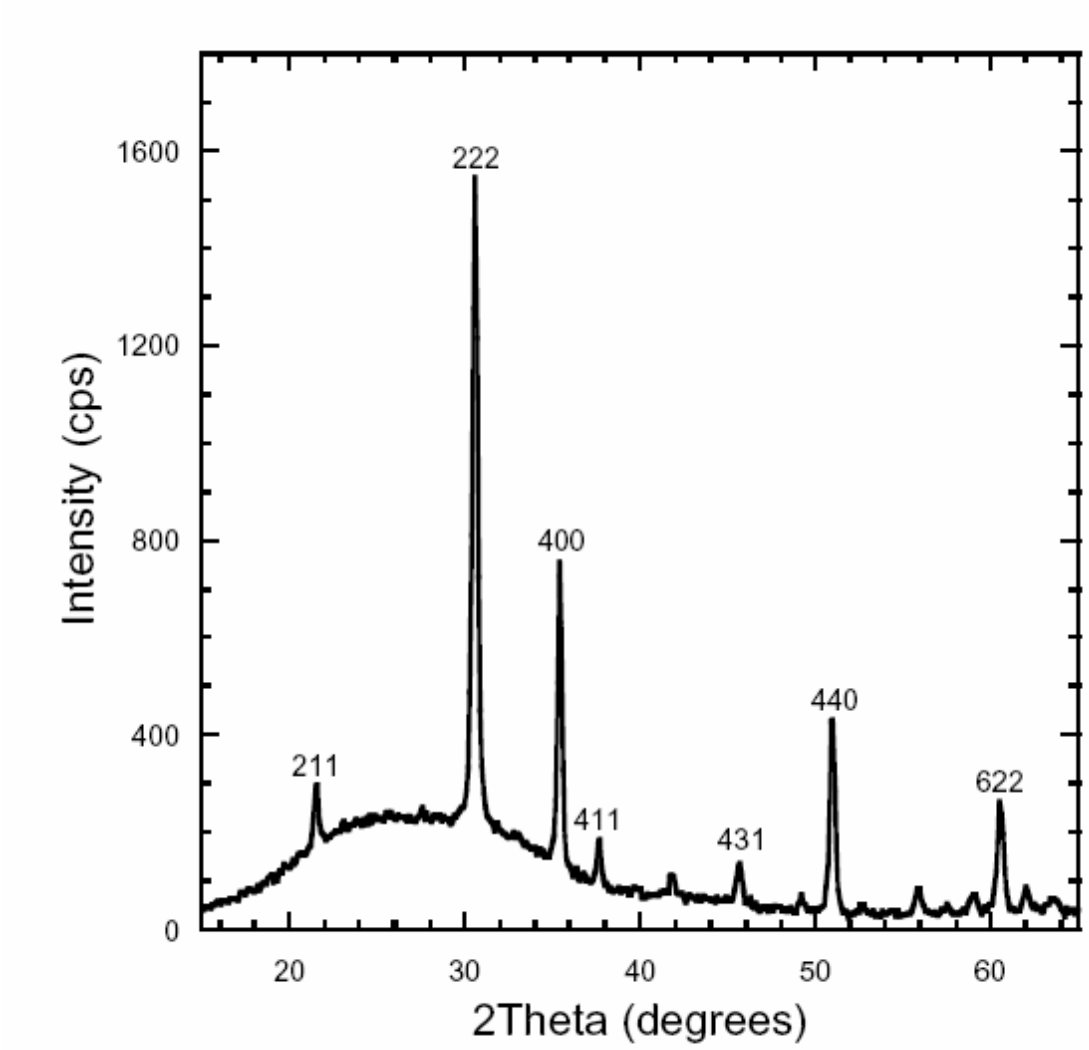

Figure 5.9. X-ray diffractogram recorded from 173 nm ALD In_2O_3 film deposited on glass using the timing sequence 2-4-2-4 at 275°C.

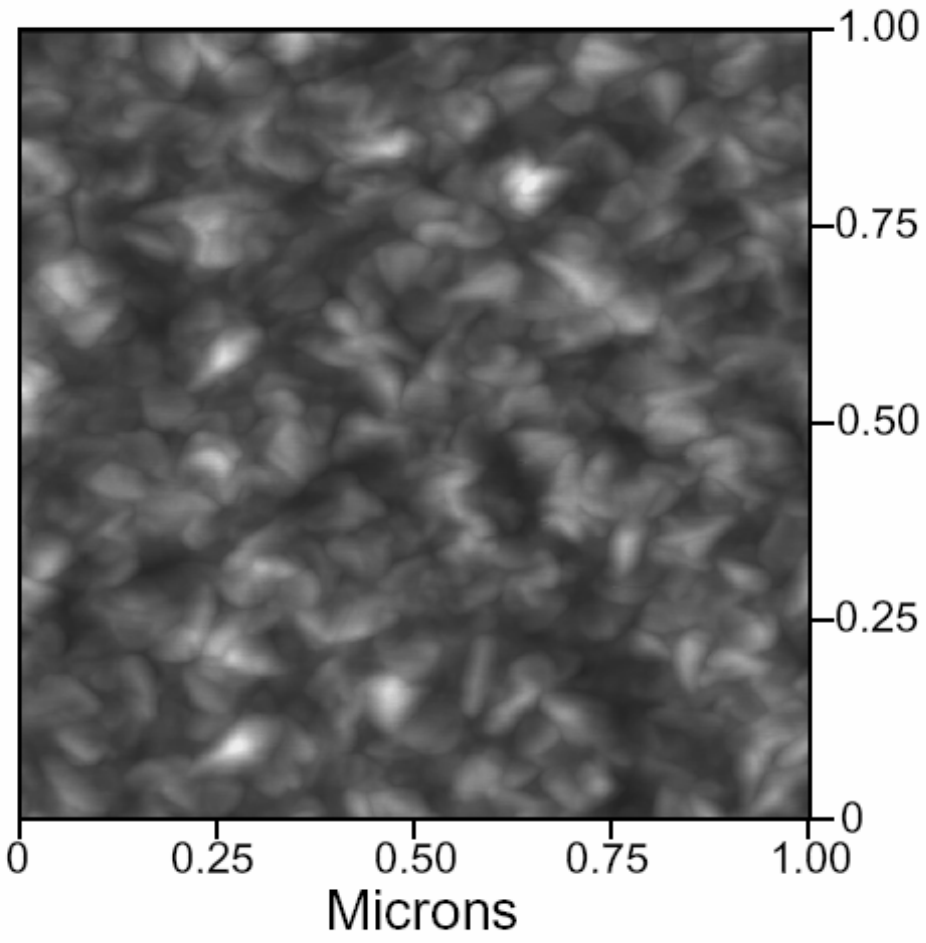

Figure 5.10. Tapping-mode AFM image recorded from 100 nm ALD In_2O_3 film deposited on Si(100) using the timing sequence 2-4-2-4 at 275°C. The contrast scale for this image is 30 nm and the RMS roughness is 3.96 nm.

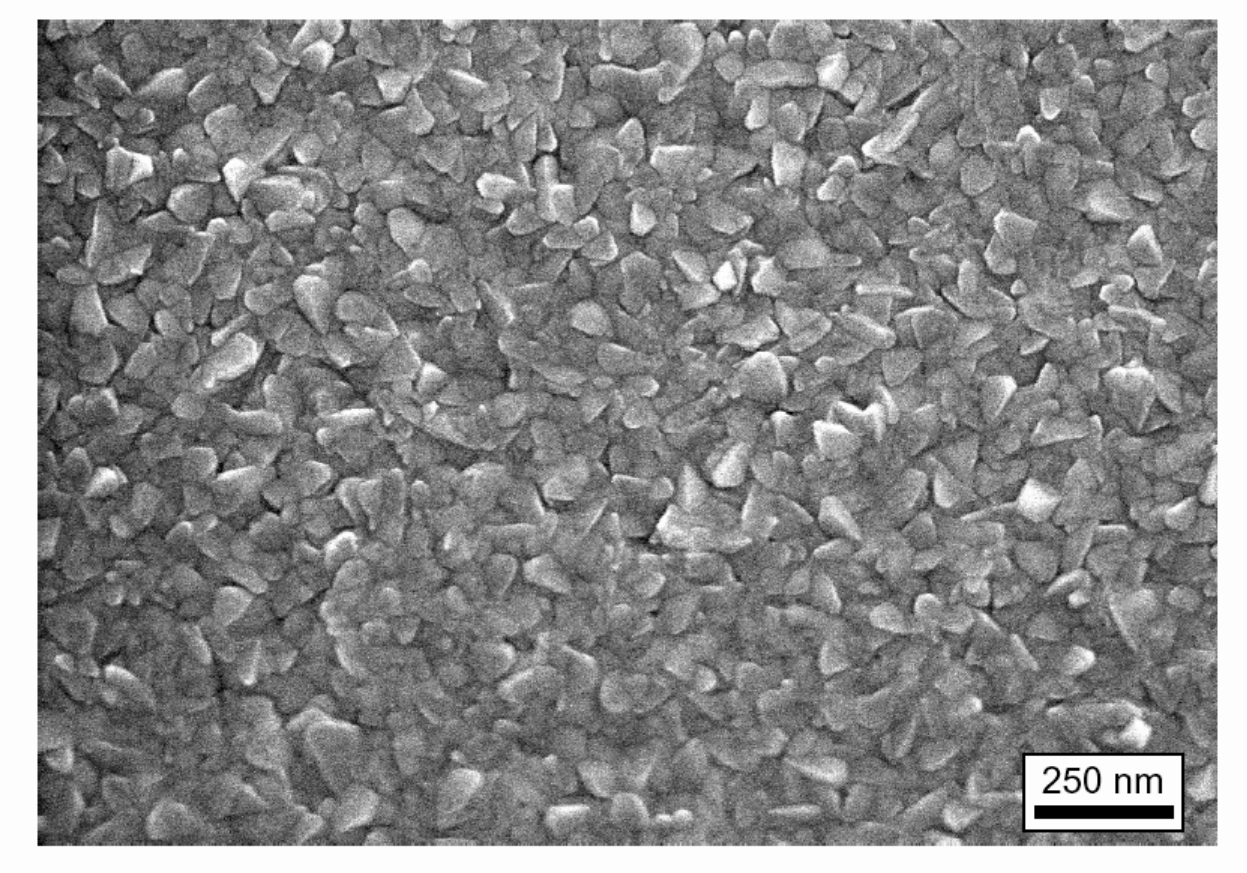

Figure 5.11. Plan view SEM image of 100 nm ALD In_2O_3 film deposited on Si(100) using the timing sequence 2-4-2-4 at 275°C.

Figure 5.12 shows the optical transmission of a 176 nm thick In_2O_3 film deposited on glass (solid line) as well as the transmission for uncoated glass (dashed line). The average transmission of the In_2O_3/glass sample over the wavelength range 400-1000 nm, after dividing by the corresponding average transmission of the uncoated glass, is 97.5%. This film had a resistivity of $16x10^{-3}$ Ω cm. This is somewhat higher than the value of $3\text{-}6x10^{-3}$ Ω cm measured previously for In_2O_3 deposited using $InCl_3/H_2O$[16]. This finding, along with the observation that the previous films were also less transparent, suggests that the O_3 used in our process produces a more perfect In_2O_3 stoichiometry with fewer oxygen vacancies resulting in increased transparency and resistivity.

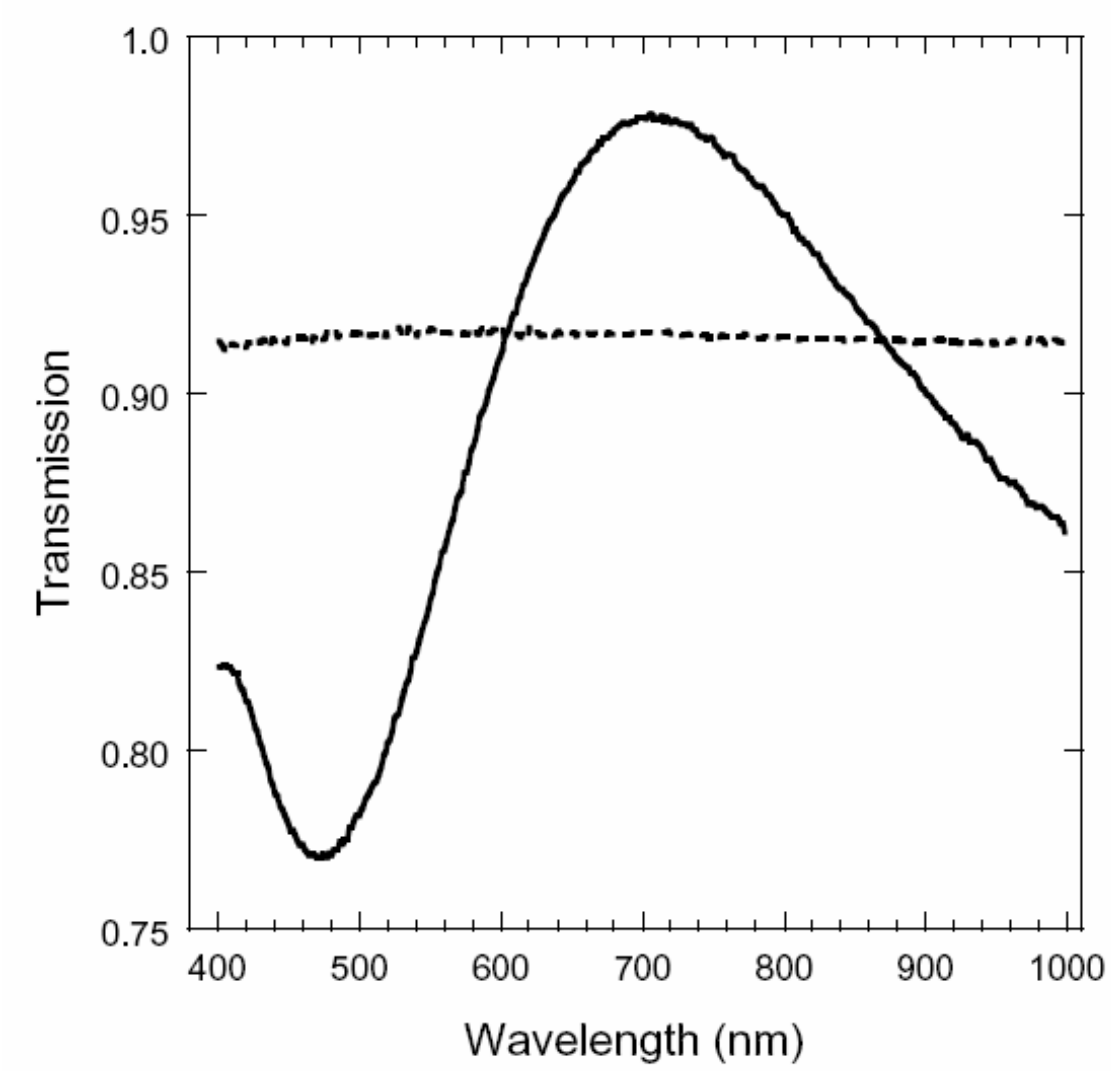

Figure 5.12. Optical transmission spectrum for 173 nm ALD In_2O_3 film deposited on glass using the timing sequence 2-4-2-4 at 275°C (solid line) and for uncoated glass (dashed line).

5.3.5. In_2O_3 ALD in AAO Membranes

Next, we coated AAO membranes with In_2O_3 using 80 InCp/O_3 cycles at 250 °C. The AAO had an initial pore diameter d=200 nm and thickness L=70 microns such that the aspect ratio L/d=350. To allow gaseous diffusion of the precursors into the high aspect ratio pores, relatively long ALD cycle times of 60-15-60-15 were used[24]. Figure 5.13a shows a backscattered electron image recorded from the middle of a cleaved cross section of the AAO membrane. The white lines visible on the edges of the AAO nanopores are the In_2O_3 coating and appear brighter than the surrounding Al_2O_3 because the higher-Z indium backscatters electrons more efficiently. Since this sample was polished prior to imaging, the white lines are unlikely caused by edge-contrast. In fact, the pore structure was practically invisible in secondary electron images (not shown). Figure 5.13b shows an EDAX spectrum taken from the same location at the center of the AAO membrane and the prominent In Lα peak at 3.29 KeV demonstrates that the ALD In_2O_3 completely infiltrates the high aspect ratio AAO membrane. The intensity of the In Lα peak decreases by only 20% between the edge and the middle of the membrane, indicating very high conformality of the ALD In_2O_3 coating. We also coated much higher aspect ratio AAO membranes (L/d=2300) using an identical treatment, but the coating was less conformal and the In Lα signal decreased by ~90% between the edge and the middle of the membrane. This is most likely due to a decrease in concentration of the O_3 or oxygen radicals along the very high aspect ratio pores.

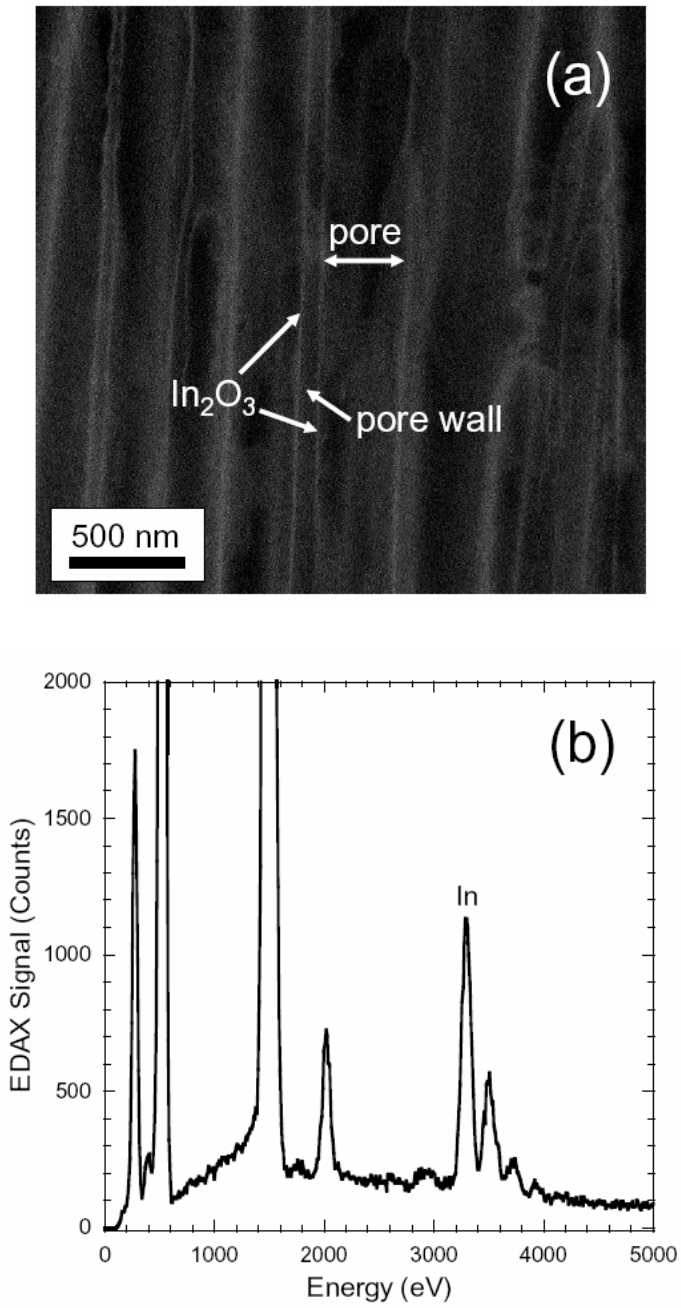

Figure 5.13. (a) Backscattered electron SEM image of cross section of high aspect ratio AAO membrane with 13 nm ALD In_2O_3 coating deposited at 275°C using the timing sequence 60-15-60-15. The white lines visible along the pore walls are the In_2O_3 coating. (b) EDAX spectrum recorded from same location at center of AAO membrane as (a).

5.4. Atomic Layer Deposition of Indium Tin Oxide

5.4.1. Introduction

Indium-tin oxide (ITO) is a transparent conducting oxide material with a wide range of uses. Thin films of ITO are used in transparent electrodes for flat panel displays, light emitting diodes, and solar cells. ITO is also used as a heat reflecting layer to improve the energy efficiency of architectural glass. ITO thin films can be deposited in a variety of ways including sputtering[39], spray pyrolysis[40], sol-gel methods[41], chemical vapor deposition[42], pulsed laser deposition[43], and atomic layer deposition (ALD)[16, 19, 44]. ALD ITO films have been prepared previously using $InCl_3$, $SnCl_4$ and either H_2O[44] or H_2O_2 [19] as the oxygen source. This method suffers from limitations including low growth rates, high deposition temperatures, the low volatility $InCl_3$, and the inconvenience of using halogenated precursors. The chlorinated precursors as well as the HCl byproduct are corrosive and can etch the substrates and damage the deposition equipment. For instance, large exposures to $InCl_3$ can etch the deposited In_2O_3.[16] This behavior is especially problematic when trying to infiltrate porous substrates where large reactant exposures are needed to ensure diffusion throughout the substrate [24]. Finally, halogenated precursors can form agglomerates during large exposures leading to non-uniform deposits[45].

We have recently started using ALD techniques to apply transparent, conducting coatings onto porous supports such as anodic aluminum oxide (AAO) membranes to synthesize electrodes for dye sensitized solar cells [46]. As part of this effort, we have developed new methods for depositing ALD In_2O_3 films using alternating exposures to cyclopentadienyl indium (InCp) and ozone[47] and also SnO_2 films using alternating exposures to tetrakis(dimethylamino) tin

(TDMASn) and H_2O_2 [48]. In this manuscript, we demonstrate how the ALD procedures for In_2O_3 and SnO_2 can be combined to make ITO thin films.

5.4.2. Experimental

SnO_2 ALD was performed using alternating exposures to tetrakis(dimethylamino) tin (TDMASn, Gelest, >95% purity) and hydrogen peroxide (H_2O_2, Aldrich, 50 wt% in water). In_2O_3 ALD was performed using alternating exposures to cyclopendadienyl indium (I) (InCp, Strem, electronic grade 99.999+% In) and ozone. The ozone was produced using a commercial ozone generator (Ozone Engineering L11) using a feed of ultrahigh purity oxygen at a flow rate of 400 sccm to produce ~10% ozone in oxygen. Both the TDMASn and InCp are held in separate stainless steel bubblers maintained at 40°C, and the tubing connecting the bubblers to the ALD reactor is heated to 150°C to prevent condensation of the precursors on the reactor walls. Ultrahigh purity nitrogen at a mass flow rate of 60 sccm was sent through the bubblers during the reactant exposures, and was diverted to bypass the bubblers following the reactant exposures.

The ALD timing sequences can be expressed as t1-t2-t3-t4 where t1 is the exposure time for the first precursor, t2 is the purge time following the first exposure, t3 is the exposure time for the second precursor, and t4 is the purge time following the exposure to the second precursor with units in seconds (s). Based on our previous studies, the timing sequence used for In_2O_3 ALD was 2-4-2-2, and the timing sequence used for SnO_2 ALD was 1-5-1-5. ITO ALD was accomplished by alternating between the InCp/O_3 cycles for In_2O_3 ALD and the TDMASn/H_2O_2 cycles for SnO_2 ALD. The composition of the films was controlled by adjusting the percentage of SnO_2 cycles that were substituted for In_2O_3 cycles.

The ALD films were deposited on 2 x 2 cm Si(100) and glass substrates. Prior to loading, the substrates were cleaned in an ultrasonicator using acetone and then isopropanol and blown dry using nitrogen. After loading, the substrates were allowed to outgas in the ALD reactor for 10 minutes at the deposition temperature (typically 275°C) in 1 Torr of flowing ultrahigh purity nitrogen. Next, the substrates were cleaned *in situ* using a 60 s exposure to 10 % ozone in oxygen at a pressure of 2 Torr and a mass flow rate of 400 sccm.

In our previous study of In_2O_3 ALD, we observed a reactor conditioning effect in which the thicknesses of In_2O_3 films deposited immediately following the growth of a different material, such as Al_2O_3 or SnO_2, were thinner than expected[47]. To compensate for this effect, we always deposited an In_2O_3 buffer layer on the inside of the reactor using ~100 InCp/O_3 cycles following depositing of a different material. After depositing this buffer layer, we would proceed with the ITO deposition experiments.

5.4.3. Results and Discussion

In order to deposit a mixed-oxide material such as ITO by ALD, it must be possible to deposit the component oxides (In_2O_3 and SnO_2) at a common temperature or range of temperatures. In other words, the ALD temperature "windows" for the component materials must overlap. Figure 5.14 shows that In_2O_3 can be deposited between 200-450°C[47]. At lower temperatures the O_3 decomposition shuts off thereby preventing deposition, and at higher temperatures the InCp decomposes. SnO_2 can be deposited between 50-325°C[48]. The lower temperature limit is fixed by the TDMASn vaporization temperature of 40°C, while at higher temperatures the TDMASn begins to decompose. As Figure 5.14 shows, there should be a

temperature window for ITO ALD between 200-325°C. Consequently, a deposition temperature of 275°C was selected for the initial experiments.

In situ QCM and QMS measurements were performed to investigate the discrepancies in thickness and composition. Figure 5.15 shows the QCM signals recorded during the ALD of ITO using 10% SnO_2 cycles at 275°C. This figure plots the growth rate measured during each ALD cycle assuming densities of 7.19 and 6.95 g/cm^2 for the In_2O_3 and SnO_2, respectively. Although the steady-state growth rate measured for In_2O_3 using the QCM is ~1.4 Å/cycle, the In_2O_3 growth rate drops to ~1 Å/cycle after each SnO_2 cycle. Following the SnO_2 cycles, the In_2O_3 growth rate increases towards the steady-state value over the following 5-7 cycles. Apparently, the SnO_2 temporarily inhibits the In_2O_3 growth.

Next, QMS experiments were performed to explore the origin for the inhibited In_2O_3 growth following the SnO_2 cycles. Figure 5.16a shows the m=66 signal from cyclopentadiene versus time measured during the ALD of ITO using 5% SnO_2 cycles at 275°C. The TDMASn exposures for each SnO_2 cycle are indicated in the figure. Cyclopentadiene is released exclusively during the InCp exposures, and the magnitude of the m=66 signal is proportional to the amount of In_2O_3 deposited during each ALD cycle.[47] In agreement with the QCM measurements, Figure 5.16a shows that the In_2O_3 growth rate decreases substantially following each SnO_2 cycle, and 8-12 In_2O_3 cycles are required for the In_2O_3 growth rate to recover to the steady-state value.

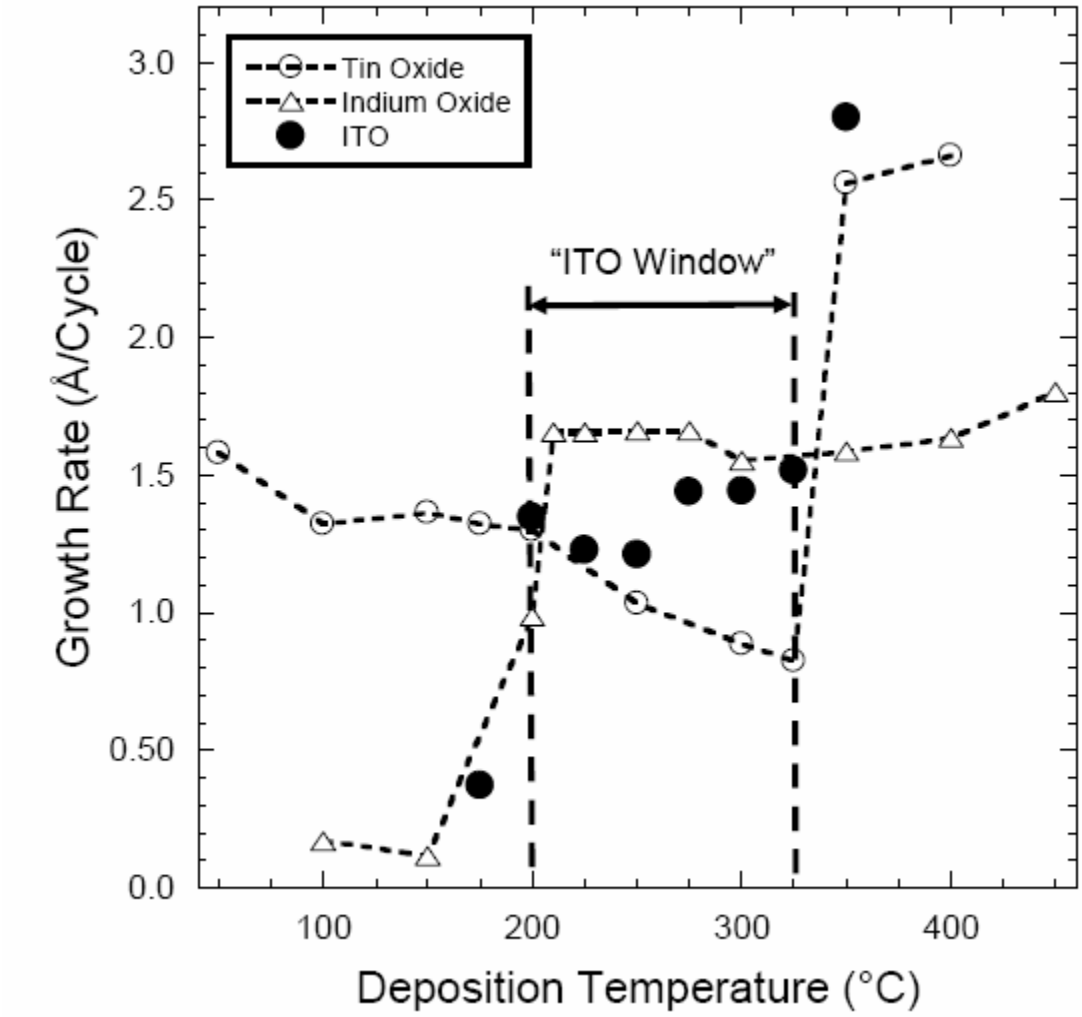

Figure 5.14. ALD growth rates for In_2O_3 (triangles), SnO_2 (open circles), and ITO (solid circles) versus deposition temperature. Potential ALD window for ITO growth is indicated.

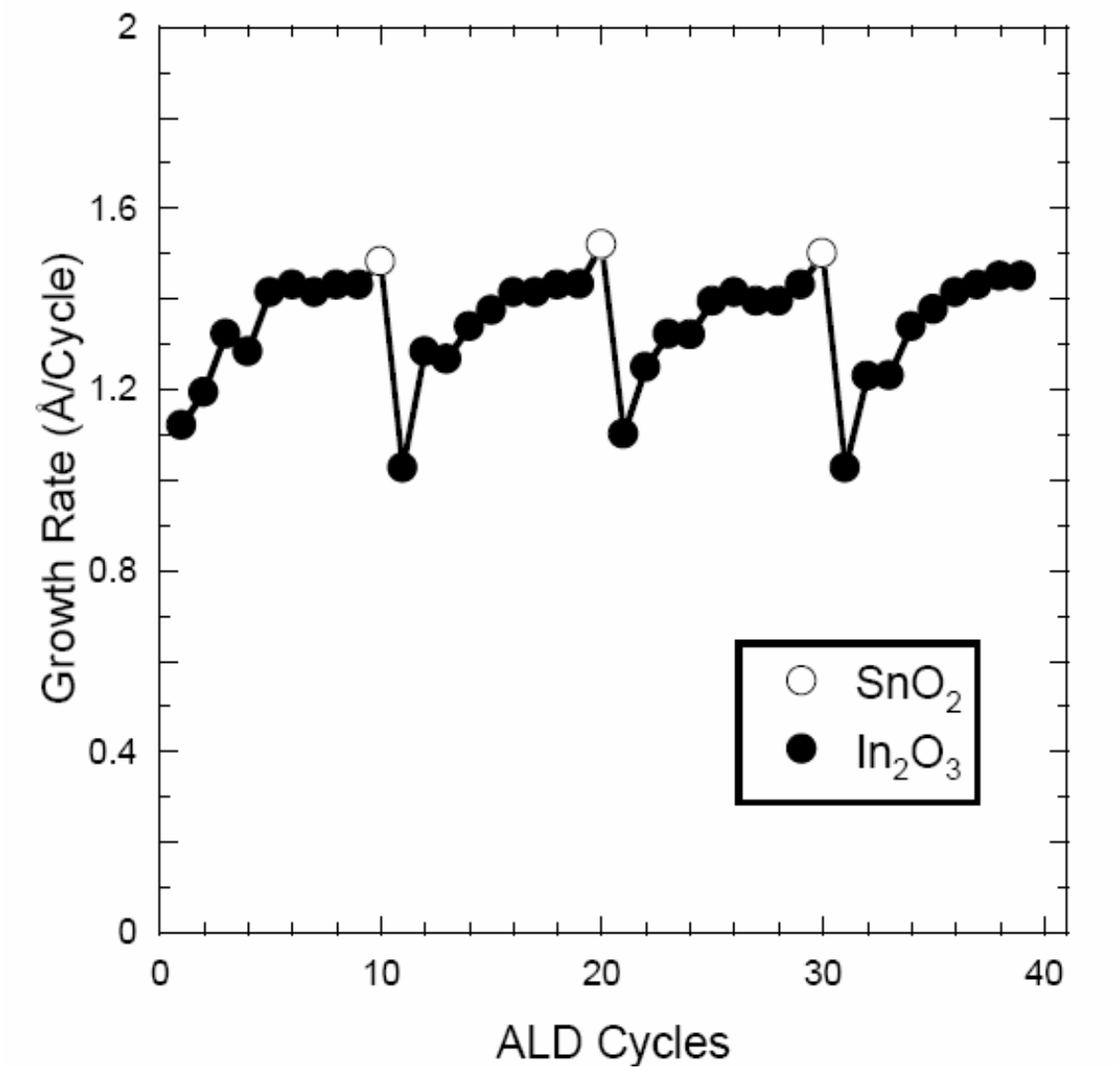

Figure 5.15. Growth rate versus ALD cycles measured using *in situ* QCM during ITO growth using 10% SnO_2 cycles.

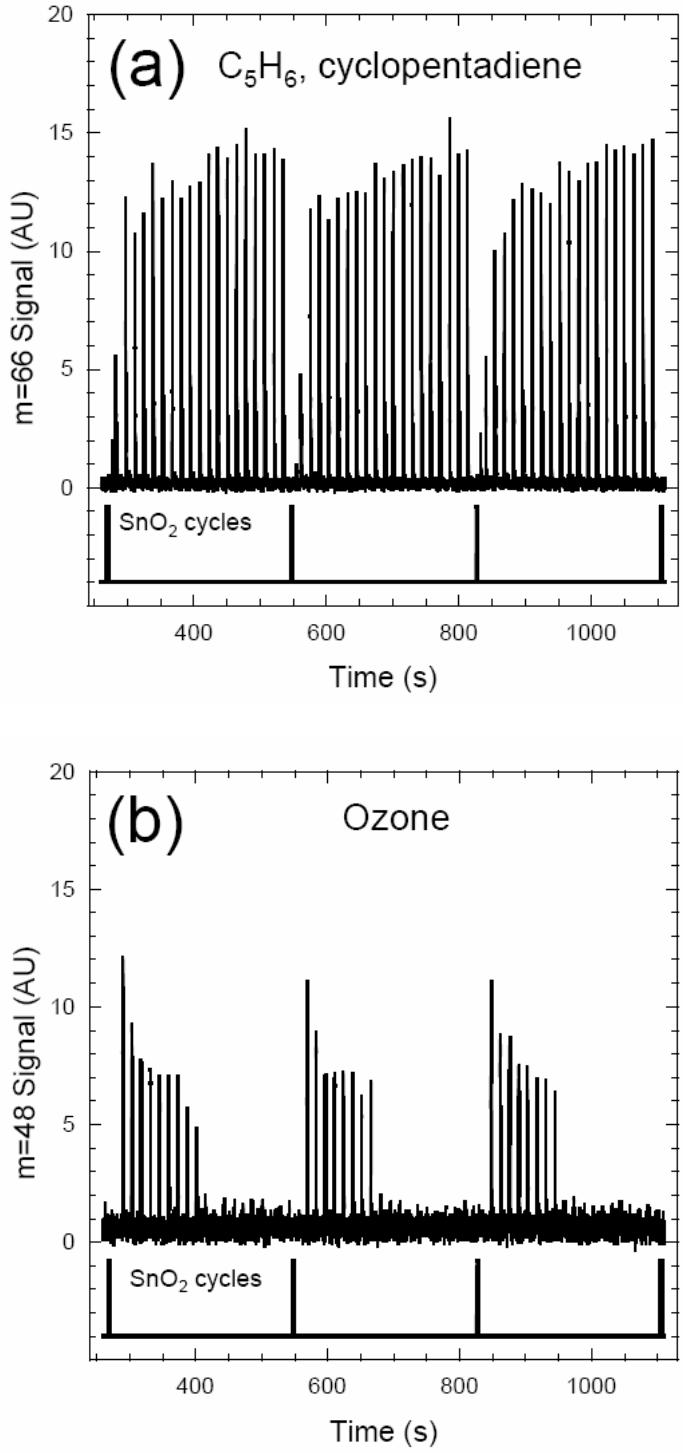

Figure 5.16. *In situ* QMS measurements for (a) m=66 from cyclopentadiene, and (b) m=48 from ozone, measured during ITO ALD using 5% SnO_2 cycles. The application of the SnO_2 ALD cycles is indicated.

Figure 5.16b presents the m=48 signal for O_3 that was recorded simultaneously with the m=66 data in Fig. 5a. No O_3 is observed during the In_2O_3 ALD when the In_2O_3 growth rate has reached the steady-state value. This observation is consistent with our previous finding that O_3 decomposes the In_2O_3 very efficiently, and this decomposition is necessary for the In_2O_3 growth[47]. Curiously, the m=48 signal returns during the O_3 exposures that immediately follow the SnO_2 ALD cycles, and this O_3 signal persists for approximately 8-10 cycles.

Figures 5.15 and 5.16 demonstrate that the SnO_2 cycles inhibit the subsequent In_2O_3 ALD, and this may result from the suppression of O_3 decomposition by the SnO_2. In our previous In_2O_3 ALD study, we observed a reactor conditioning effect in which the thicknesses of In_2O_3 films deposited immediately following Al_2O_3 growth were thinner than expected. To compensate for this effect, we always deposited an In_2O_3 buffer layer on the inside of the reactor following depositing of a different material. Evidently, the SnO_2 deposited during a single SnO_2 cycle is sufficient to suppress the O_3 decomposition necessary to sustain the In_2O_3 growth.

Once the growth behavior of the ALD ITO films was understood, we proceeded to measure the properties of the films to determine the effect of the deposition conditions on the resistivity, transparency, and morphology of the ITO. Figure 5.17a shows the ITO resistivity versus percent SnO_2 cycles determined using four point probe measurements of films prepared on glass at 275°C using 300 ALD cycles. Initially, the ITO resistivity decreases dramatically from $1.4x10^{-2}$ Ωcm at 0% SnO_2 cycles to $3.9x10^{-4}$ Ωcm at 5% SnO_2 cycles, and then increases slightly to $1.1x10^{-3}$ Ωcm at 25% SnO_2 cycles.

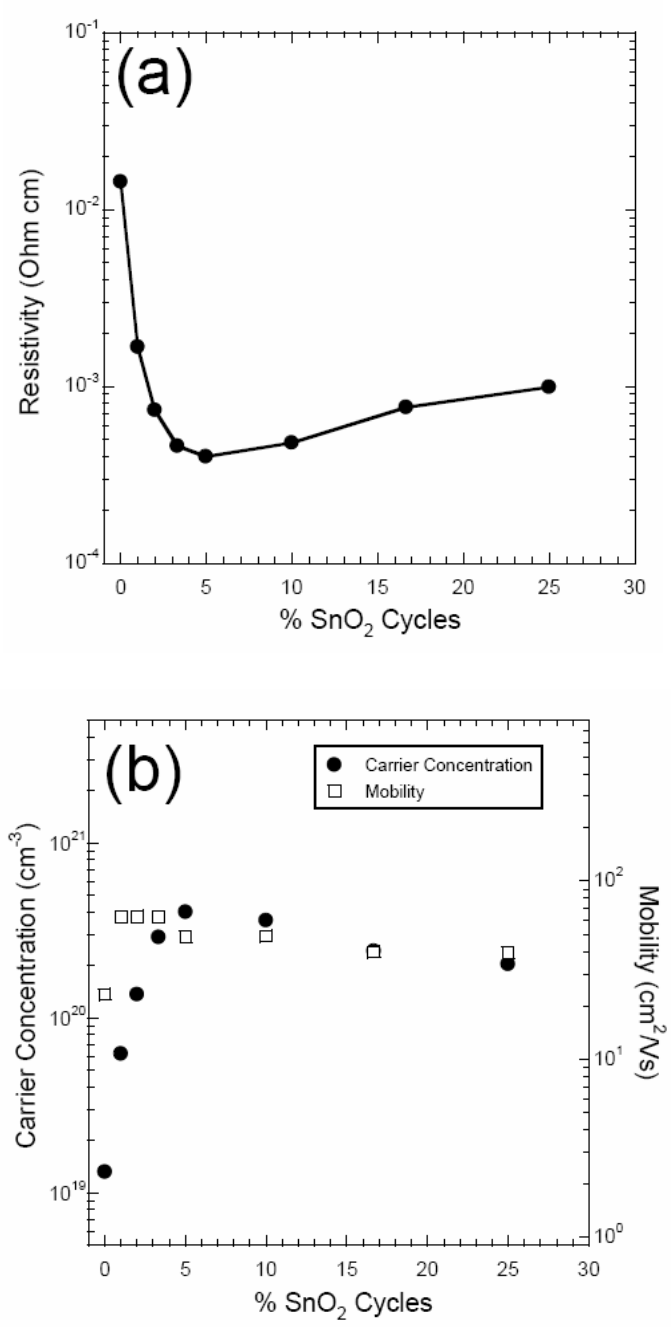

Figure 5.17. (a) Resistivity versus percentage of SnO_2 cycles measured using four point probe for ALD ITO films prepared on glass at 275°C using 300 cycles. (b) Hall probe measurements of the same ITO films showing carrier concentration and mobility.

Hall probe measurements performed on the samples prepared on glass confirmed that the ITO films are n-doped, and the Hall probe resistivity values were nearly identical to those obtained using the four point probe. The carrier concentration and mobility values obtained using the Hall probe (Figure 5.17b) reveal that the decrease in resistivity with SnO_2 doping can be mostly attributed to an increase in carrier concentration. The carrier concentration increases from $1.3x10^{19}$ cm^{-3} at 0% SnO_2 cycles to $4.0x10^{20}$ cm^{-3} at 5% SnO_2 cycles. In contrast, the mobility only increases from 23 to 49 cm^2/Vs over this range. The electrical characteristics of the ITO films prepared using 5% SnO_2 cycles in this study are comparable to values obtained for ALD ITO films deposited previously using metal chloride precursors.[44] In addition, these electrical transport values are very similar to the values measured for commercially available ITO films prepared using sputtering.

It is interesting to compare the carrier concentration determined by the Hall probe measurements with the actual concentration of Sn atoms in the ITO films measured by XRF. The ratio of these values is known as the doping efficiency, and this quantity assumes that every Sn atom contributes one free electron. For the ITO film prepared using 5% SnO_2 cycles, the Hall probe measured a carrier concentration $n=4.0x10^{20}$ cm^{-3}, while XRF yielded 4.9% SnO_2 for this film. Using the atomic density of bulk In_2O_3, this composition corresponds to a Sn atom density of $7.6x10^{20}$ cm^{-3} so that the doping efficiency is 53%. This number compares favorably with ITO films of similar Sn content prepared by sol-gel techniques[41]. It is thought that the remaining 47% of the Sn atoms form neutral clusters such as Sn_2O_3 which do not contribute to the ITO conductivity. Perhaps by doping the In_2O_3 using a different SnO_2 precursor with a lower growth rate than TDMASn, the Sn atoms could be spaced farther apart to avoid forming neutral clusters, thereby increasing the doping efficiency.

5.4.4. High Surface Area ITO

We used the ALD methods described in the preceding sections to synthesize transparent, conducting electrodes to be used for spectrophotochemical applications. First, a thin ITO coating was deposited on a commercial anodic AAO membrane that completely infiltrated the AAO pores to create a conformal, uniform coating with a thickness of 9.7 nm. This process used 58 ALD cycles with 10% SnO_2 cycles at a temperature of 275°C with the timing sequence 12-10-60-5 for In_2O_3 and 10-10-10-10 for SnO_2. Next, the AAO was mounted in a fixture that limited deposition to the front, 20 nm pore side of the membrane and an ITO film with a thickness of 161 nm was deposited. The function of this thick layer was to seal off the small pores and also to provide a low resistance contact to the electrode. The thick layer used 1000 cycles with 5% SnO_2 cycles at a temperature of 275°C with the timing sequence 2-4-2-2 for In_2O_3 and 1-5-1-5 for SnO_2.

Cross-sectional SEM images of the resulting electrode are shown in Figure 5.18. Figure 5.18a demonstrates that the 20 nm pores of the membrane are completely sealed, while the underlying 200 nm pores are still open beneath the thick coating. Figure 5.18b is a higher resolution image showing that the inside surfaces of the pores are decorated with ITO nanocrystals. The coated membrane had a 5Ω resistance through the membrane, a 15 Ω/□ sheet resistance on the thickly coated side, and an optical transparency of ~70%.

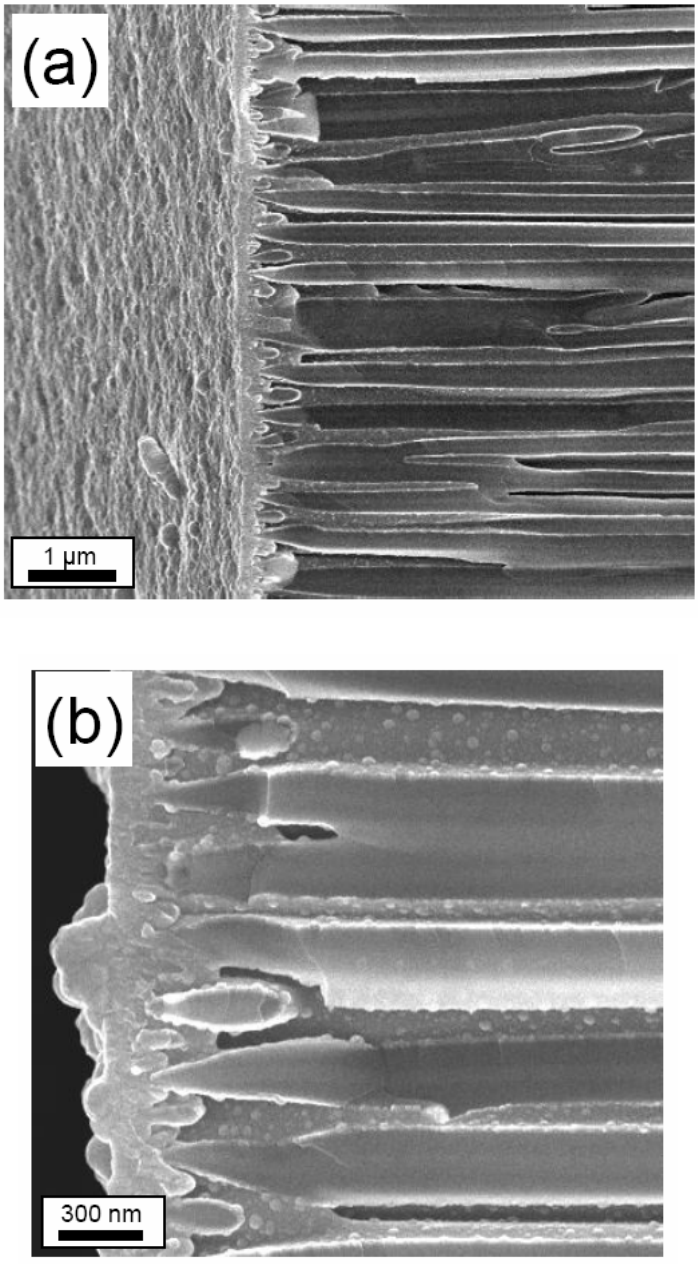

Figure 5.18. (a) Cross sectional SEM image of AAO membrane coated conformally with 9.7 nm ALD ITO film, and also with 161 nm ALD ITO film deposited selectively on the AAO front surface visible on the left side of the image. (b) Higher resolution SEM image of AAO membrane showing that the 20 nm pores are sealed, and ITO nanocrystals decorate the inner walls of the 200 nm pores.

5.5. Conclusions

We have presented a method for preparing In_2O_3 films by ALD using alternating exposures to cyclopendadienyl indium (I) and ozone. This method yields a growth rate of 1.3-2.0 Å/cycle over the temperature range 200-450 °C using a precursor evaporation temperature of only 40°C. *In situ* measurements reveal a mechanism in which approximately 1 in 6 of the initial Cp ligands remain on the surface following each InCp exposure, and the remaining Cp ligand is burned off during the subsequent O_3 exposure to form CO_2. The reactive sites for InCp adsorption are likely to be OH groups formed by during the preceding oxidation step, and the active oxidizing species is believed to be oxygen radicals formed by O_3 thermal decomposition on the reactor walls. The resulting films are nanocrystalline, cubic In_2O_3 that is highly transparent and conducting. Using this method, we demonstrate for the first time the conformal coating of very high aspect ratio porous membranes with ALD In_2O_3.

Furthermore, we have demonstrated a new method for depositing ITO thin films by ALD using alternating InCp/O_3 exposures for In_2O_3 and TDMASn/H_2O_2 exposures for SnO_2. By adjusting the relative number of In_2O_3 and SnO_2 ALD cycles, ITO films were deposited with precise control over the thickness and SnO_2 content. ITO films with a thickness of 42 nm deposited on glass using 5% SnO_2 cycles exhibited a resistivity of $3x10^{-4}$ Ωcm and an optical transparency of 92%. The ITO films were slightly thinner and contained more SnO_2 than predicted, and *in situ* measurements revealed that these discrepancies result from an inhibition of the In_2O_3 growth following the SnO_2 cycles. We have used this new ALD method to apply conformal ITO layers on very high aspect ratio porous membranes.

Chapter 6. Radial Electron Collection in Dye-Sensitized Solar Cells

6. Chapter Overview

In many ways the theoretical, experimental, and instrumental developments described in the first five chapters of this work are a prelude to this, the final chapter. As is often the case, steady progress toward an ambitious original research proposal resulted in several interesting digressions that comprise the bulk of this dissertation. But at the outset, the hypothesis was that in order to accommodate an array of interesting (and potentially superior) redox shuttles for dye-sensitized solar cells (DSSCs), electrons injected into the semiconducting oxide must be collected dramatically faster. We posited that the most effective route to radically reducing extraction times was to bring the current collector to the electrons. That is, by depositing the TCO deep inside the photoanode we aimed to decrease the electron diffusion distance (while retaining a large surface area) by radially collecting electrons. The new photoelectrode architecture is comprised of concentric conducting and semiconducting nanotubes grown within anodic aluminum oxide (AAO), Figure 6.1b. Atomic layer deposition is employed to grow indium tin oxide (ITO) within the porous template and subsequently coat the high area photoelectrode with amorphous TiO_2. Compared to control devices lacking a current collector within the pores, the new photoelectrode geometry exhibits dramatically higher current densities, an effect attributed to the radial collection of electrons. In many ways the new nanoscale architecture is a return to simple bilayer heterojuction photovoltaics. The advantage here is that a relatively large surface area can be packed into a significantly smaller projected area by "folding" the heterojuction over an inert and transparent template.

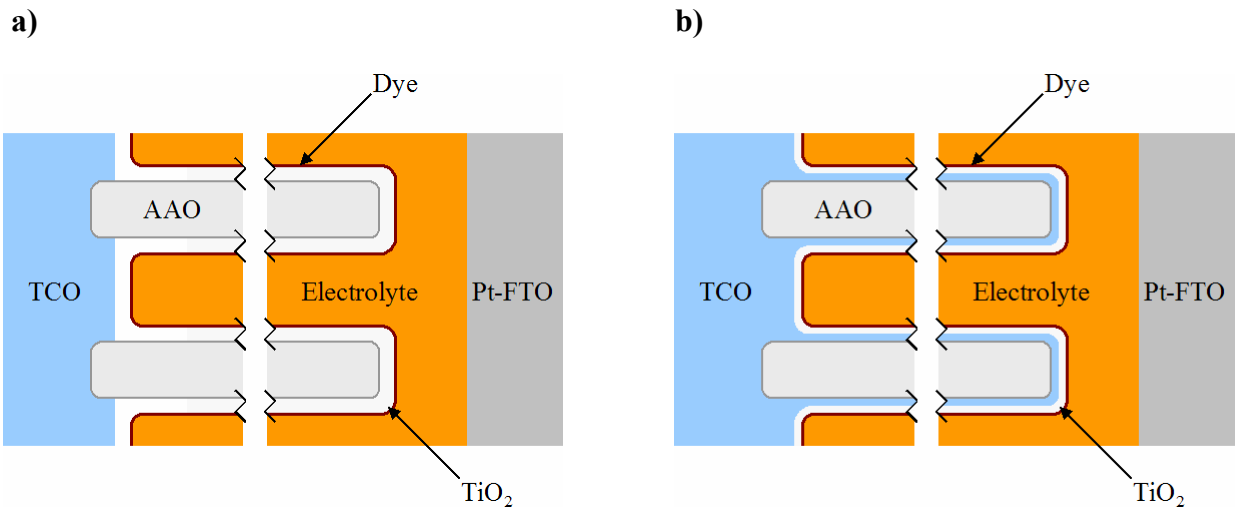

Figure 6.1. Idealized 2-D cross-section of **a)** a nanotube DSSC photoanode and **b)** a concentric nanotube DSSC photoanode with ITO lining the pores.

6.1. Introduction

In the most efficient DSSCs to date, the superior light harvesting efficiency of photons throughout the visible spectrum is realized by a ~14 μm thick nanoparticle photoanode with roughness > 2000.[1] The implications of this architecture define DSSCs as a class of photovoltaics (PVs) with

1) an exceedingly large, heterogeneous interface through which electrons may be (parasitically) intercepted
2) slow electron transport controlled by trap-limited hopping through a relatively long and tortuous path to the transparent electrode.[2, 3]

Given a charge collection time of milliseconds at the maximum power point,[4] efficient charge extraction is only made possible through the extraordinarily slow interception of electrons by adjacent I_3^-. Thus, what promises to be a *tour de force* in photoelectrochemical energy conversion has so far only offered a limited variable space in which efficient devices are realized. Particularly lacking is an assortment of redox couples that permit reasonable collection efficiency, the current number able to be counted upon one hand.[5-8] Furthermore, the most successful shuttle to date, iodide/triiodide (I^-/I_3^-), builds in photovoltage losses of ca. 500 to 600 mV on account of the high driving force needed to regenerate dyes at acceptable rates. Additionally, the iodine-based redox shuttle remains poorly understood owing to its multielectron nature and nonconformity to simple rate laws.[9] One consequence of the "shuttle problem" has been efficiency improvements of only ~1% in DSSC devices over the past 15 years.[1, 10]

In order to accommodate the faster electron interception rates of alternative redox shuttles, the collection time of electrons traversing the photoanode must be reduced. In the limit

of rapid dye regeneration, the collection of electrons at the transparent conducting electrode (TCO) is in competition only with the interception of electrons by the oxidizing redox species. Since electron transport through the wide bandgap semiconductor is typically diffusion controlled, the transport time is inversely proportional to the effective electron diffusion constant and goes as the inverse square of photoanode thickness. Therefore, two distinct strategies may make devices more tolerant to faster interception (i.e. alternative redox couples) – accelerating electron diffusion or reducing the photoanode thickness. Appeals to the first strategy are the motivation for recent reports of 1D nanorod and nanotube photoanodes with relatively large crystalline domains compared to nanoparticles photoanodes.[11-13] Although yet to be tested with alternative redox couples, these novel photoanodes show potential to collect electrons over greater distances relative to their nanoparticle analogues. While the second strategy is straightforward, reducing the photoanode thickness results in a proportional reduction in surface area for dye loading, ultimately resulting in loss of light harvesting efficiency (unless suitable super-chromophores are devised). Overviews of the intricacies of DSSC charge dynamics, as modeled by the continuity equation for DSSCs, have been communicated by several authors.[14-17]

Herein we introduce a new device architecture in which the electron collection distance is reduced by orders of magnitude, without a significant reduction in surface area, by extending the transparent electrode deep within the semiconductor framework. The architecture is an elaboration of a previous design[12] in which wide bandgap semiconductor tubes were grown within the pores of anodic aluminum oxide (AAO) by atomic layer deposition (ALD), Figure 6.1a. By leveraging the broad synthetic palette of ALD, a variety of metal oxides tubes may be fabricated inside AAO including transparent conducting oxides (TCOs).[18-20] In this report, indium tin oxide (ITO) is grown within and upon AAO to produce a transmissive and conductive

high-area electrode. Subsequent deposition of amorphous TiO_2 within the pores of the electrode yields a high-area photoanode suitable for implementation in DSSCs. A highly idealized schematic of the new architecture is shown as Figure 6.1b. In contrast to a conventional DSSC photoanode, in which electrons diffuse the length of the microns-thick nanotube or nanoparticle photoanode, we hypothesized that electrons would flow *radially* through a few nanometers of semiconductor to be collected by the adjacent, interdigitated ITO electrode (i-ITO). While the idea of extending the current collector within a DSSC photoanode has been previously postulated,[21] this work represents the first experimental realization. Furthermore, the materials and methods as well as nanoscale architecture reported herein are considerably different from those previously proposed.

6.2. Experimental

6.2.1. Materials

A nominally 60 μm thick AAO membrane with 200 nm pores that is 25-50% porous (Anodisc 13, 0.02 μm, Whatman) was cleaned by 30 s sonication in water followed by an isopropanol rinse. The membranes were coated using atomic layer deposition (ALD) in a custom built viscous flow reactor[22] operating under 1 torr of N_2. For i-ITO samples, the membranes were coated with ~7 nm of ITO by ALD via 45 alternate exposures to cyclopentadienyl indium (InCp) and O_3 at a temperature of 220°C. Reactant exposure times of 15 s and 80 s were employed, respectively, with nitrogen purge periods of 10 s and 5 s after respective exposures. Doping of the In_2O_3 was accomplished by substituting pulses of tetrakisdimethylamido tin (TDMASn) and H_2O_2 every 10^{th} cycle. The exposure times for TDMASn and H_2O_2 were 15 s and 10s, respectively, with 10 s N_2 purge periods following each

exposure. Post-deposition annealing of the membrane under N_2 in a tube furnace at 450°C for 20 minutes increased the conductivity of the i-ITO. A thick (~230 nm) ITO coating was applied to one side of both the i-ITO and uncoated membranes by ion-assisted deposition (IAD) at room temperature.[23] IAD is a line-of-sight deposition method similar to sputtering in which very little ITO penetrates the tapered (20 nm) pores of the asymmetric membrane. Finally, several different thicknesses of amorphous TiO_2 were deposited within each membrane using ALD. During the TiO_2 ALD, the membranes were mounted in a steel fixture designed to minimize TiO_2 growth on the thick IAD ITO layer (to which electrical contact is subsequently made). The TiO_2 ALD was performed using alternating exposures to $TiCl_4$ and H_2O at 100°C for 6 s and 3 s respectively, with nitrogen purges of 10 s and 14 s between exposures. Finally, each sample was soaked in an ethanoic solution of 0.5 mM $(Bu_4N)_2$[Ru(4-(COOH),4'-(COO)-2,2'-bipyridine)$_2$(NCS)$_2$] ("N719", Dyesol, B2 dye) for 20 hours and rinsed with ethanol before devices were assembled according to established methods.[1] Briefly, a 25 μm Surlyn spacer (Solaronix SX1170-25) was sandwiched between the photoanode and a platinized fluorine doped tin oxide (FTO) dark electrode. A 0.28 cm^2 active area was defined by a hole punched through the spacer, which softens at ~80°C to seal the device. Electrical contact was made to each electrode by applying silver epoxy (SPI) to a tin-coated copper wire. A solution of 0.5 M butylmethylimidizolium iodide (TCI America), 0.05 M I_2, and 0.5 M *tert*-butylpyridine in 85:15 acetonitrile:valeronitrile was introduced into the cell via vacuum backfilling through a hole in the platinized FTO electrode. A second Surlyn spacer and microscope cover slip was sealed over the hole with a soldering iron. All chemicals were used as received from Sigma-Aldrich unless otherwise specified.

6.2.2. Instrumentation

Monochromatic illumination for photoresponse experiments was achieved through the excitation slits of a Jobin-Yvon fluorescence spectrometer. *J-V* plots were acquired on a CH Instruments 1202 potentiostat. The AM1.5 power efficiency of a 0.28 cm^2 masked device was measured on a class A solar cell analyzer from Spectra-Nova Technologies. Scanning electron microscopy (SEM) was performed using a Hitachi S4800.

6.3. Results and Discussion

6.3.1. Photoanode Characterization

The viability of the i-ITO photoanode design relies upon the ability of ALD to coat the membrane pores conformally with transparent and conductive ITO. The development of ALD processes for In_2O_3 and SnO_2 using non-halogenated precursors make possible this challenging task.[18-20] That the photoelectrodes employed herein are coated by a continuous film is demonstrated by resistivity measurements through the 60 μm membranes. Though each nanoscale tube that spans a membrane is poorly conductive on its own, in parallel the millions of tubes show a collective resistance < 20 ohm, in analogy to a conductive copper cable composed of many thin filaments. Subsequent annealing in N_2 at 450°C for 15 minutes reduces this value, measured by sandwiching the membrane between metal surfaces, to < 3 ohm.

To prevent the rapid (parasitic) reaction of electrons in the ITO with the hole transporting ions in solution (I_3^-), an equally conformal semiconductor layer is required. To apply this semiconducting layer, ALD of TiO_2 was performed using alternating exposures to $TiCl_4$ and H_2O at 100°C. This growth temperature was selected to minimize etching by $TiCl_4$.[24] Micro-Raman analysis performed after the TiO_2 ALD detected no anatase or rutile peaks on either the i-ITO or

the bare alumina membranes (data not shown), implying that the semiconductor is generated in amorphous form as has been previously reported at this deposition temperature.[25] Cross sectional SEM analysis of a fractured alumina membrane with i-ITO (~15 nm) and TiO_2 pore wall (~20 nm) reveals the bilayer structure of the photoanode, Figure 6.2. The smoothness of the TiO_2 coating is further evidence for an amorphous film.

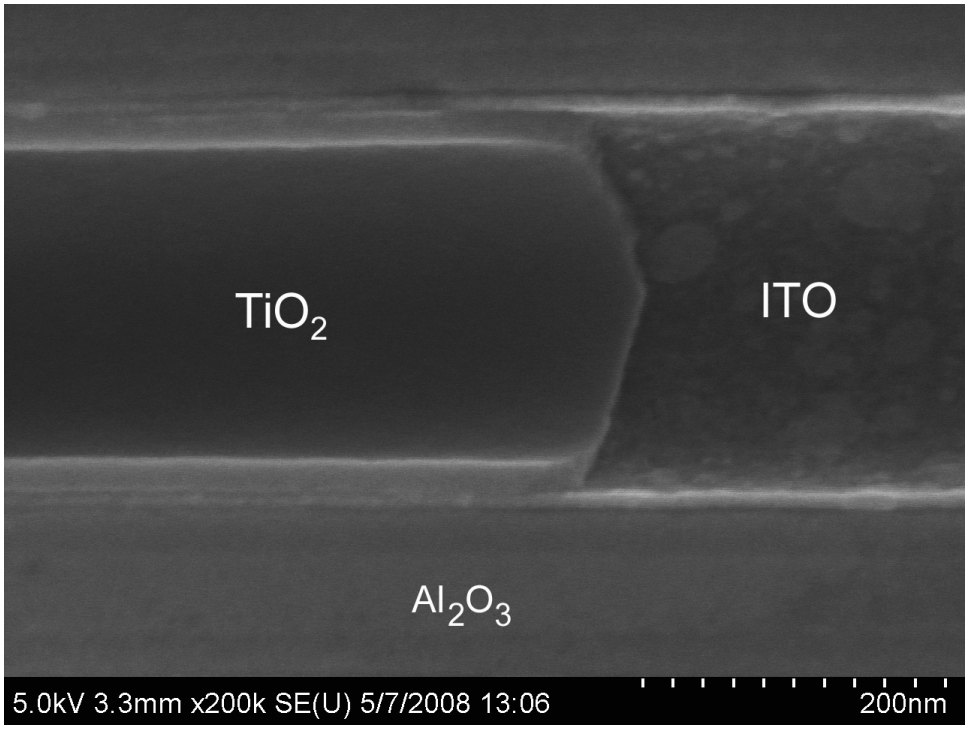

Figure 6.2. Cross-sectional SEM image of a TiO_2 tube cleaved to reveal the i-ITO tube beneath. The concentric tubes, grown by atomic layer deposition, are embedded in a ~60 μm long alumina pore. In order to provide clear imaging, the TiO_2 and i-ITO film thicknesses shown here are thicker than those utilized in photovoltaic devices.

6.3.2. Photovoltaic Performance

Figure 6.3 shows the short-circuit photocurrent densities (J_{sc}) measured for a series of samples prepared with increasing TiO_2 tube wall thickness, with and without i-ITO. The most striking observation is that all of the control samples, lacking i-ITO within the pores, exhibit very small current densities that only slowly increase with TiO_2 thickness. The meager output of the control devices is not surprising since injected electrons, forced to traverse the microns-long amorphous TiO_2 tubes, are expected to be collected extremely inefficiently at the distant TCO (see Figure 6.1a). We hypothesize that the diffusion/hopping of electrons through the amorphous semiconductor is too slow to compete effectively with their interception by I_3^-. The result is a short effective diffusion length over which injected electrons may be collected and consequent poor conversion efficiencies. These small J_{sc} values are in contrast to the J_{sc} of a similarly constructed ZnO nanotube DSSC[12] in which the highly crystalline semiconductor provides an amply efficient electron transport pathway. An additional control, in which only i-ITO is present in the pores, underscores the need for some thickness of semiconductor to rectify the dark current. Here the high surface area TCO exhibits exceedingly large dark currents that overwhelm any photocurrent. In striking contrast, the i-ITO DSSCs (idealized in Figure 6.1b), each with > 2 nm of TiO_2 over 7 nm of ITO within the pores, show larger J_{SC} values (10- to 60-fold) than the controls. Indeed, the current densities approach that of the best ZnO nanotube DSSCs to date.[12]

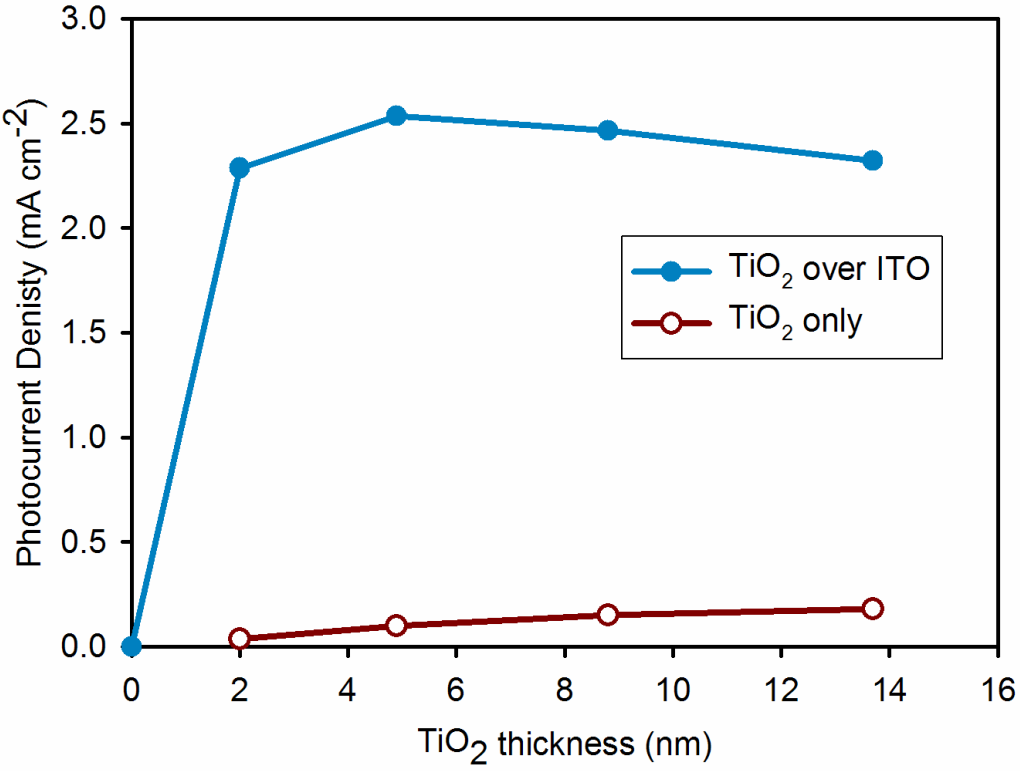

Figure 6.3. Short-circuit photocurrent density for devices with (blue, closed circle) and without (red, open circle) 7 nm of ITO in the pores as a function of TiO_2 tube wall thickness.

Compared to the best nanocrystalline DSSCs, however, nanotube J_{SC} values are still low. Current densities of the nanotube devices are primarily limited by low light harvesting efficiency – a consequence of both the modest surface area of the AAO template (~ 400 cm^2/cm^2) and the propensity of the commercial AAO samples to scatter incident photons and thereby inhibit light penetration. Both problems are, in principle at least, solvable by switching to custom-made, narrow-channel AAO templates. The extent to which photocurrents are ultimately limited by ion transport through the liquid electrolyte is revealed by light intensity dependence measurements, Figure 6.4. The photocurrent increases linearly with light intensity, up to approximately 4 mA/cm^2. Beyond this point, mass transport of I_3^- through the relatively thick photoanode evidently starts becoming detrimental. This effect can be ameliorated to some extent by increasing the concentration of I_3^- in solution (see figure).

The photovoltage at open circuit (V_{OC}) of i-ITO devices is consistently greater than 700 mV, while the *J-V* curve of the control device (without TiO_2, but with i-ITO) passes through the origin. Apparently ≤ 2 nm of TiO_2 is required to reach the maximum photovoltage for the system, Figure 6.5. Amorphous TiO_2 tube DSSCs (without ITO in the pores) also exhibit good photovoltages that peak (or perhaps plateau) around 9 nm. The V_{OC} of the most efficient i-ITO DSSC reported here is within 80% of the V_{OC} of that for the most efficient nanoparticle DSSCs to date (850 mV)[1] implying that the rectifying behavior of amorphous TiO_2 is similar to that of anatase TiO_2 (employed in nanoparticle cells).

The *J-V* curve of the most efficient device, 5 nm TiO_2 over 7 nm ITO, is shown as Figure 6.6. Under AM1.5 illumination the DSSC exhibits a J_{SC} of 2.6 mA/cm^2, V_{OC} of 716 mV, and fill factor (*FF*) of 0.58, yielding an overall conversion efficiency of 1.1%. The modest *FF* is most likely due to a low shunt resistance, the signature of which can be seen in the negatively sloping

photocurrent at low applied potentials. The origin of the shunt resistance is not yet clear.

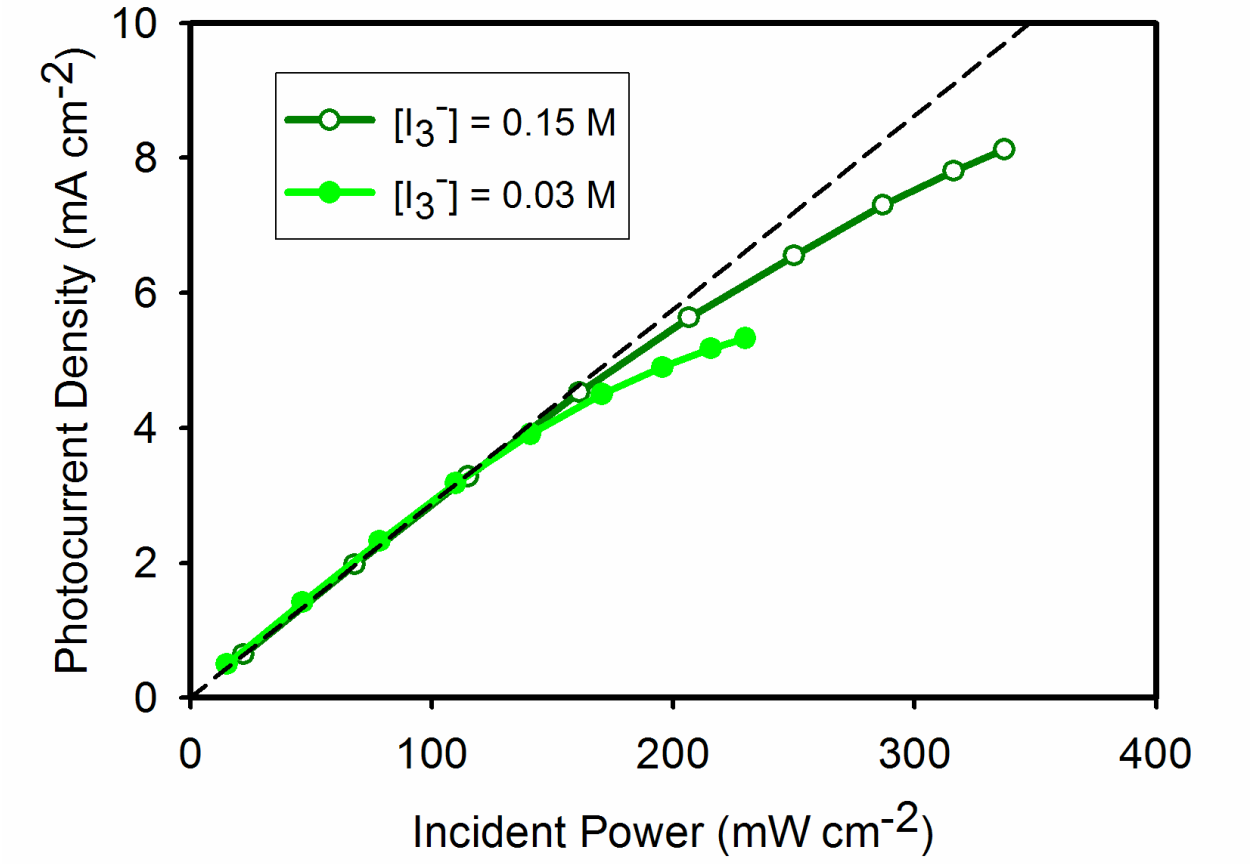

Figure 6.4. Short-circuit photocurrent density (J_{SC}) of the most efficient i-ITO device reported (light green, closed circle) as a function of illumination intensity. The departure from linearity at high light intensity can be reduced by increasing the I_3^- to 0.15 M (dark green, open circle) in an otherwise identical device. The dashed line defines a hypothetical linear J_{SC} /incident-power correlation. Note that 100 mW/cm^2 corresponds approximately to 1 Sun of visible-region light intensity.

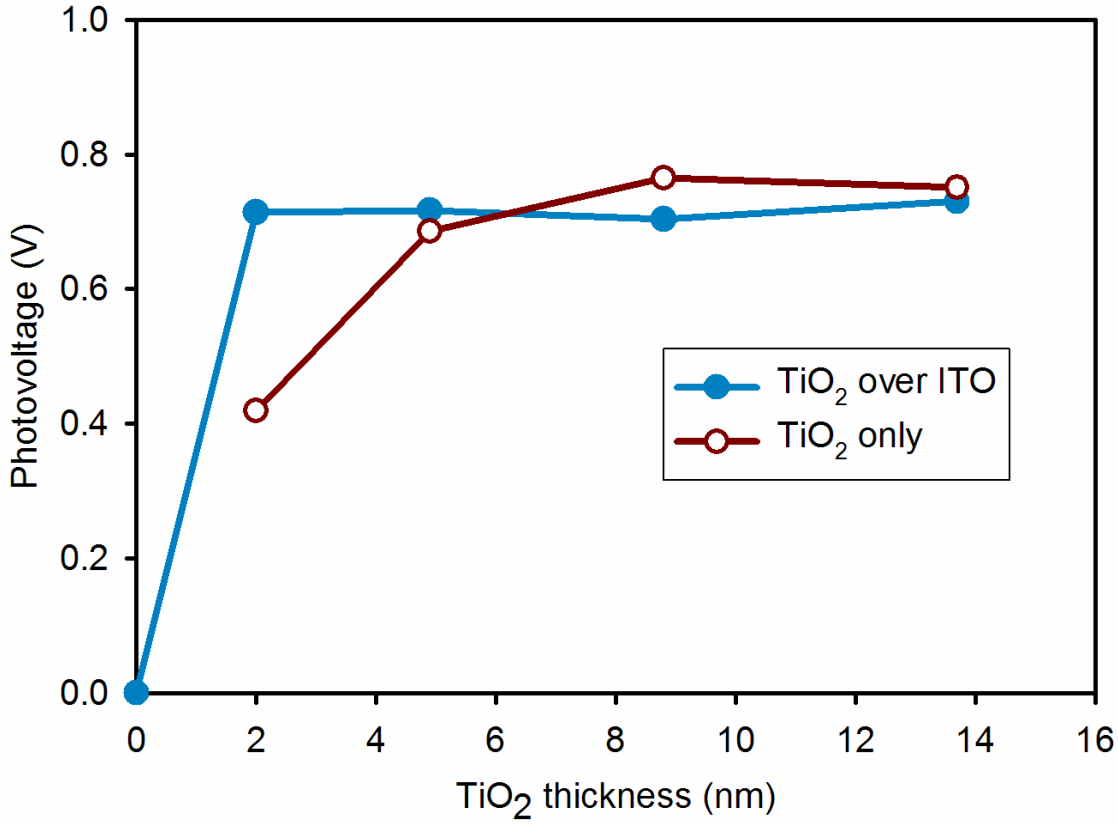

Figure 6.5. Open-circuit photovoltage for devices with (blue, closed circle) and without (red, open circle) ITO in the pores as a function of TiO_2 tube wall thickness.

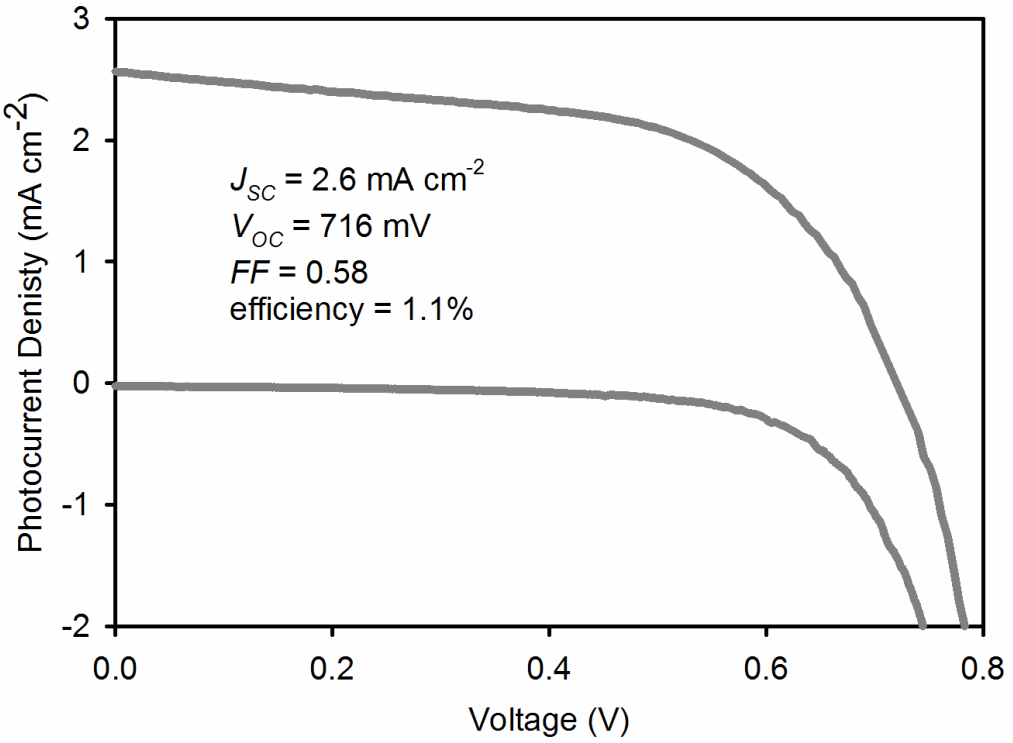

Figure 6.6. *J-V* curve under AM1.5 illumination and in the dark for the most efficient i-ITO device, 5 nm TiO_2 over 7 nm ITO

6.3.3. Photoresponse Spectra

Further insight into the operation of the new photoanodes can be gleaned from the spectral photoresponse of the completed devices. Due to the logarithmic relationship between absorbance and light harvesting efficiency, a longer path length cell will exhibit broadened features on a light harvesting efficiency scale. For example, the difference between a 1 and 2 absorbance unit valley and peak is small (~ 10%) on the light harvesting (1 minus transmission) scale. This effect can be seen in Figure 6.7 around the peak absorbance (~0.7) at 530 nm. It appears that the path length (or in this case "useful" photoanode thickness as reported by photoresponse) is significantly shorter for devices without ITO in the pores. A deviation from this simple analysis is evident between wavelengths 400 - 450 nm where the i-ITO device has a smaller (normalized) photoresponse. This effect is most likely due to the attenuation of blue light traversing the cell by I_3^- and by ITO within the pores. The observation further supports the hypothesis that the useful photoanode thickness is greater for the DSSCs with ITO in the pores.

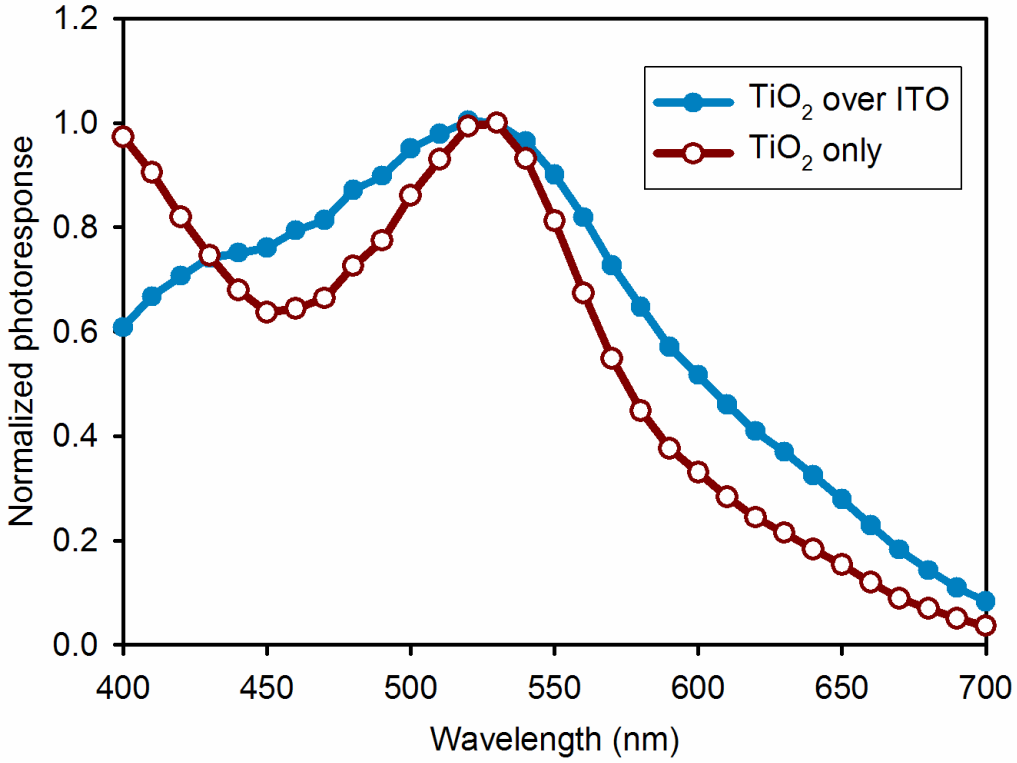

Figure 6.7. Representative normalized photoresponses under short-circuit conditions for devices with (blue, closed circle) and without (red, open circle) ITO in the pores.

6.3.4. Electrochemical Impedance Spectroscopy

As in previous chapters, electrochemical impedance spectroscopy may here also be used to probe the electron extraction and lifetime characteristic of the photoanode. The difficulty here is that the expected result is the negative result. That is, in the limit of short extraction times (due to the very small semiconductor thickness separating the dye and TCO) we expect the resistance to electron transport to become immeasurably small. The signature of success then becomes an efficiently operating device (such that we believe the entire photoanode thickness is being probed) that fits a simpler equivalent circuit, Figure 6.8. Compared to the equivalent circuit fit in Chapter 4, this circuit lacks the resistance to charge transport and consequently collapses into a simple RC circuit, characteristic of flat bilayer heterojuctions. Throughout the range of applied potentials measured the fit is superb, as illustrated by the Bode plot, Figure 6.9.

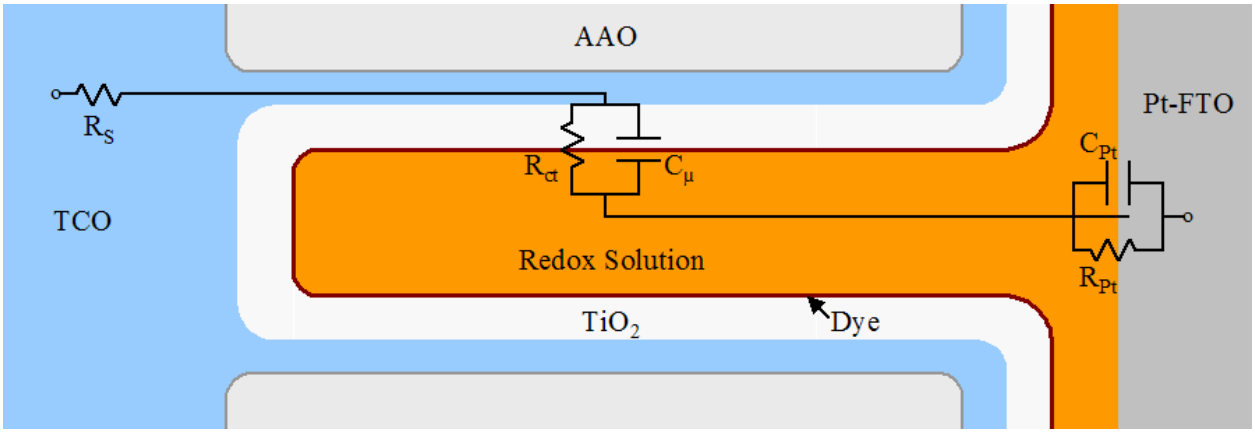

Figure 6.8. The equivalent circuit to which impedance spectrum was fit overlays a highly idealized photoanode schematic. Equivalent circuit elements overlay the geometrically appropriate interface.

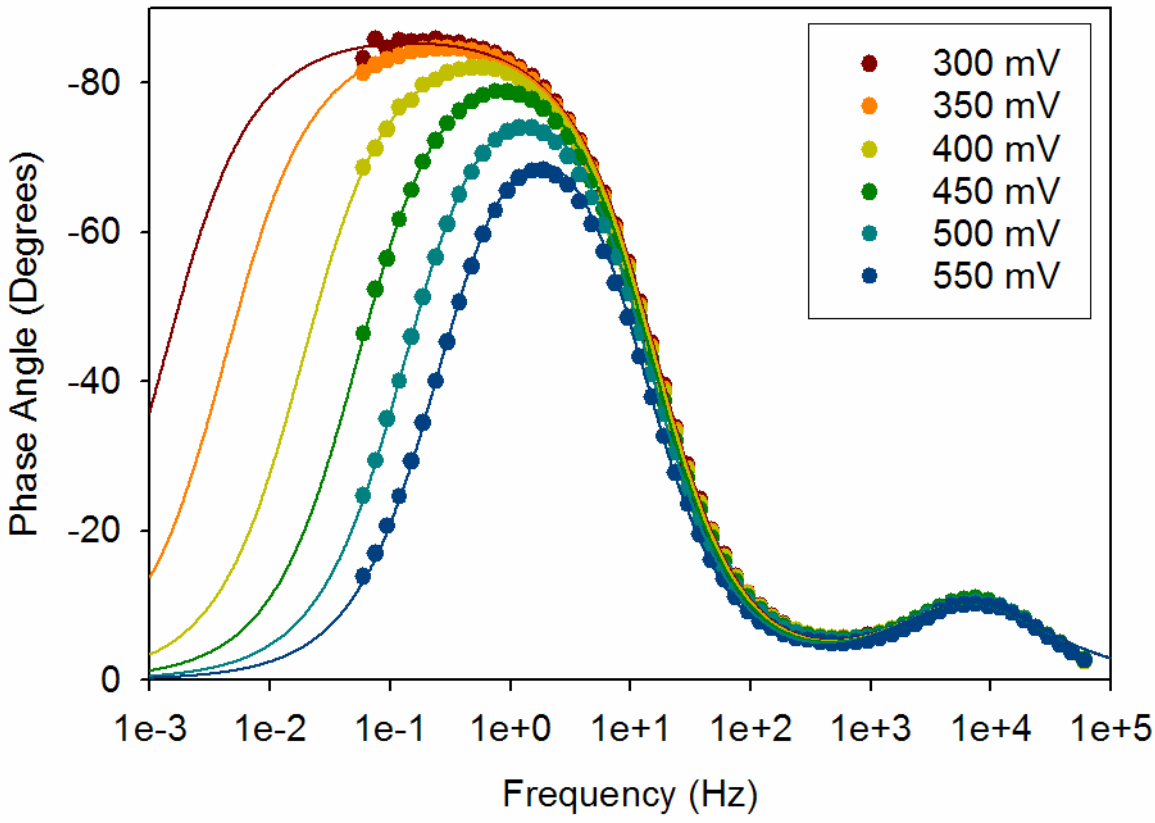

Figure 6.9. Bode plot of i-ITO DSSC impedance (filled circles) as function of applied potential in the dark. Lines trace the fits derived using the simplified equivalent circuit shown in Figure 6.8.

The substantially larger J_{SC} and broadened photoresponse spectra of i-ITO DSSCs indicate that electrons are being collected over a much longer distance than in the control DSSCs. That is, radial electron collection through amorphous TiO_2 (to surrounding ITO) competes effectively with electron interception, even deep within the photoelectrode. In contrast, longitudinal electron diffusion through amorphous TiO_2 (to a distant planar ITO layer) does not. While the control devices based on amorphous TiO_2 tubes were anticipated to perform poorly, the recovery of photovoltaic performance upon interdigitation of a TCO is remarkable and points to a broader utility for the radial collection approach. Particularly intriguing is the prospect of replacing traditional crystalline semiconductors (like anatase TiO_2) with previously unexplored DSSC photoanode materials; amorphous TiO_2 is now the first on this list. Since the task of rapid charge transport has been transferred to the i-ITO, effective use of otherwise inefficient materials such as electrodeposited and/or amorphous indirect bandgap semiconductors (including, perhaps, fuel producing photoelectrodes) may be feasible. Furthermore, the processing temperatures of DSSC photoanodes may be relaxed to allow for greater substrate compatibility.

6.4. Conclusions

In summary, a promising new DSSC photoanode design in which electrons radially diffuse through the wall of semiconducting tubes and are efficiently collected at an adjacent, concentric ITO tube has now been experimentally realized. Atomic layer deposition is used to grow the current collector within an AAO template and subsequently coat the high surface-area electrode with a semiconducting metal oxide. The viability of this architecture as a DSSC photoanode is demonstrated by photovoltaic characterization of completed devices with and without the

interdigitated current collector. This architecture is not limited to AAO templates, and the benefits of radial charge collection may also be realized using other high surface area templates such as aerogels.[26] Like previously reported nanotube array based DSSCs, the power efficiencies of these DSSCs are limited by modest light harvesting efficiency (at least with conventional dyes). Current work is focused on determining the extent to which optimized, higher-area templates can be translated into better photoelectrode performance and the extent to which the idea can be used to advantage with chemical producing (e.g. water oxidizing) photoelectrodes. Finally, these systems are good candidates for the exploration of alternative redox shuttles and previously unexplored semiconducting materials due to their potential for fast electron collection via the adjacent TCO.

Chapter 1 References

1. *Basic Research Needs for Solar Energy Utilization*; 2005.
2. *BP Statistical Review of World Energy* British Petroleum: 2006.
3. *International Energy Outlook*; Energy Information Administration: 2007.
4. Climate Change 2007: Summary for Policymakers. In Fourth Assessment Report of the Intergovernmental Panel on Climate Change: 2007.
5. http://www.iter.org/. In 2008.
6. Statistics Iceland. In http://www.statice.is/, 2008.
7. The History of Solar. In US DOE: Energy Efficiency and Renewable Energy.
8. Gregg, B. A., *J. Phys. Chem. B* **2003,** 107, (20), 4688-4698.
9. O'Regan, B.; Gratzel, M., *Nature* **1991,** 353, (6346), 737-740.
10. Nazeeruddin, M. K.; Kay, A.; Rodicio, I.; Humphry-Baker, R.; Muller, E.; Liska, P.; Vlachopoulos, N.; Gratzel, M., *Journal of the American Chemical Society* **1993,** 115, (14), 6382-6390.
11. Bisquert, J.; Cahen, D.; Hodes, G.; Ruhle, S.; Zaban, A., *Journal of Physical Chemistry B* **2004,** 108, (24), 8106-8118.
12. Meyer, G. J., *Inorganic Chemistry* **2005,** 44, (20), 6852-6864.
13. Peter, L. M., *J. Phys. Chem. C* **2007,** 111, (18), 6601-6612.
14. Gratzel, M., *Inorganic Chemistry* **2005,** 44, (20), 6841-6851.
15. Nazeeruddin, M. K.; Zakeeruddin, S. M.; Humphry-Baker, R.; Jirousek, M.; Liska, P.; Vlachopoulos, N.; Shklover, V.; Fischer, C. H.; Gratzel, M., *Inorganic Chemistry* **1999,** 38, (26), 6298-6305.

16. Benko, G.; Kallioinen, J.; Korppi-Tommola, J. E. I.; Yartsev, A. P.; Sundstrom, V., *Journal of the American Chemical Society* **2002,** 124, (3), 489-493.

17. Wenger, B.; Gratzel, M.; Moser, J. E., *Journal of the American Chemical Society* **2005,** 127, (35), 12150-12151.

18. Haque, S. A.; Palomares, E.; Cho, B. M.; Green, A. N. M.; Hirata, N.; Klug, D. R.; Durrant, J. R., *Journal of the American Chemical Society* **2005,** 127, (10), 3456-3462.

19. Kroeze, J. E.; Hirata, N.; Koops, S.; Nazeeruddin, M. K.; Schmidt-Mende, L.; Gratzel, M.; Durrant, J. R., *Journal of the American Chemical Society* **2006,** 128, (50), 16376-16383.

20. Clifford, J. N.; Palomares, E.; Nazeeruddin, M. K.; Gratzel, M.; Durrant, J. R., *Journal of Physical Chemistry C* **2007,** 111, (17), 6561-6567.

21. Palomares, E.; Clifford, J. N.; Haque, S. A.; Lutz, T.; Durrant, J. R., *Journal of the American Chemical Society* **2003,** 125, (2), 475-482.

22. O'Regan, B. C.; Bakker, K.; Kroeze, J.; Smit, H.; Sommeling, P.; Durrant, J. R., *Journal of Physical Chemistry B* **2006,** 110, (34), 17155-17160.

23. Nazeeruddin, M. K.; De Angelis, F.; Fantacci, S.; Selloni, A.; Viscardi, G.; Liska, P.; Ito, S.; Takeru, B.; Gratzel, M. G., *Journal of the American Chemical Society* **2005,** 127, (48), 16835-16847.

24. Durrant, J. R.; Haque, S. A.; Palomares, E., *Coordination Chemistry Reviews* **2004,** 248, (13-14), 1247-1257.

25. Sodergren, S.; Hagfeldt, A.; Olsson, J.; Lindquist, S. E., *Journal of Physical Chemistry* **1994,** 98, (21), 5552-5556.

26. Lee, J. J.; Coia, G. M.; Lewis, N. S., *Journal of Physical Chemistry B* **2004,** 108, (17), 5269-5281.

27. Bisquert, J.; Zaban, A.; Salvador, P., *Journal of Physical Chemistry B* **2002,** 106, (34), 8774-8782.

28. Peter, L. M.; Duffy, N. W.; Wang, R. L.; Wijayantha, K. G. U., *J. Electroanal. Chem.* **2002,** 524, 127-136.

29. Bisquert, J.; Zaban, A.; Greenshtein, M.; Mora-Sero, I., *Journal of the American Chemical Society* **2004,** 126, (41), 13550-13559.

30. Cameron, P. J.; Peter, L. M., *Journal of Physical Chemistry B* **2005,** 109, (15), 7392-7398.

31. Kopidakis, N.; Benkstein, K. D.; van de Lagemaat, J.; Frank, A. J., *Journal of Physical Chemistry B* **2003,** 107, (41), 11307-11315.

32. Forro, L.; Chauvet, O.; Emin, D.; Zuppiroli, L.; Berger, H.; Levy, F., *Journal of Applied Physics* **1994,** 75, (1), 633-635.

33. Sauve, G.; Cass, M. E.; Doig, S. J.; Lauermann, I.; Pomykal, K.; Lewis, N. S., *Journal of Physical Chemistry B* **2000,** 104, (15), 3488-3491.

34. Gregg, B. A.; Pichot, F.; Ferrere, S.; Fields, C. L., *J. Phys. Chem. B* **2001,** 105, (7), 1422-1429.

35. Schlichthorl, G.; Park, N. G.; Frank, A. J., *Journal of Physical Chemistry B* **1999,** 103, (5), 782-791.

36. Gregg, B. A., *Coord. Chem. Rev.* **2004,** 248, (13-14), 1215-1224.

37. Cazzanti, S.; Caramori, S.; Argazzi, R.; Elliott, C. M.; Bignozzi, C. A., *J. Am. Chem. Soc.* **2006,** 128, (31), 9996-9997.

38. Sapp, S. A.; Elliott, C. M.; Contado, C.; Caramori, S.; Bignozzi, C. A., *Journal of the American Chemical Society* **2002,** 124, (37), 11215-11222.

39. Hamann, T. W.; Brunschwig, B. S.; Lewis, N. S., *Journal of Physical Chemistry B* **2006,** 110, (50), 25514-25520.

40. Gratzel, M., *MRS Bulletin* **2005,** 30, (1), 23-27.

41. Wang, P.; Zakeeruddin, S. M.; Moser, J. E.; Nazeeruddin, M. K.; Sekiguchi, T.; Gratzel, M., *Nature Materials* **2003,** 2, (6), 402-407.

42. Kopidakis, N.; Neale, N. R.; Frank, A. J., *Journal of Physical Chemistry B* **2006,** 110, (25), 12485-12489.

43. Hamann, T. W.; Martinson, A. B. F.; Elam, J. W.; Pellin, M. J.; Hupp, J. T., *Prepr Pap ACS Div. Fuel Chem.* **2007,** 52, (2).

44. Zhu, K.; Kopidakis, N.; Neale, N. R.; van de Lagemaat, J.; Frank, A. J., *Journal of Physical Chemistry B* **2006,** 110, (50), 25174-25180.

45. Law, M.; Greene, L. E.; Radenovic, A.; Kuykendall, T.; Liphardt, J.; Yang, P. D., *Journal of Physical Chemistry B* **2006,** 110, (45), 22652-22663.

46. Handa, S.; Haque, S. A.; Durrant, J. R., *Advanced Functional Materials* **2007,** 17, (15), 2878-2883.

47. Splan, K. E.; Hupp, J. T., *Langmuir* **2004,** 20, (24), 10560-10566.

48. Angiolillo, P. J.; Susumu, K.; Uyeda, H. T.; Lin, V. S. Y.; Shediac, R.; Therien, M. J., *Synthetic Metals* **2001,** 116, (1-3), 247-253.

49. Nazeeruddin, M. K.; Pechy, P.; Renouard, T.; Zakeeruddin, S. M.; Humphry-Baker, R.; Comte, P.; Liska, P.; Cevey, L.; Costa, E.; Shklover, V.; Spiccia, L.; Deacon, G. B.;

Bignozzi, C. A.; Gratzel, M., *Journal of the American Chemical Society* **2001,** 123, (8), 1613-1624.

50. Gaal, D. A.; Hupp, J. T., *Journal of the American Chemical Society* **2000,** 122, (44), 10956-10963.

51. Kuciauskas, D.; Freund, M. S.; Gray, H. B.; Winkler, J. R.; Lewis, N. S., *Journal of Physical Chemistry B* **2001,** 105, (2), 392-403.

52. Gaal, D. A.; McGarrah, J. E.; Liu, F.; Cook, J. E.; Hupp, J. T., *Photochemical & Photobiological Sciences* **2004,** 3, (3), 240-245.

53. Nelson, J.; Haque, S. A.; Klug, D. R.; Durrant, J. R., *Physical Review B* **2001,** 6320, (20).

54. Hasselmann, G. M.; Meyer, G. J., *Journal of Physical Chemistry B* **1999,** 103, (36), 7671-7675.

Chapter 2 References

1. Peter, L. M.; Wijayantha, K. G. U., *Electrochim. Acta* **2000,** 45, 4543-4551.
2. Schlichthorl, G.; Park, N. G.; Frank, A. J., *Journal of Physical Chemistry B* **1999,** 103, (5), 782-791.
3. Cao, F.; Oskam, G.; Meyer, G. J.; Searson, P. C., *Journal of Physical Chemistry* **1996,** 100, (42), 17021-17027.
4. Dloczik, L.; Ileperuma, O.; Lauermann, I.; Peter, L. M.; Ponomarev, E. A.; Redmond, G.; Shaw, N. J.; Uhlendorf, I., *Journal of Physical Chemistry B* **1997,** 101, (49), 10281-10289.
5. Hosono, E.; Fujihara, S.; Honna, I.; Zhou, H. S., *Advanced Materials* **2005,** 17, (17), 2091.
6. Kakiuchi, K.; Hosono, E.; Fuiihara, S., *Journal of Photochemistry and Photobiology a-Chemistry* **2006,** 179, (1-2), 81-86.
7. Bedja, I.; Kamat, P. V.; Hua, X.; Lappin, A. G.; Hotchandani, S., *Langmuir* **1997,** 13, (8), 2398-2403.
8. Law, M.; Greene, L. E.; Johnson, J. C.; Saykally, R.; Yang, P. D., *Nature Materials* **2005,** 4, (6), 455-459.
9. Kim, K. S.; Kang, Y. S.; Lee, J. H.; Shin, Y. J.; Park, N. G.; Ryu, K. S.; Chang, S. H., *B. Kor. Chem. Soc.* **2006,** 27, (2), 295-298.
10. Gao, Y. F.; Nagai, M., *Langmuir* **2006,** 22, (8), 3936-3940.
11. Ravirajan, P.; Peiro, A. M.; Nazeeruddin, M. K.; Graetzel, M.; Bradley, D. D. C.; Durrant, J. R.; Nelson, J., *Journal of Physical Chemistry B* **2006,** 110, (15), 7635-7639.

12. Kruger, J.; Plass, R.; Gratzel, M.; Cameron, P. J.; Peter, L. M., *Journal of Physical Chemistry B* **2003,** 107, (31), 7536-7539.

13. Park, N. G.; Kang, M. G.; Kim, K. M.; Ryu, K. S.; Chang, S. H.; Kim, D. K.; van de Lagemaat, J.; Benkstein, K. D.; Frank, A. J., *Langmuir* **2004,** 20, (10), 4246-4253.

14. Govender, K.; Boyle, D. S.; Kenway, P. B.; O'Brien, P., *Journal of Materials Chemistry* **2004,** 14, (16), 2575-2591.

15. Greene, L. E.; Law, M.; Tan, D. H.; Montano, M.; Goldberger, J.; Somorjai, G.; Yang, P. D., *Nano Lett.* **2005,** 5, (7), 1231-1236.

16. Peter, L. M., *Physical Chemistry Chemical Physics* **2007,** 9, (21), 2630-2642.

17. Frank, A. J.; Kopidakis, N.; van de Lagemaat, J., *Coord. Chem. Rev.* **2004,** 248, 1165-1179.

Chapter 3 References

1. Gratzel, M., *Inorg. Chem.* **2005,** 44, (20), 6841-6851.
2. Benko, G.; Yartsev, A. P.; Sundstrom, V., *Trends in Optics and Photonics* **2002,** 72, (Thirteenth International Conference on Ultrafast Phenomena, 2002), 434-435.
3. Kallioinen, J.; Benkoe, G.; Myllyperkioe, P.; Khriachtchev, L.; Skrman, B.; Wallenberg, R.; Tuomikoski, M.; Korppi-Tommola, J.; Sundstroem, V.; Yartsev, A. P., *J. Phys. Chem. B* **2004,** 108, (20), 6365-6373.
4. Frank, A. J.; Kopidakis, N.; van de Lagemaat, J., *Coordin. Chem. Rev.* **2004,** 248, (13-14), 1165-1179.
5. Law, M.; Greene, L. E.; Radenovic, A.; Kuykendall, T.; Liphardt, J.; Yang, P., *J. Phys. Chem. B* **2006,** 110, (45), 22652-22663.
6. Fabregat-Santiago, F.; Garcia-Canadas, J.; Palomares, E.; Clifford, J. N.; Haque, S. A.; Durrant, J. R.; Garcia-Belmonte, G.; Bisquert, J., *J. Appl. Phys.* **2004,** 96, (11), 6903-6907.
7. Kroeze, J. E.; Hirata, N.; Koops, S.; Nazeeruddin, M. K.; Schmidt-Mende, L.; Gratzel, M.; Durrant, J. R., *J. Am. Chem. Soc.* **2006,** 128, (50), 16376-16383.
8. Kruger, J.; Plass, R.; Gratzel, M.; Cameron, P. J.; Peter, L. M., *J. Phys. Chem. B* **2003,** 107, (31), 7536-7539.
9. Gratzel, M., *MRS Bull.* **2005,** 30, (1), 23-27.
10. Law, M.; Greene, L. E.; Johnson, J. C.; Saykally, R.; Yang, P. D., *Nat. Mater.* **2005,** 4, (6), 455-459.

11. Yoshida, T.; Pauporté, T.; Lincot, D.; Oekermann, T.; Minoura, H., *J. Electrochem. Soc.* **2003,** 150, (C608).

12. Paulose, M.; Shankar, K.; Varghese, O. K.; Mor, G. K.; Grimes, C. A., *J. Phys. D Appl. Phys.* **2006,** 39, (12), 2498-2503.

13. Galoppini, E.; Rochford, J.; Chen, H.; Saraf, G.; Lu, Y.; Hagfeldt, A.; Boschloo, G., *J. Phys. Chem. B* **2006,** 110, (33), 16159-16161.

14. Martinson, A. B. F.; McGarrah, J. E.; Parpia, M. O. K.; Hupp, J. T., *Phys. Chem. Chem. Phys.* **2006,** 8, 4655 - 4659.

15. Greene, L. E.; Yuhas, B. D.; Law, M.; Zitoun, D.; Yang, P., *Inorg. Chem.* **2006,** 45, (19), 7535-7543.

16. Elam, J. W.; Routkevitch, D.; Mardilovich, P. P.; George, S. M., *Chem. Mater.* **2003,** 15, (18), 3507-3517.

17. Li, A. P.; Müller, F.; Birner, A.; Nielsch, K.; Gösele, U., *J. Appl. Phys.* **1998,** 84, 6023-6026.

18. Masuda, H.; Yada, K.; Osaka, A., *Jpn. J. Appl. Phys.* **1998,** 37, L1340-L1342.

19. Lee, W.; Ji, R.; Gösele, U.; Nielsch, K., *Nat. Mater.* **2006,** 5, 741-747.

20. Kakiuchi, K.; Hosono, E.; Fujihara, S., *J. Photoch. Photobio. A* **2006,** 179, 81-86.

21. Zaban, A.; Greenshtein, M.; Bisquert, J., *ChemPhysChem* **2003,** 4, 859-864.

22. Quintana, M.; Edvinsson, T.; Hagfeldt, A.; Boschloo, G., *J. Phys. Chem. C* **2007,** 111, 1035-1041.

23. Wang, Z.-S.; Kawauchi, H.; Kashima, T.; Arakawa, H., *Coordin. Chem. Rev.* **2004,** 248, (13-14), 1381-1389.

24. Elam, J. W.; Martinson, A. B. F.; Pellin, M. J.; Hupp, J. T., *Chem. Mater.* **2006,** 18, (15), 3571-3578.

Chapter 4 References

1. O' Regan, B.; Gratzel, M., *Nature* **1991,** 353, (6346), 737-740.
2. Nazeeruddin, M. K.; Kay, A.; Rodicio, I.; Humphrybaker, R.; Muller, E.; Liska, P.; Vlachopoulos, N.; Gratzel, M., *Journal of the American Chemical Society* **1993,** 115, (14), 6382-6390.
3. Wang, Q.; Ito, S.; Gratzel, M.; Fabregat-Santiago, F.; Mora-Sero, I.; Bisquert, J.; Bessho, T.; Imai, H., *Journal of Physical Chemistry B* **2006,** 110, (50), 25210-25221.
4. Kayes, B. M.; Atwater, H. A.; Lewis, N. S., *Journal of Applied Physics* **2005,** 97, (11).
5. Li, G.; Shrotriya, V.; Huang, J. S.; Yao, Y.; Moriarty, T.; Emery, K.; Yang, Y., *Nature Materials* **2005,** 4, (11), 864-868.
6. Sodergren, S.; Hagfeldt, A.; Olsson, J.; Lindquist, S. E., *Journal of Physical Chemistry* **1994,** 98, (21), 5552-5556.
7. Martinson, A. B. F.; Hamann, T. W.; Pellin, M. J.; Hupp, J. T., *Chemistry - A European Journal* **2008,** 14, (15), 4458-4467.
8. Lee, J. J.; Coia, G. M.; Lewis, N. S., *Journal of Physical Chemistry B* **2004,** 108, (17), 5282-5293.
9. Law, M.; Greene, L. E.; Johnson, J. C.; Saykally, R.; Yang, P. D., *Nature Materials* **2005,** 4, (6), 455-459.
10. Martinson, A. B. F.; Elam, J. W.; Hupp, J. T.; Pellin, M. J., *Nano Letters* **2007,** 7, (8), 2183-2187.
11. Ku, C. H.; Wua, J. J., *Applied Physics Letters* **2007,** 91, (9).

12. Sapp, S. A.; Elliott, C. M.; Contado, C.; Caramori, S.; Bignozzi, C. A., *Journal of the American Chemical Society* **2002,** 124, (37), 11215-11222.

13. Fabregat-Santiago, F.; Garcia-Belmonte, G.; Bisquert, J.; Zaban, A.; Salvador, P., *J. Phys. Chem. B* **2002,** 106, (2), 334-339.

14. Kern, R.; Sastrawan, R.; Ferber, J.; Stangl, R.; Luther, J., *Electrochimica Acta* **2002,** 47, (26), 4213-4225.

15. Bisquert, J.; Vikhrenko, V. S., *J. Phys. Chem. B* **2004,** 108, (7), 2313-2322.

16. Fabregat-Santiago, F.; Bisquert, J.; Garcia-Belmonte, G.; Boschloo, G.; Hagfeldt, A., *Solar Energy Materials and Solar Cells* **2005,** 87, (1-4), 117-131.

17. Lim, S. J.; Kwon, S. J.; Kim, H., *Thin Solid Films* **2008,** 516, (7), 1523-1528.

18. Huby, N.; Ferrari, S.; Guziewicz, E.; Godlewski, M.; Osinniy, V., *Applied Physics Letters* **2008,** 92, (2).

19. Zaban, A.; Greenshtein, M.; Bisquert, J., *Chemphyschem* **2003,** 4, (8), 859-864.

Chapter 5 References

1. Edwards, P. P.; Porch, A.; Jones, M. O.; Morgan, D. V.; Perks, R. M., *Dalton Transactions* **2004**, (19), 2995-3002.
2. Kiriakidis, G.; Suchea, M.; Christoulakis, S.; Katsarakis, N., *Reviews on Advanced Materials Science* **2005,** 10, (3), 215-223.
3. Golovanov, V.; Maeki-Jaskari, M. A.; Rantala, T. T.; Korotcenkov, G.; Brinzari, V.; Cornet, A.; Morante, J., *Sensors and Actuators, B: Chemical* **2005,** B106, (2), 563-571.
4. Korotcenkov, G.; Brinzari, V.; Cerneavschi, A.; Ivanov, M.; Golovanov, V.; Cornet, A.; Morante, J.; Cabot, A.; Arbiol, J., *Thin Solid Films* **2004,** 460, (1-2), 315-323.
5. Gervasini, A.; Perdigon-Melon, J. A.; Guimon, C.; Auroux, A., *Journal of Physical Chemistry B* **2006,** 110, (1), 240-249.
6. Perdigon-Melon, J. A.; Gervasini, A.; Auroux, A., *Journal of Catalysis* **2005,** 234, (2), 421-430.
7. Li, J.; Hao, J.; Cui, X.; Fu, L., *Catalysis Letters* **2005,** 103, (1-2), 75-82.
8. Zhu, T.; Hao, J.; Fu, L.; Wang, J.; Li, J.; Liu, Z.; Cui, X., *Huanjing Kexue* **2004,** 25, (3), 26-29.
9. Ren, L.; Zhang, T.; Xu, C.; Lin, L., *Topics in Catalysis* **2004,** 30/31, (1-4), 55-57.
10. Qiao, Z.; Mergel, D., *Thin Solid Films* **2005,** 484, (1-2), 146-153.
11. Nishimura, E.; Ohkawa, H.; Sato, Y.; Song, P.-K.; Shigesato, Y., *Shinku* **2004,** 47, (11), 796-801.
12. Kim, H. W.; Kim, N. H.; Myung, J. H., *Journal of Materials Science* **2005,** 40, (18), 4991-4993.

13. Ni, J.; Yan, H.; Wang, A.; Yang, Y.; Stern, C. L.; Metz, A. W.; Jin, S.; Wang, L.; Marks, T. J.; Ireland, J. R.; Kannewurf, C. R., *Journal of the American Chemical Society* **2005,** 127, (15), 5613-5624.

14. Kim, N. H.; Myung, J. H.; Kim, H. W.; Lee, C., *Physica Status Solidi A: Applied Research* **2005,** 202, (1), 108-112.

15. Girtan, M.; Folcher, G., *Surface and Coatings Technology* **2003,** 172, (2-3), 242-250.

16. Asikainen, T.; Ritala, M.; Leskela, M., *Journal Of The Electrochemical Society* **1994,** 141, (11), 3210-3213.

17. Asikainen, T.; Ritala, M.; Leskelae, M., *Journal of the Electrochemical Society* **1995,** 142, (10), 3538-41.

18. Asikainen, T.; Ritala, M.; Leskelae, M., *Vacuum* **1995,** 46, (8-10), 887.

19. Ritala, M.; Asikainen, T.; Leskela, H., *Electrochemical And Solid State Letters* **1998,** 1, (3), 156-157.

20. Ritala, M.; Asikainen, T.; Leskelae, M.; Skarp, J., *Materials Research Society Symposium Proceedings* **1996,** 426, (Thin Films for Photovoltaic and Related Device Applications), 513-518.

21. Ritala, M.; Leskela, M., *Handbook of Thin Film Materials* **2002,** 1, 103-159.

22. Pellin, M. J.; Stair, P. C.; Xiong, G.; Elam, J. W.; Birrell, J.; Curtiss, L.; George, S. M.; Han, C. Y.; Iton, L.; Kung, H.; Kung, M.; Wang, H. H., *Catalysis Letters* **2005,** 102, (3-4), 127-130.

23. Kucheyev, S. O.; Biener, J.; Wang, Y. M.; Baumann, T. F.; Wu, K. J.; van Buuren, T.; Hamza, A. V.; Satcher, J. H.; Elam, J. W.; Pellin, M. J., *Applied Physics Letters* **2005,** 86, (8).

24. Elam, J. W.; Routkevitch, D.; Mardilovich, P. P.; George, S. M., *Chemistry of Materials* **2003,** 15, (18), 3507-3517.

25. Ott, A. W.; Johnson, J. M.; Klaus, J. W.; George, S. M., *Applied Surface Science* **1997,** 112, 205-215.

26. Haugan, H. J.; Yu, W.; Lee, S. T.; Petrou, A.; McCombe, B. D.; Brewer, K. S.; Lees, J. F.; Beachley, O. T., *Journal Of Crystal Growth* **2002,** 244, (2), 157-167.

27. Elam, J. W.; Groner, M. D.; George, S. M., *Reviews of Scientific Instruments* **2002,** 73, (8), 2981-2987.

28. Elam, J. W.; Pellin, M. J., *Analytical Chemistry* **2005,** 77, (11), 3531-3535.

29. Paivasaari, J.; Putkonen, M.; Sajavaara, T.; Niinisto, L., *Journal Of Alloys And Compounds* **2004,** 374, (1-2), 124-128.

30. Myllymaki, P.; Nieminen, M.; Niinisto, J.; Putkonen, M.; Kukli, K.; Niinisto, L., *Journal Of Materials Chemistry* **2006,** 16, (6), 563-569.

31. Niinisto, J.; Petrova, N.; Putkonen, M.; Niinisto, L.; Arstila, K.; Sajavaara, T., *Journal Of Crystal Growth* **2005,** 285, (1-2), 191-200.

32. Paivasaari, J.; Niinisto, J.; Arstila, K.; Kukli, K.; Putkonen, M.; Niinisto, L., *Chemical Vapor Deposition* **2005,** 11, (10), 415-419.

33. Niinisto, J.; Putkonen, M.; Niinisto, L.; Stoll, S. L.; Kukli, K.; Sajavaara, T.; Ritala, M.; Leskela, M., *Journal Of Materials Chemistry* **2005,** 15, (23), 2271-2275.

34. *Eight Peak Index of Mass Spectra*. Mass Spectometry Data Centre, The Royal Society of Chemistry: Cambridge, UK, 1991; Vol. 1.

35. Ferguson, J. D.; Weimer, A. W.; George, S. M., *Applied Surface Science* **2000,** 162, 280-292.

36. Niskanen, A.; Arstila, K.; Ritala, M.; Leskela, M., *Journal Of The Electrochemical Society* **2005,** 152, (7), F90-F93.

37. Elam, J. W.; Sechrist, Z. A.; George, S. M., *Thin Solid Films* **2002,** 414, 43-55.

38. Ritala, M.; Leskela, M.; Nykanen, E.; Soininen, P.; Niinisto, L., *Thin Solid Films* **1993,** 225, (1-2), 288-295.

39. Calnan, S.; Upadhyaya, H. M.; Thwaites, M. J.; Tiwari, A. N., *Thin Solid Films* **2007,** 515, (15), 6045-6050.

40. Rozati, S. M.; Ganj, T., *Renewable Energy* **2004,** 29, (10), 1671-1676.

41. Tahar, R. B. H.; Ban, T.; Ohya, Y.; Takahashi, Y., *Journal of Applied Physics* **1998,** 83, (4), 2139-2141.

42. Suzuki, A.; Maki, K., *Chemical Vapor Deposition* **2006,** 12, (10), 608-613.

43. Gupta, R. K.; Mamidi, N.; Ghosh, K.; Mishra, S. R.; Kahol, P. K., *Journal Of Optoelectronics And Advanced Materials* **2007,** 9, (7), 2211-2216.

44. Asikainen, T.; Ritala, M.; Leskela, M., *Journal of the Electrochemical Society* **1995,** 142, (10), 3538-3541.

45. Puurunen, R. L., *Chemical Vapor Deposition* **2005,** 11, (2), 79-90.

46. Martinson, A.; Elam, J.; Hupp, J.; Pellin, M. J., *Nano Letters* **2007**, (7), 2183-2187.

47. Elam, J. W.; Martinson, A. B. F.; Pellin, M. J.; Hupp, J. T., *Chemistry of Materials* **2006,** 18, (15), 3571-3578.

48. Elam, J. W.; Baker, D. A.; Hryn, A. J.; Martinson, A. B. F.; Pellin, M. J.; Hupp, J. T., *Journal of Vacuum Science and Technology A* **2007,** Submitted.

Chapter 6 References

1. Nazeeruddin, M. K.; De Angelis, F.; Fantacci, S.; Selloni, A.; Viscardi, G.; Liska, P.; Ito, S.; Takeru, B.; Gratzel, M. G. *J. Am. Chem. Soc.* **2005,** 127, (48), 16835-16847.
2. Dloczik, L.; Ileperuma, O.; Lauermann, I.; Peter, L. M.; Ponomarev, E. A.; Redmond, G.; Shaw, N. J.; Uhlendorf, I. *J. Phys. Chem. B* **1997,** 101, (49), 10281-10289.
3. van de Lagemaat, J.; Zhu, K.; Benkstein, K. D.; Frank, A. J. *Inorg. Chim. Acta* **2008,** 361, (3), 620-626.
4. Wang, Q.; Ito, S.; Gratzel, M.; Fabregat-Santiago, F.; Mora-Sero, I.; Bisquert, J.; Bessho, T.; Imai, H. *J. Phys. Chem. B* **2006,** 110, (50), 25210-25221.
5. Nusbaumer, H.; Moser, J. E.; Zakeeruddin, S. M.; Nazeeruddin, M. K.; Gratzel, M. *J. Phys. Chem. B* **2001,** 105, (43), 10461-10464.
6. Wang, Z. S.; Sayama, K.; Sugihara, H. *J. Phys. Chem. B* **2005,** 109, (47), 22449-22455.
7. Wang, P.; Zakeeruddin, S. M.; Moser, J. E.; Humphry-Baker, R.; Gratzel, M. *J. Am. Chem. Soc.* **2004,** 126, (23), 7164-7165.
8. Gorlov, M.; Pettersson, H.; Hagfeldt, A.; Kloo, L. *Inorg. Chem.* **2007,** 46, (9), 3566-3575.
9. Clifford, J. N.; Palomares, E.; Nazeeruddin, M. K.; Gratzel, M.; Durrant, J. R. *J. Phys. Chem. C* **2007,** 111, (17), 6561-6567.
10. Nazeeruddin, M. K.; Kay, A.; Rodicio, I.; Humphrybaker, R.; Muller, E.; Liska, P.; Vlachopoulos, N.; Gratzel, M. *J. Am. Chem. Soc.* **1993,** 115, (14), 6382-6390.
11. Law, M.; Greene, L. E.; Johnson, J. C.; Saykally, R.; Yang, P. D. *Nat. Mater.* **2005,** 4, (6), 455-459.

12. Martinson, A. B. F.; Elam, J. W.; Hupp, J. T.; Pellin, M. J. *Nano Lett.* **2007,** 7, (8), 2183-2187.

13. Mor, G. K.; Shankar, K.; Paulose, M.; Varghese, O. K.; Grimes, C. A. *Nano Lett.* **2006,** 6, (2), 215-218.

14. Sodergren, S.; Hagfeldt, A.; Olsson, J.; Lindquist, S. E. *J. Phys. Chem.* **1994,** 98, (21), 5552-5556.

15. Peter, L. M. *J. Phys. Chem. C* **2007,** 111, (18), 6601-6612.

16. Lee, J. J.; Coia, G. M.; Lewis, N. S. *J. Phys. Chem. B* **2004,** 108, (17), 5282-5293.

17. Martinson, A. B. F.; Hamann, T. W.; Pellin, M. J.; Hupp, J. T. *Chem.-Eur. J.* **2008,** 14, (15), 4458-4467.

18. Elam, J. W.; Baker, D. A.; Martinson, A. B. F.; Pellin, M. J.; Hupp, J. T. *J. Phys. Chem. C* **2008,** 112, (6), 1938-1945.

19. Elam, J. W.; Martinson, A. B. F.; Pellin, M. J.; Hupp, J. T. *Chem. Mater.* **2006,** 18, (15), 3571-3578.

20. Elam, J. W.; Baker, D. A.; Hryn, A. J.; Martinson, A. B. F.; Pellin, M. J.; Hupp, J. T. *J. Vac. Sci. Technol., A* **2008,** 26, (2), 244-252.

21. Grinis, L.; Ofir, A.; Zaban, A. *J. Phys. Chem. B* **2005,** 109, (5), 1643-1647.

22. Elam, J. W.; Groner, M. D.; George, S. M. *Rev. Sci. Instrum.* **2002,** 73, (8), 2981-2987.

23. Yang, Y.; Huang, Q. L.; Metz, A. W.; Ni, J.; Jin, S.; Marks, T. J.; Madsen, M. E.; DiVenere, A.; Ho, S. T. *Adv. Mater.* **2004,** 16, (4), 321-+.

24. Puurunen, R. L. *Chem. Vap. Deposition* **2005,** 11, (2), 79-90.

25. Aarik, J.; Aidla, A.; Uustare, T.; Sammelselg, V. *J. Cryst. Growth* **1995,** 148, (3), 268-275.

26. Hamann, T. W.; Martinson, A. B. F.; Elam, J. W.; Pellin, M. J.; Hupp, J. T. *Adv. Mater.* **2008,** 20, (8), 1560-1564.

Alex B. F. Martinson

Northwestern University, Department of Chemistry
2145 Sheridan Road, Evanston, IL 60208
Office: (847) 467-4935, Fax: (847) 497-1425
Email: a-martinson2@northwestern.edu

Education

PhD, Northwestern University, Evanston, Illinois — 2008
Charge Dynamics in New Architectures for Dye-Sensitized Solar Cells

BA (Summa Cum Laude), Luther College, Decorah, Iowa — 2003
Majors: Chemistry, Mathematics; Minor: Physics (GPA: 3.99/4.0)

Experience

Laboratory Graduate Fellow, Argonne National Laboratory — Argonne, IL
Fellowship Advisor: Dr. Michael Pellin — 2005-Present

Research Assistant, Northwestern University — Evanston, IL
Advisor: Prof. Joseph T. Hupp — 2003-Present

Research Intern, Argonne National Laboratory — Argonne, IL
Advisor: Dr. Theodore Krause — 2003

Research Intern, National Renewable Energy Laboratory — Golden, CO
Advisor: Dr. David Ginley — 2002

Research Intern, Northwestern University — Evanston, IL
Advisor: Prof. Kenneth Poeppelmeier — 2001

Honors

Argonne Lab-Grad Fellow — 2006-present
Colin Garfield Fink Summer Fellowship of The Electrochemical Society — 2006
University Scholar (Northwestern University) — 2005-2006
Link Foundation Energy Fellowship — 2005-2006
Docken Scholarship/Outstanding Chemistry Student (Luther College) — 2002-2003
Maytag Innovation Award for Student Research — 2002
Barry M. Goldwater Scholarship — 2002-2003

Professional Affiliations

American Chemical Society, member since 2004
Phi Lambda Upsilon National Chemistry Honor Society, member since 2005
Electrochemical Society, member since 2006

Recent Presentations

"Anodic Aluminum Oxide Templated Nanotube Electrodes via Atomic Layer Depositions" – oral presentation, 211th Meeting of the Electrochemical Society, Chicago, IL, 2007

"New Photoanode Architectures for Dye-Sensitized Solar Cells" – poster presentation, Gordon Research Conference (Renewable Energy: Solar Fuels), Ventura Beach, CA, 2007

Publications

Hamann, T. W.; Martinson, A. B. F.; Elam, J. W.; Pellin, M. J.; Hupp, J. T. "Atomic Layer Deposition of TiO2 on Aerogel Templates: New Photoanodes for Dye-Sensitized Solar Cells" *J. Phys. Chem. C* , **2008**, accepted.

Hamann, T. W.; Martinson, A. B. F.' Elam, J. W.; Pellin, M. J.; Hupp, J. T. "Aerogel Templated ZnO Dye-Sensitized Solar Cells," *Adv. Mater.*, **2008** , 20, 1560-1564.

Martinson, A. B. F.; Hamann, T. W.; Pellin, M. J.; Hupp, J. T. "New Architectures for Dye-Sensitized Solar Cells" *Chem-Eur J.*, **2007**, 15, 4458-4467.

Elam, J. W.; Baker, D. A.; Martinson, A. B. F.; Pellin, M. J.; Hupp, J. T. "Atomic Layer Deposition of Indium-Tin Oxide Thin Films Using Non-Halogenated Precursors" *J. Phys. Chem. C*, **2007**, 112, 1938-1945.

Elam, J. W.; Baker, D. A.; Hryn, A. J.; Martinson, A. B. F.; Pellin, M. J.; Hupp, J. T. "Atomic Layer Deposition of Tin Oxide Films Using Tetrakis(dimethylamino) Tin" *J. Vac. Sci. Technol. A*, **2007**, 26, 244-252.

Martinson, A. B. F.; Elam, J. W.; Hupp, J. T.; Pellin, M. J. "ZnO Nanotube Dye-Sensitized Solar Cells" *Nano Letters*, **2007**, *7*, 2183-2187.

Martinson, A. B. F.; McGarrah, J. E.; Parpia, M. O. K.; Hupp, J. T. "Dynamics of Charge Transport and Recombination in ZnO Nanorod Array Dye Sensitized Solar Cells" *Phys. Chem. Chem. Phys.*, **2006,** *8*, 4655 - 4659.

Elam, J. W.; Martinson, A. B. F.; Pellin, M. J.; Hupp, J. T. "Atomic Layer Deposition of In_2O_3 Using Cyclopentadienyl Indium: A New Synthetic Route to Transparent Conducting Oxide Films" *Chem. Mater.*, **2006**, *18*, 3571-3578.

Martinson, A. B. F.; Massari, A. M.; Lee, S. J.; Gurney, R. W.; Splan, K. E.; Hupp, J. T.; Nguyen, S. T. "Organic Photovoltaics Interdigitated on the Molecular Scale" *J. Electrochem. Soc.*, **2006**, *153*, A527-A532.

Ginley, D.; Roy, B.; Ode, A.; Warmsingh, C.; Yoshida, Y.; Parilla, P.; Teplin, C.; Kaydanova, T.; Miedaner, A.; Curtis, C.; Martinson, A., Coutts, T.; Readey, D.; Hosono, H.; Perkins, J. "Non-vacuum and PLD Growth of Next Generation TCO Materials" *Thin Solid Films*, **2003**, *445*, 193-198.

Floros, N, F.; Rijssenbeek, J. T.; Martinson, A. B.; Poeppelmeier, K. R. "Structural study of A_2CuTiO_6 (A = Y, Tb-Lu) compounds" *Solid State Sci.* **2002**, *4*, 1495-1498.

Patents

Pellin, M.; Elam, J.; Welp, U.; Martinson, A.; Hupp, J. "Heterojunction Photovoltaic Assembled with Atomic Layer Deposition" **2007**, patent pending.

Pellin, M.; Elam, J.; Martinson, A.; Hupp, J. "Synthesis of Transparent Conducting Oxide Coatings" **2007**, patent pending.